Simulating a topological gauge theory in a Raman-dressed Bose-Einstein condensate

by

Anika Frölian

Thesis Advisor:
Prof. Dr. Leticia Tarruell

ICFO – Institut de Ciències Fotòniques
UPC – Universitat Politècnica de Catalunya

April 2022

Thesis committee:

Prof. Dr. Jérôme Beugnon (Université Pierre et Marie Curie, France)
Prof. Dr. Patrik Öhberg (Heriot-Watt University, United Kingdom)
Prof. Dr. Hugues de Riedmatten (ICFO – Institut de Ciències Fotòniques, Spain)

Abstract

Ultracold quantum gases constitute a powerful and versatile tool to experimentally explore quantum many-body physics. This thesis presents an original contribution to the quantum simulation of gauge theories with ultracold atoms, which has evolved into a thriving research field during the last years.

Gauge theories form the basis of our modern understanding of nature, with applications ranging from high energy to condensed matter physics. A subclass formed by topological gauge theories plays a key role in the effective description of certain strongly correlated materials. An important example is the fractional quantum Hall effect, where the topological Chern-Simons theory can provide an effective single-particle description for some of the filling factors. A simpler toy model which already provides access to the key properties of topological gauge theories is the one-dimensional chiral BF theory obtained from Chern-Simons theory after dimensional reduction. This thesis reports on the quantum simulation of the chiral BF theory in an ultracold gas of bosonic potassium atoms, establishing ultracold quantum gases as a resource for the quantum simulation of topological gauge theories.

As a first step, we establish the theoretical framework necessary for the quantum simulation of the chiral BF theory. We start by deriving an encoded Hamiltonian for this gauge theory in which the gauge degrees of freedom are eliminated via the local symmetry constraint. The encoding results in a system with only matter particles that have local but unconventional chiral interactions. We continue by showing that these chiral interactions can be realized in a Raman-dressed Bose-Einstein condensate (BEC) with unbalanced interactions by deriving an effective single-component Hamiltonian from a microscopic view in momentum space.

Subsequently, we present the implementation of the different ingredients necessary to realize the chiral BF theory in our experiment. In a first series of experiments, we study the effects of coherent coupling on the effective collisional properties of the system. To this end, we employ radio-frequency to couple two internal states with unequal interaction in a ^{39}K BEC. We measure the effective scattering length of the system as a function of the coupling field parameters. Moreover, we use the coherent coupling as an interaction control tool and quench the effective interactions from repulsive to attractive values. Afterwards, we turn to the implementation of Raman coupling and characterize the modifications in the dispersion of Raman-dressed atoms at the single particle level.

Finally, we demonstrate the realization of the chiral BF theory by combining Raman coupling and unbalanced interactions in a BEC of ^{39}K. We probe the chiral interactions arising in the system and observe the formation of chiral bright solitons which dissolve as soon as their propagation direction is inverted. Moreover, we use the local symmetry constraint of the theory to reveal the BF electric field through measurements on the matter field alone, and show that it leads to an asymmetric expansion of the condensate. Our experiments establish chiral interactions as a novel resource for quantum simulation experiments and pave the way towards implementing topological gauge theories in higher dimensions with ultracold atoms.

Resumen

Los gases cuánticos ultrafríos constituyen una herramienta poderosa y versátil para explorar experimentalmente la física cuántica de muchos cuerpos. Esta tesis presenta una contribución original a la simulación cuántica de las teorías gauge con átomos ultrafríos, que se ha convertido en un floreciente campo de investigación durante los últimos años.

Las teorías gauge constituyen la base de nuestra comprensión moderna de la naturaleza, con aplicaciones que van desde la física de alta energía hasta la de materia condensada. Una subclase formada por las teorías gauge topológicas desempeña un papel clave en la descripción efectiva de ciertos materiales fuertemente correlacionados. Un ejemplo importante es el efecto Hall cuántico fraccionario, en el que la teoría topológica de Chern-Simons puede proporcionar una descripción efectiva de una sola partícula para algunos de los factores de relleno. Un modelo más sencillo que ya proporciona acceso a las propiedades clave de las teorías gauge topológicas es la teoría BF quiral unidimensional obtenida a partir de la teoría de Chern-Simons tras la reducción dimensional.

Esta tesis reporta sobre la simulación cuántica de la teoría BF quiral en un gas ultrafrío de átomos bosónicos de potasio, estableciendo los gases cuánticos ultrafríos como un recurso para la simulación cuántica de teorías gauge topológicas. Como primer paso, establecemos el marco teórico necesario para la simulación cuántica de la teoría BF quiral. Comenzamos derivando un Hamiltoniano codificado para esta teoría gauge en la que los grados de libertad gauge se eliminan a través de la restricción de simetría local. La codificación da como resultado un sistema con sólo partículas de materia que tienen interacciones quirales locales pero no convencionales. Continuamos mostrando que estas interacciones quirales pueden realizarse en un condensado de Bose-Einstein (BEC) con acoplamiento Raman y con interacciones desequilibradas, derivando un Hamiltoniano efectivo de una solo componente desde una visión microscópica en el espacio de momentos. Posteriormente, presentamos la implementación de los diferentes ingredientes necesarios para realizar la teoría BF quiral en nuestro experimento.

En una primera serie de experimentos, estudiamos los efectos del acoplamiento coherente sobre las propiedades colisionales efectivas del sistema. Para ello, empleamos radiofrecuencia para acoplar dos estados internos con interacción desigual en un condensado de potasio-39. Medimos la longitud de dispersión efectiva del

sistema en función de los parámetros del campo de acoplamiento. Además, utilizamos el acoplamiento coherente como herramienta de control de la interacción y cambiamos súbitamente las interacciones efectivas desde valores repulsivos hasta atractivos.

Posteriormente, pasamos a la implementación del acoplamiento Raman y caracterizamos las modificaciones en la dispersión de los átomos con acoplamiento Raman a nivel de una sola partícula. Finalmente, demostramos la realización de la teoría BF quiral combinando el acoplamiento Raman y las interacciones desequilibradas en un BEC de potasio-39. Investigamos las interacciones quirales que surgen en el sistema y observamos la formación de solitones brillantes quirales que se disuelven en cuanto se invierte su dirección de propagación. Además, utilizamos la restricción de simetría local de la teoría para revelar el campo eléctrico BF a través de mediciones en el campo de la materia solamente, y mostramos que conlleva a una expansión asimétrica del condensado. Nuestros experimentos establecen las interacciones quirales como un recurso novedoso para los experimentos de simulación cuántica y establecen las bases para la implementación de teorías gauge topológicas en dimensiones superiores con átomos ultrafríos.

Prologue and acknowledgements

When I was young, a PhD in Physics seemed incredible far away. Although I already had a huge interest in Physics and was reading popular science books like "A Brief History of Time" from Stephen Hawking in my 7th grade of high school, my grades in Physics and Maths were disastrous and nobody - including myself - believed I would study Physics one day. In fact, my teachers gave me the impression that Maths and Physics were to difficult for me. Luckily, one teacher conveyed to me that Maths (at least to some extent) can be understood by everyone and together with my curiosity and ambition things turned around. Today, I am deeply thankful for this teacher and everyone who encouraged me.

This thesis summarizes the work accomplished during my PhD studies and the scientific results obtained along the way. The following part is dedicated to those people who were part of my journey throughout the last four years.

First, I would like to thank Leticia for giving me the opportunity to spend the past years in the QGE group at ICFO and for guiding me through all challenges. Your advice, expertise and knowledge has been a constant source of support and a crucial driving force for the success of our research projects. Your immense dedication and involvement impressed me from the very first day onwards.

The results presented in this thesis are the outcome of an intensive teamwork. During the years, I worked in different constellations extensively together with former and current members of the QGE-K team, involving in historical order Julio, Cesar, Bruno, Manon, Craig, Elettra and Ramón. It was a pleasure to work with you and the results described here are the outcome of our common efforts. We shared some moments of despair, when e.g. trying to trace back atom number fluctuations or wrapping taller around the PID boxes to shield them from radio-frequency, but also precious moments when we realized a measurement finally worked or we understood something new. Moreover, I would like to thank:
Julio for introducing me to every part of the machine and having a master plan for installing the objectives. But also for familiarizing me with Catalunya and explaining me Catalan politics, the importance of *calcots* and *el tío de navidad* during the lunch break.
Cesar for teaching me to listen to the machine and showing me how to solve problems creatively. Your motivation and enthusiasm was contagious. The Mexican/German combination worked so well in the Lab, however made it quite chal-

lenging to meet outside...lets go for drinks in Barcelona soon!
Bruno for giving me important advices already in my first weeks.
Craig for being the crucial constant during most of the time and almost all projects. We shared so many hours, days, weeks and months in the Lab. I learned much from you - the unquestioned python and electronics expert of our group. In addition, you showed me how to survive with sarcasm and pointed out to me the subtleties of the English language.
Elettra for making work so pleasant, with you even "going back to the magnetic trap" was fun! I am indebted for your shared insights into the theory part of our work and also the ones from psychology and life in general. Thanks for the many moments of laughter we shared and your kindness.
Ramón for always keeping the overview and staying calm and friendly in any situation. In moments when most of us were desperate you maintained a general optimism and lifted my spirits. Thank you for being a great listener and taking so much interest in any story from the working day or weekend.

In addition to the direct members of the QGE-K team, I am grateful to Alessio Celi from UAB for our fruitful collaboration. The completion of our chiral BF project would have been impossible without your input and your help in translating the theory jargon to us experimentalists! I also wish to thank Tobias and Valentin for all discussions and informal talks about gauge theories. Thanks also to the rest of the QGE group, in particular to Jonatan, Vasiliy, Sandra and Toni, who shared all their shiny nice new tools with my team and were always ready to give some advice.

The help I received continued while I wrote down this thesis. I am indebted to my committee members Patrik Öhberg, Jérôme Beugnon and Hugues de Riedmatten for their helpful feedback which improved this thesis. Moreover, to Leticia and Elettra for their intensive proofreading and for discussing any open questions I had. Furthermore, Ramón and Leticia assisted me with the translation of the abstract into *castellano*.

Apart from this scientific help, I am thankful for all the support received from ICFO, the institute enabled me to fully concentrate on the research. In particular, I would like to mention the facility unit with Carlos and his team, who are doing an amazing job and were always ready to repair our chillers or even came on the weekends to switch back on our AC after powercuts. Moreover, I benefited from the excellent mechanical workshop lead by Xavi and the electronic workshop of Jose Carlos and his team. The purchasing unit with Santi and Magda made orders as simple and fast as possible and the IT department impressed me with its reliable quick responses. The HR unit was of utterly importance to me as it made life so much easier by taking care of most bureaucracy, e.g. Anne helped in any matter

and even brought me to a doctor when I arrived with huge back pain on my first day in ICFO. Moreover, Rut did a fantastic job in organizing the administration process towards my thesis defence.

Throughout all the these years, I enjoyed to be part of the QGE group and being an ICFOnian. Thanks to the potassium and strontium team with Leticia, Julio, Cesar, Bruno, Manon, David, Craig, Teo, Jonatan, Daniel, Elettra, Ramón, Vasiliy, Sandra, Ana, Toni and Max, I had a relaxed office atmosphere and nice lunch breaks in which not only the progress in the labs, but also all cultural differences we represent were discussed in great detail. I am also thankful to Valentin and Daniel who proved themselves as professional and reliable partner in organizing the weekly Journal club of the ICFO groups working with cold atoms. In general, I experienced the atmosphere in ICFO as welcoming and inclusive and it made a big difference to me to be surrounded by friendly faces every day!

I received funding for my PhD studies in form of the INPhINIT fellowship from "la Caixa" Foundation (ID 100010434). The fellowship code is LCF/BQ/DI18/11660040 and is co-funded by the European Union's Horizon 2020 research and innovation programme under the Marie Skłodowska-Curie grant agreement No. 713673. My fellowship also offered an amazing supporting programme ranging from workshops to outreach activities.

Finally, I am thankful for everyone who made my life outside ICFO and the research environment so enjoyable. It was great to dive into the Spanish language with Jelena and Craig. My randomly found flatmates Shuchi, Niels and initially Pei-Sheng turned out to be a huge lottery win and made me feel at home in the middle of busy Barcelona. I am deeply grateful for our usually common dinners allowing me to disconnect from the working day. I was stunned over and over again by your friendship and support. And thanks to you I know a good restaurant for nearly every country cuisine (somehow Zeeshan keeps to be the most memorable experience). My personal highlights were certainly the many amazing explorations into the rural countryside and climbing the mountains of the Pyrenees in Catalunya and Aragon. Mostly together with Shuchi, Niels, Zafer and Nick we made it from *el Montardo* to *Puigmal*, from *la puerta del cielo* to *Miami beach* and back.

Living in another country and in particular in Covid times, my family and friends back in Germany could feel quite distant. Thanks to all keeping in touch and my family for supporting me unconditionally.

Contents

1 Introduction

Ultracold quantum gases are a versatile testbed for simulating complex many-body physics in a quantum simulator approach. One important research direction of the field is the simulation of gauge theories, a theoretical concept crucial for the description of nature. A broad class, important in high energy physics, describes the coupling between matter and dynamical gauge fields. However gauge theories emerging in certain condensed matter systems, as in fractional quantum Hall states, belong to a different class where the gauge fields are of topological nature.
This chapter introduces gauge theories, motivates the simulation of gauge theories with ultracold quantum gases and describes the experimental advances of the field in the realization of dynamical and topological gauge theories, which is precisely the topic of this work. We conclude the chapter by outlining the aim and structure of this thesis.

In the last years we have witnessed an immense quest towards a programmable quantum computer[1,2]. Not only research institutions, but also major telecommunication companies entered the race to build the first scalable and fault-tolerant computer with quantum supremacy. One application of a quantum computer will be the modelling of complex quantum many-body systems where the interatomic interactions lead to collective phenomena on the quantum level. The precise evolution of such condensed matter systems cannot be calculated nowadays as the computational power of any classical supercomputer in the world is not sufficient. Therefore these strongly correlated quantum systems including high T_c superconductors, fractional quantum Hall states and frustrated spin systems often remain poorly understood.

Despite all promising progress, a universal quantum computer within the next decade is still out of reach. However, there exists a different solution for this problem, namely instead of calculating one can simulate the system of interest with a special purpose analogue quantum computer, a device commonly referred to as quantum simulator. To this end a well-controlled quantum system can be employed which is effectively described by the Hamiltonian of the condensed matter system we want to study. The idea of using quantum hardware to mimic the behaviour of complex quantum systems was envisioned by Feynman[3] and his quantum simulator approach can be realized on many different platforms, ranging from trapped ions[4], superconducting qubits[5] to ultracold quantum gases[6,7], on which we will focus in this thesis.

In a dilute atomic gas, the distance between particles is much larger than the range of the interatomic interaction potential and the interactions can be well encapsulated in a single parameter, the scattering length, making a simple microscopic theoretical description possible. Moreover, degenerate gases offer an outstanding experimental control: the external trapping potential can easily be modified, the interaction between atoms tuned or the dimensionality effectively reduced. Therefore ultracold quantum gases constitute an ideal candidate to study the evolution of complex condensed matter systems and also to realize parameter regimes which are otherwise inaccessible in nature. They have already been successfully employed to tackle open problems of condensed matter physics[6,7]. For example, the interaction control over different orders of magnitude allowed the investigation of different regimes of superfluidity in fermionic gases where the interactions were tuned from the strongly to the weakly interacting limit and the crossover between a molecular Bose-Einstein condensate and BCS state was observed[8]. The outstanding control of the external trapping potential enabled the realization of the prominent Hubbard model by confining bosonic or fermionic atoms in optical lattices, so quantum phase transitions like the bosonic superfluid to Mott transition could be explored[9]. In combination with recent established single site resolution, this also allowed the

simulation of quantum magnetism with fermions[10]. Moreover, ultracold atoms in effectively one and two dimensions were realized, unlocking the possibility to reach e.g. the Tonks-Girardeau gas[11] or to study quasi-long-range order, e.g. the BKT transition[12]. Last but not least, ultracold gases are also extremely well isolated from the environment, which makes the investigation of out of equilibrium physics, e.g. the quantum dynamics after a quench of a system parameter possible[13,14].

Over the last years, a big quest of the research community is the quantum simulation of gauge theories[15–19], which form the basis of our modern understanding of nature as they e.g describe the interactions of fundamental particles. However, they can be investigated theoretically only within certain limitations, making a quantum simulation beneficial.

This thesis contributes to the research field of degenerate gases as platform to simulate effective gauge theories emerging in strongly-correlated systems. In the remaining part of this chapter, we will introduce gauge theories in general and summarize recent advances in their simulation before describing more concretely the thesis goal and the outline of this thesis.

1.1 Gauge theories

Gauge theories are field theories emerging from local symmetry constraints or equivalently local conservation laws in the system. They describe a matter and a gauge field, minimally coupled to matter, and dictate the interaction between gauge particles and matter particles to ensure the system fulfils invariance with respect to its defining symmetry in every point in space and time. In the next paragraph, we will illustrate this concept and the connection between symmetries, conservation laws and gauge theories. To this end, we follow the seminal publication of R. Mills in Ref. [20] and as an example recall his derivation of the prototypical gauge theory of electromagnetism which naturally unfolds when enforcing locally charge conservation.

Every symmetry of a physical system corresponds to a conservation law and vice versa, this is known as Noether theorem. Let us consider one operator $\hat{A}$ with observable A and the Hamiltonian operator $\hat{H}$. With Ψ the state vector of the system, the expectation value of $\hat{A}$ is $\langle \Psi | \hat{A} | \Psi \rangle$ and the expectation value of $\hat{H}$ is the energy of the system. The unitary transformation generated by $\hat{A}$ is given by $\Psi \rightarrow \Psi' = \exp\left(-i\lambda\hat{A}\right)\Psi$ with λ a real parameter of arbitrary value. The Hamiltonian operator generates time displacements *via* $\Psi(t) = \exp\left(-i\hat{H}t\right)\Psi(0)$. If the two operators commute, so $[\hat{A}, \hat{H}] = 0$, the expectation value of $\hat{A}$ is invariant under the transformation generated by $\hat{H}$ and vice versa. This statement actually

implies that $\langle \Psi | \hat{A} | \Psi \rangle$ is a constant over time, i.e. it is a conserved quantity. Moreover, because $\hat{H}$ is invariant under the transformations generated by $\hat{A}$, this operator represents a symmetry of the system. Hence, an operator describing a system's symmetry has a conserved expectation value and a conserved quantity implies a particular symmetry of the system. An example for this relation is a system with translational symmetry where the corresponding conserved quantity is the momentum.

We now turn to the link between conservation laws or equivalently symmetries and gauge theories. As an example we investigate in the following the conservation law of the electric charge Q. Its operator $\hat{Q}$ generates transformations of the form

$$\Psi(x) \to \Psi'(x) = \exp(-ine\theta)\Psi(x) \approx (1 - ine\theta)\Psi(x) \tag{1.1}$$

where Ψ describes a particle with charge ne and θ is an arbitrary parameter. The invariance of a system under this global symmetry is trivial as any physical observable involves terms of Ψ^* and Ψ, such that a global phase factor cancels. However, the situation changes drastically if the symmetry has to be fulfilled locally. In this case, θ is a function of position x, so the transformation generated by $\hat{Q}$ differs at each point and leads to a local phase factor which is not trivial. Hence, terms with a derivative of Ψ will not be invariant under this transformation as they transform as

$$\partial_x \Psi'(x) - \partial_x \Psi(x) = -ine\theta(x)\partial_x \Psi(x) - ine(\partial_x \theta(x))\Psi(x), \tag{1.2}$$

with a new second term with respect to the previous case of $\theta \neq \theta(x)$ for the global transformation. In order to restore invariance under the local transformation, we have to introduce a new invariant derivative D_μ which has to take the form

$$D_\mu = \partial_\mu + ineA_\mu \tag{1.3}$$

where A_μ has to fulfil

$$A_\mu \to A'_\mu = A_\mu + \partial_\mu \theta(x) \tag{1.4}$$

under the transformation. In the following, $\mu = 0, \dots d$ where $\mu = 0$ represents the time component and $1, \dots d$ the spatial components. In the way we defined the covariant derivative in eq. (1.3) and (1.4), A_μ leads to invariance under the symmetry transformation and we refer to it as gauge potential. The so defined covariant derivative and gauge potential A_μ actually are the vector potential of electromagnetism, minimally coupled to matter.
In order to obtain the full field theory, we need to construct the corresponding Lorentz- and gauge invariant Lagrangian density. If the Lagrangian density $\mathcal{L}_{\text{matter}}$ for the matter field alone is known, we just have to replace the standard derivatives therein with the covariant derivative and add an invariant term to the Lagrangian

density which makes the gauge potential dynamically active.
Assuming a non-relativistic bosonic matter field, the Lagrangian density for the matter field alone is in dimension of $3+1$ spacetime

$$\mathcal{L}_{\text{matter}} = i\psi^* \dot{\psi} + \frac{1}{2m}\psi^* \nabla^2 \psi - V(\rho), \tag{1.5}$$

where we have set the reduced Planck constant $\hbar$, the speed of light c and the electron charge e to 1. m is the mass of the matter particle and the dot denotes the time derivative, e.g. $\dot{\psi} \equiv \partial_0 \psi$, and $V(\rho)$ are the matter-matter interactions, which depend only on the matter density ρ. If we replace the standard derivatives with the covariant ones, we have $i\psi^* \dot{\psi} - A^0 \rho$ and $(\psi^*(\nabla - i\mathbf{A})^2 \psi)/(2m)$. In the Lagrangian density this is equivalent to $\frac{1}{2m}\psi^* \nabla^2 \psi - A_\mu J^\mu$ where the time component of the current is simply the density, $J^0 = \rho = |\psi|^2$ and the three spatial components are given by $\mathbf{J} = [(\psi^*(\nabla - i\mathbf{A})\psi - \psi(\nabla + i\mathbf{A})\psi^*)]/(2mi)$. Here, spatial vectors are denoted in bold and with the index up, so $(\mathbf{A})^i = A^i = -A_i$.

In order to obtain non trivial field equations for the gauge field, we need to supplement the Lagrangian density with a term involving derivatives of A_μ. In electromagnetism, the gauge field is dynamically active by itself, so we need derivates to second order. Note that there also exist gauge theories which are not dynamical but topological and where derivatives to first order are sufficient, see below. The only combination of the derivatives which maintains the gauge invariance is

$$F_{\mu\nu} = \partial_\nu A_\mu - \partial_\mu A_\nu \tag{1.6}$$

as a gauge transformation generated by $\hat{Q}$ results in two cross derivatives of θ which cancel. This gauge invariant combination is the well known electromagnetic field tensor. We further account for the desired Lorentz invariance by forming the scalar product of $F_{\mu\nu}$. Then the total Lagrangian density reads

$$\mathcal{L}_{\text{M}} = -\frac{1}{4}F_{\mu\nu}F^{\mu\nu} - A_\mu J^\mu + \mathcal{L}_{\text{matter}}. \tag{1.7}$$

where a scaling factor $\frac{1}{4}$ was introduced. Eq.(1.7) is the well-known Lagrangian density for electromagnetism. Applying the Euler Lagrange equations yield the equations of motion for the matter and the gauge field. One obtains the familiar Maxwell equations for the gauge field and in particular Gauss law

$$\boldsymbol{\nabla} \cdot \mathbf{E} = \rho, \tag{1.8}$$

where $(\mathbf{E})^i = -F^{0i}$ is the electric field generated by the gauge potential. The Gauss law describes the coupling between matter and gauge field and as long at it is fulfilled, gauge invariance is preserved.

In summary, just imposing the symmetry of charge conservation locally yields a

fully-determined field theory which describes the familiar gauge potential of electromagnetism minimally coupled to the matter field and determines the interaction between gauge and matter particles *via* the Gauss law.
In the following, we will also refer to the here presented field theory of electromagnetism as Maxwell theory and for the quantum version use the term quantum electrodynamics (QED).

Gauge theories are classified by their underlying symmetries. In our example of electromagnetism, the system is invariant under all symmetry transformations giving a complex (and local) phase factor (see eq.(1.2)), which form a symmetry group on a circle, the unitary group of degree 1. Therefore electromagnetism is classified as U(1) gauge theory. Because all operators within the group commute, i.e. the order in which they are applied is irrelevant, we further specify it as abelian U(1) gauge theory.

So far we have only considered one example: electromagnetism which describes the electromagnetic interactions between fermions mediated by photons. In a similar fashion as outlined above, one obtains gauge theories for the electroweak or strong interaction. In fact, gauge theories are a fundamental concept in high energy physics and describe all interactions between elementary particles, which are mediated by gauge bosons.

However, gauge theories also play a crucial part outside the physics of the standard model. General relativity can be viewed as gauge theory[21] with a tensor gauge field obtained by the requirement of local invariance under arbitrary curvilinear coordinate transformations. Another example is Kitaev's toric code for quantum computation, which is a gauge theory of Z_2 symmetry[22]. Moreover, gauge theories emerge as powerful effective descriptions of strongly-correlated condensed matter systems which still defy our understanding. For instance, abelian U(1) and Z_2 lattice gauge theories capture the behaviour of certain quantum spin liquids[23,24] and fractional quantum Hall states can be described by a U1 gauge theory, the Chern-Simons theory, for several filling factors.

In summary, gauge theories are important in a variety of physical fields, ranging from high energy, relativity to condensed-matter. Unfortunately, their computation can be extremely challenging in the strong coupling limit, which is e.g. the regime relevant for quantum chromodynamics (QCD) in particle physics or for the emergent gauge theory describing spin ice in condensed-matter physics. Classical numerical methods like quantum Monte Carlo are partially successful and can predict some equilibrium properties, but usually fail to describe e.g. out of equilibrium phenomena as the thermalization after heavy-ion collisions[15]. A quantum simulation of gauge theories and their dynamics could overcome this limitation. Moreover, there are also gauge theories that constitute effective single-particle de-

scriptions of strongly-correlated many-body systems, describing adequately their phenomenology. In this case, a quantum simulation would allow the experimental investigation of properties arising in such strongly correlated systems without the need to engineer those directly. In this way e.g. anyonic excitations could be explored without the challenging task to implement a fractional quantum Hall system. Therefore, the realization of gauge theories in a quantum simulator is highly desirable.

1.2 Simulation of gauge theories

The last years have seen an increased effort towards the simulation of gauge theories with digital and analogue quantum simulators[15–19]. Here, we will focus mainly on their realization with ultracold quantum gases, but we will also give examples from trapped ions and superconducting qubits when relevant.

Most of recent efforts of simulating gauge theories have focused on abelian gauge theories with U(1) gauge invariance akin to quantum electrodynamics (QED). QED is a prototypical example of a dynamical gauge theory. These gauge theories constitute an important class as most gauge theories in nature are of this kind. In this class, the gauge fields are dynamical entities and have propagating solutions even in the absence of matter.

To simulate a dynamical gauge theory one has *a priori* to realize experimentally a system with a minimum of two different species which represent matter and gauge particles and in addition engineer the interactions between those such that they fulfil gauge invariance. The dynamics of matter and gauge particles is linked, which is very challenging to achieve. For simplicity, most experiments until now have focused on the realization of dynamic gauge theories akin to QED either in system systems of minimalistic size which constitute the first building block for scaling up their implementation and/or in one dimension, where the simulation is greatly simplified as the gauge field cannot have its own dynamics.

There have been many proposal about how to simulate dynamical gauge theories, experimentally three different approaches were so far employed which differ in how the gauge invariance is maintained:

- *Encoding*. This approach can be used in one dimension, where QED looses its dynamical character. Here, the electric field has only one component which is aligned with the single physical dimension of the system and no magnetic fields appear. For the gauge field to be dynamical photons would need to propagate in the orthogonal direction, which does not exist. Consequently, the gauge field does not have its own dynamics, i.e. it has no propagating degrees of freedom in vacuum.

In this case, one can use the local symmetry constrain, e.g. for QED the Gauss law (see eq. (1.8)), to eliminate the gauge field degrees of freedom and express the gauge field solely in terms of the matter field.
This approach of encoding was used in ion-trapped quantum computers[25,26], where a lattice one-dimensional version of QED - the Schwinger model - was implemented[27]. A building block of the same model was simulated with the IBM quantum computer based on superconduting qubits[28].

- *Energy penalties*. In this scheme gauge invariance is ensured by making states which do not fulfil the gauge symmetry energetically inaccessible. Recently, it was successfully employed by fine-tuning of Bose-Hubbard parameter in an ultracold optical lattice system[29,30], where it allowed the implementation of a one-dimensional extended U(1) lattice gauge theory. The simulated theory is as quantum-link model akin to QED, so the gauge field is quantized and truncated to a spin $1/2$. Interestingly, Rydberg chain experiments[31], where the Rydberg blockade strongly suppressed symmetry breaking processes, can be interpreted as a version of the same model[32]. Building blocks of Z_2 lattice gauge theories[33,34] with ultracold atoms in optical lattices were also demonstrated with the energy penalty approach.

- *Symmetry approach*. In this method a symmetry or equivalently a conservation law is employed so only processes which preserve gauge invariance are allowed. Following this idea, a building block of U(1) lattice gauge theory[35] in an ultracold atomic gas using angular momentum conservation was implemented.

Although the described experiments constitute a remarkable progress, these approaches are difficult to further scale up and hence simulating QED as well as strongly coupled gauge theories in higher dimensions remains an open challenge.

Apart from the dynamical gauge theories, in nature there exists a specific subclass of gauge theories which is of topological nature. Here the gauge field is fully linked to the matter and cannot propagate in the absence of it. However, topological gauge fields are not just trivial background potentials which can be eliminated by an appropriate choice of the wavefunction's phase factor as their interaction with matter strongly modifies the properties of the system. Topological gauge theories play an important role in condensed-matter physics where they emerge as effective low-energy description of certain strongly-correlated systems[36–38].

A prime example of topological field theory is the Chern-Simons gauge theory often used to describe two-dimensional fractional quantum Hall states. The fractional quantum Hall effect occurs for a strongly interacting electron gas confined on a two-dimensional plane and subjected to a strong external magnetic field. The Hall conductance in such systems was found to be quantized and as function of the

magnetic field shows a series of plateaus at fractional values of $h/(e^2\nu)$ with filling factor ν of fractional value. Remarkably, the excitations of the system have fractional charge and anyonic exchange statistics. The Chern-Simons theory provides a simple and appealing effective single-particle description of the key features of fractional quantum Hall systems[39]. The effective description builds upon Wilczek's idea of *flux attachment*, where each strongly interacting particle is replaced by a weakly interacting *composite* particle carrying an integer number of flux quanta from the external magnetic field. The Chern-Simons theory governs the coupling between matter and the magnetic field generated by the flux tubes. It is an Abelian U(1) gauge theory where the local symmetry constraint ensures the flux attachment. According to it, the vector potential that is minimally coupled to matter has a complex density dependence so that the Chern-Simons magnetic field scales linearly with the matter density. We will further discuss this gauge theory in chapter 2.

The simulation of Chern-Simons theory and in general of topological gauge theories is simpler compared to dynamical gauge theories. As the gauge fields do not have propagating degrees of freedom in the absence of matter even beyond one spatial dimension, the approach of encoding can always be employed and the theory can be reformulated with solely matter degrees of freedom. However, this is done at the expense of introducing unusual and very often non-local interactions between the particles. Thus, a gauge theory formulation is more natural and the simulation of such effective theories provides further insights into the description of the system.

Simulating Chern-Simons theory with engineered quantum systems requires the implementation of specific density-dependent artificial magnetic fields. Recent experiments have realized an important step in this direction by engineering density-dependent vector potentials in lattice systems, where they are equivalent to an imaginary tunneling amplitude which depends on the sum of the particle occupation in the adjacent lattice sites. These so-called density-dependent Peierls phases were implemented on different experimental platforms, including ultracold atoms[40,41], superconducting qubits[42], and Rydberg atoms[43]. However, in all described experiments, no attempts were made to implement the required local symmetry constraints needed to promote a density-dependent gauge field to a gauge theory. The goal of this thesis is to fill in this gap.

1.3 Aim and outline of this thesis

This thesis explores a degenerate gas of bosonic potassium for the simulation of topological gauge theories. The prototypical example, the Chern-Simons theory, is too demanding for an immediate experimental realization. This motivates us to

investigate theoretically end experimentally one of the simplest topological gauge theories available, the so-called chiral BF theory, which is a one-dimensional reduction of Chern-Simons theory in the continuum[44–48]. Our goal is to exploit the chiral BF theory as toy model for the quantum simulation of topological gauge theories with ultracold atoms, making it play a role similar to the Schwinger model in the quantum simulation of QED.

An important difference to previous experiments is that we consider directly a gauge theory in the continuum, instead of focusing on a lattice formulation of it. This has two key advantages. First, it directly gives access to the continuous limit, removing discretization artefacts associated to the lattice. And second, since the formulation of Chern-Simons theory in the lattice is considerably more involved than in the continuum[49–51], it prepares the path for its future implementation in our system.

For the simulation of the chiral BF theory, the approach of *encoding* can be employed, so the use of one single species which represents the matter particles is sufficient. However, it requires the engineering of unusual interactions which are chiral in nature. The term chiral might be ambiguous. Here and in the following, we adopt the convention established in Refs. [44–48] and refer to interactions as chiral if atoms moving in one direction have different collisional properties compared to atoms moving in the opposite directions. These chiral interactions can be implemented by combining the following two ingredients: first, interaction control obtained with coherent coupling in a Bose-Einstein condensate with unequal intrastate interactions. And second, the locking of momentum and internal state introduced by Raman coupling: optical coherent coupling *via* a two-photon process.

The encoded Hamiltonian of the chiral BF theory can equivalently be described in terms of a minimally coupled gauge potential which linearly depends on density. Hence, simulating the chiral BF theory implies the engineering of either chiral interactions or a density-dependent vector potential with $\hat{A} \propto \rho$.

In this thesis we investigate the encoded Hamiltonian of the chiral BF theory. Building upon the proposal from the Öhberg group in Ref. [52], we theoretically show that a Bose-Einstein condensate with two Raman-coupled internal states with unbalanced intrastate interaction strengths can effectively be described by the encoded Hamiltonian of this gauge theory on the quantum level, and this in a parameter regime that is realistic for our experiment. We further present an experimental realization of the chiral BF gauge theory in a Bose-Einstein condensate of ^{39}K by engineering chiral interactions. To this end we will proceed as follows:

- In chapter 2 we introduce the Chern-Simons gauge theory and demonstrate the difference between dynamical and topological gauge theories by compar-

ing the field theory of electromagnetism to the Chern-Simons theory. Afterwards, we derive the chiral BF gauge theory as one possible dimensional reduction of the Chern-Simons theory. From the Lagrangian we derive an Hamiltonian with an encoding similar to that of Refs. 25–27 for the Schwinger model, where the gauge field is eliminated in terms of the matter field using the local symmetry constraint of the theory. We show that the Hamiltonian features chiral interactions or equivalently a vector potential which depends linearly on density. We comment on the properties of the chiral BF theory from a gauge theory perspective.

- In chapter 3 we outline the approach we follow to encode the chiral BF gauge theory in our experimental system. It is based on the combination of Raman coupling and unbalanced intrastate interaction strengths in the coupled states of a ^{39}K Bose-Einstein condensate (BEC)[52]. We derive the effective Hamiltonian from a microscopic perspective, which allows us to map the experimental system to the BF theory for experimentally realistic parameters.

- After introducing the theoretical framework, in chapter 4 we describe the main characteristics of our experimental apparatus which are relevant for the work described in this thesis. Afterwards, we study the first main experimental ingredient for simulating the BF theory: the interaction control in a BEC of ^{39}K using coherent coupling between two internal states with different intrastate interaction strengths. To describe the concept, in this chapter we focus on the simplest situation of rf-coupling.

- In chapter 5 we turn to the second key ingredient, the implementation of Raman coupling between two internal states of the BEC, which leads to a locking of the spin composition of the system and the momentum of the particles. In this chapter we detail its experimental implementation. In particular, we find the settings for magnetic field, internal states and Raman wavelength that minimize the effect of magnetic field fluctuations and the atomic loss due to inelastic scattering from the Raman beams.

- In chapter 6 we explore Raman-coupled BECs without interactions. We present our experiments to observe the signatures of the modified dispersion relation due to the Raman coupling at the single particle level.

- In chapter 7 we combine the interaction control and Raman coupling in a BEC of ^{39}K and report on the experimental simulation of the chiral BF gauge theory. In our measurements we observe its defining properties: chiral solitons and the back-action between matter and gauge field as required by the local symmetry constraint.

- In chapter 8 we conclude this thesis by summarizing our work, present an outlook to the horizon of this field and outline the possible next research directions with our specific experimental setup as opened up by the work presented in this thesis.

2 Chern-Simons and BF gauge theory

This chapter introduces the chiral BF gauge theory as one dimensional reduction of the topological Chern-Simons gauge theory which emerges in the effective description of fractional quantum Hall states. We derive the equations of motion for the matter and BF gauge field from the Lagrangian density. Based on the topological nature of the theory, we eliminate the gauge field in terms of the matter field and obtain an encoded Hamiltonian which is local and describes a bosonic matter field featuring chiral interaction or equivalently coupled to a vector potential linear in density.

The chiral BF theory is a possible dimensional reduction of U(1) Chern-Simons theory and constitutes one of the simplest examples of topological field theory[44–48]. As discussed in chapter 1, topological field theories are very particular types of gauge theories. They describe the coupling of matter fields to gauge fields that do not have propagating degrees of freedom in vacuum. Instead, their dynamics is linked to that of matter through the local symmetry constraint of the theory, which also ensures its gauge invariance. In this chapter, we start by reviewing the prototypical example of topological gauge theories - the Chern Simons theory - and compare it to the well-known dynamical gauge theory of electromagnetism. We then introduce the chiral BF theory, obtained by reducing Chern-Simons theory from two to one spatial dimensions and supplementing the resulting Lagrangian with a chiral boson term[46–48]. Afterwards, we derive an encoded Hamiltonian for the chiral BF theory which could be realized on quantum simulators. Finally, we discuss its signatures as observable in possible experiments.

The content of this chapter is part of our manuscript "Encoding a one-dimensional topological field theory in a Raman-coupled Bose-Einstein condensate", which is prepared for submission and for which I am co-author. We here recall the main parts of this publication without major modifications, and extend certain discussions. The presented work is an experiment-theory collaboration between our group (Craig Chisholm, Dr. Elettra Neri, Dr. Ramón Ramos and myself, under the guidance of Prof. Leticia Tarruell), and Prof. Alessio Celi from UAB.

2.1 Maxwell and Chern-Simons gauge theory in comparison

Historically, the Chern-Simons gauge theory was specifically constructed as description for anyons - particles with fractional statistics[39]. A different physical origin for the Chern-Simons theory is the dimensional reduction of electromagnetism from $3+1$ dimensional spacetime to $2+1$ dimensions. Therefore we start with the Lagrangian of Maxwell theory as derived in chapter 1 and review its main features as dynamical gauge theory. We then introduce Maxwell-Chern-Simons theory as generalization in $2+1$ dimension. Afterwards, we concentrate on pure Chern-Simons theory and point out how it relates to the description of anyons and fractional quantum Hall systems. Finally, we derive the equations of motion from the Lagrangian in an analogous way to the case of Maxwell theory.

2.1.1 Maxwell theory.

We have already considered the U(1) abelian field theory of electromagnetism, i.e. Maxwell theory, as example of a prototypical dynamical gauge theory in the previous

chapter 1. For completeness, we recall its Lagrangian density (see eq. (1.7))

$$\mathcal{L}_{\mathrm{M}} = -\frac{1}{4}F_{\mu\nu}F^{\mu\nu} - A_\mu J^\mu + \mathcal{L}_{\mathrm{matter}}, \tag{2.1}$$

with the matter field Ψ, which we take to be non-relativistic and bosonic, minimally coupled to a U(1) gauge field A_μ with $\mu = 0..d$, where $\mu = 0$ denotes the time and $\mu = 1, 2, 3$ the spatial components x,y,z. Moreover,the current is defined by $J^0 = \rho = \Psi^*\Psi$, and $\mathbf{J} = [\Psi^*(\nabla - i\mathbf{A})\Psi - ((\nabla + i\mathbf{A})\Psi^*)\Psi]/(2mi)$, where m is the mass of the matter particles, and $F_{\mu\nu} = \partial_\mu A_\nu - \partial_\nu A_\mu$ is the electromagnetic field tensor. The term $\mathcal{L}_{\mathrm{matter}}$ is the Lagrangian density for the matter field alone, as previously defined in eq. (1.5). Here and in the following repeated indices are summed, indices are raised and lowered with the mostly negative Minkowski metric, spatial vectors are denoted in bold and with the index up. We have also set the reduced Planck constant $\hbar$, the speed of light c, the vacuum permittivity ϵ_0, the vacuum permeability μ_0 and the electron charge e to 1.

To clarify the content of the theory, we here follow Faddeev and Jackiw[53,54] and rewrite the Lagrangian density in first order formalism, i.e. in a form analogous to the Legendre transform of a Hamiltonian density

$$\begin{aligned}\mathcal{L}_{\mathrm{M}} =& A^0\left(\boldsymbol{\nabla}\cdot\mathbf{E} - \rho\right) - \mathbf{E}\cdot\dot{\mathbf{A}} - \frac{1}{2}\left(\mathbf{E}^2 + \mathbf{B}^2\right) \\ &+ i\Psi^*\dot{\Psi} + \frac{1}{2m}\Psi^*\left(\nabla - i\mathbf{A}\right)^2\Psi - V(\rho).\end{aligned} \tag{2.2}$$

To do so, we introduced the electric and magnetic fields $E^i = (\mathbf{E})^i = -F^{0i} = -(\dot{A}^i + \partial_i A^0)$ and $B^i = (\mathbf{B})^i = (\nabla\times\mathbf{A})^i = -\frac{1}{2}\epsilon^{ijk}F^{jk}$, where ϵ^{ijk} is the Levi-Civita symbol. Moreover, we used $E^2 = A^0\boldsymbol{\nabla}\cdot\mathbf{E} - \mathbf{E}\nabla A^0$, where we have omitted the total derivative $\nabla\left(A^0\mathbf{E}\right)$ because it does not contribute to the action. In this form of the Lagrangian density, the term $-\mathbf{E}\cdot\dot{\mathbf{A}}$ has the desired symplectic form for the gauge field that will allow us to rewrite the Lagrangian in canonical form (see next section).

Eq. (2.2) does not contain terms of the form $\partial_\mu A^0$, and therefore A^0 plays the role of a Lagrangian multiplier. It enforces the local symmetry constraint of the theory ensuring its gauge invariance. Concretely, it imposes

$$\boldsymbol{\nabla}\cdot\mathbf{E} = \rho, \tag{2.3}$$

which is the Gauss law.

The equations of motion for the matter and gauge fields are simply

$$i\dot{\Psi} + \frac{1}{2m}(\nabla - i\mathbf{A})^2\Psi - \frac{\mathrm{d}V(\rho)}{\mathrm{d}\rho}\Psi = 0$$

$$\begin{aligned} \boldsymbol{\nabla}\cdot\mathbf{E} &= \rho,\ \boldsymbol{\nabla}\times\mathbf{B} - \dot{\mathbf{E}} = \mathbf{J} \\ \boldsymbol{\nabla}\cdot\mathbf{B} &= 0,\ \boldsymbol{\nabla}\times\mathbf{E} + \dot{\mathbf{B}} = 0. \end{aligned} \tag{2.4}$$

For the gauge field we obviously recover Maxwell's equations. They show that, in the absence of matter, only the transverse (divergenceless) part of the gauge field has propagating solutions: the electromagnetic waves. In tensor form, they correspond to the solutions of $\partial_\mu F^{\mu\nu} = 0$ (plus $\partial_\mu F_{\nu\sigma} + \partial_\nu F_{\sigma\mu} + \partial_\sigma F_{\mu\nu} = 0$)[55] that, as we will see below, is very different from the in vacuum equation of motion encountered in topological gauge theories. For $d = 2$ or 3, the gauge field is thus *dynamical*, making electromagnetism a *dynamical gauge theory*. In one spatial dimension $d = 1$, however, no transverse electric field nor magnetic fields appear and thus in vacuum the gauge field has no dynamics.

2.1.2 Chern-Simons theory

When restricting the dynamics of electromagnetism from 3 spatial dimensions to an infinite plane, the most general Lagrangian which fulfils the same gauge invariance is given by

$$\mathcal{L}_{\text{MCS}} = -\frac{1}{4}F_{\mu\nu}F^{\mu\nu} - A_\mu J^\mu + \frac{1}{4\kappa}\epsilon^{\mu\nu\sigma}A_\mu F_{\nu\sigma} + \mathcal{L}_{\text{matter}}, \tag{2.5}$$

for a non-relativistic and bosonic matter field and where now $\mu = 0, 1, 2$ denote the time and the two spatial dimensions. Due to the dimensional reduction, the electric field $\mathbf{E}$ and vector potential $\mathbf{A}$ have two spatial components. The magnetic field has now only one spatial component that is perpendicular to the system's plane, that is, aligned with the $\hat{z}$ direction. In eq. (2.5), we have an additional term scaling with $1/(4\kappa)$ in comparison to the Lagrangian electromagnetism (2.1) in $3+1$ dimensional spacetime. The coefficient κ of the gauge field term is the so-called Chern-Simons level. This term leads to effectively massive photons with mass $1/(2\kappa)$. Therefore, the photons cease to propagate for large mass and the fields $\mathbf{E}, B$ are decaying exponentially with the distance from charge sources. However, as the term includes the electromagnetic field tensor which depends on the derivative of the gauge field $\mathbf{A}$, this one can still take large value away from the sources.

In the following, we focus on the particular case in which no external fields are applied. Hence, we drop the Maxwell term and only consider a matter field Ψ minimally coupled to the Chern-Simons gauge field A_μ that is "internal", i.e. self-generated by the system. This theory is called *pure Chern-Simons theory* or in the following just Chern-Simons theory. As electromagnetism it is an U(1) abelian gauge theory, but instead of being dynamical, it is of topological nature. The pure Chern-Simons theory for a non-relativistic and bosonic matter field is also known

as Jackiw-Pi model[56,57] and its Lagrangian density reads

$$\mathcal{L}_{\mathrm{CS}} = \frac{1}{4\kappa}\epsilon^{\mu\nu\sigma}A_\mu F_{\nu\sigma} - A_\mu J^\mu + \mathcal{L}_{\mathrm{matter}}. \tag{2.6}$$

As we did above for electromagnetism, we separate the A^0 term from the Lagrangian. We then obtain the Lagrangian density

$$\mathcal{L}_{\mathrm{CS}} = -A^0\left(\frac{B}{\kappa}+\rho\right) - \frac{1}{2\kappa}\mathbf{A}\times\dot{\mathbf{A}} + i\psi^*\dot{\psi} + \frac{1}{2m}\psi^*\left(\nabla - i\mathbf{A}\right)^2\psi - V(\rho). \tag{2.7}$$

From the Lagrangian multiplier we again obtain the the local symmetry constraint of the theory, i.e. the equivalent to the Gauss law for electromagnetism. In the case of Chern-Simons theory, it is

$$B = -\kappa\rho, \tag{2.8}$$

so the Chern-Simons magnetic field B is proportional to the matter density.

By integrating eq. (2.8), we find that the flux $\Phi = \int d^2\mathbf{x}B$ at the position of the source and the total charge $Q = \int d^2\mathbf{x}\rho$ are related *via*

$$\Phi = -\kappa Q. \tag{2.9}$$

Now we can understand what was described only qualitatively in the previous chapter: the local symmetry constraint fulfilled by the Chern-Simons term causes every charged particle to carry a magnetic flux. The Chern-Simons level κ indicates the number of flux tubes, i.e. the quanta of the magnetic field, that are attached to each matter particle. Therefore, the local symmetry constraint is known as *flux attachment* because it highlights the fact that B is given by the flux tubes attached to the matter particles[58]. From the concept of *flux attachement* two points follow. First, Chern-Simons theory causes statistical transmutation, i.e. effectively changes the statistics of the particles coupled to it. The particles with the attached flux tubes can be considered as new composite particles. Imagine we have two of those composite particles in a plane. When transporting one on a closed contour around the other enclosing the flux $\Phi = -\kappa Q$, it picks up a geometric phase of $\exp(iQ\Phi) = \exp\left(-i\kappa Q^2\right)$, as in the Aharonov-Bohm effect. Therefore, an exchange of these composite particles would lead to a phase factor of $\exp\left(-i\kappa Q^2/2\right)$, where κ and thus the phase factor can take any arbitrary value which is a defining property of anyons. Hence, bosons/fermions coupled to a Chern-Simons field, i.e carrying a flux described by the Chern-Simons theory, can be anyons. For the specific values of $\kappa = \pi$, $\kappa = 2\pi$ we obtain fermions and bosons, respectively.

Second, the mechanism of *flux attachement* becomes relevant in the effective

description of fractional quantum Hall systems. There, the strongly interacting electrons of the original system, which are subjected to an external magnetic field perpendicular to the two-dimensional plane, can equivalently be described by weakly-interacting effective particles composed out of electrons with an integer number of flux quanta from the external field attached to them[58]. Remarkably, the peculiar properties of fractional quantum Hall states become natural in terms of such composite bosons with attached flux tubes. For instance, the fractional transverse conductance plateaus simply correspond to the filling of the composite particle's Landau levels, and the quasi-particles' anyonic character emerges from the Aharonov-Bohm phases that are picked up upon exchange of flux tubes[39] as outlined above. Chern-Simons theory is the field theory describing the coupling of the matter particles to the magnetic field generated by the flux tubes.Therefore, the *flux attachement* makes the Chern-Simons theory play a key role in the description of fractional quantum Hall states.

We now turn to the equations of motion of the Chern-Simons theory. In the absence of matter, the equation of motion for the gauge field is $F_{\mu\nu} = 0$, which is locally trivial. Thus, the existence of solutions for A_μ that are globally non trivial only depends on the topology of the space. This is very different to electromagnetism where we have propagating solutions already in the vacuum (namely $\partial_\mu F^{\mu\nu} = 0$ and $\partial_\mu F_{\nu\sigma} + \partial_\nu F_{\sigma\mu} + \partial_\sigma F_{\mu\nu} = 0$[55]).

In the presence of matter, the Chern-Simons field acquires non-trivial dynamics. This can be seen by explicitly writing the equations of motion for the matter and gauge fields

$$\begin{aligned} & i\dot{\psi} + \frac{1}{2m}(\nabla - i\mathbf{A})^2\psi - \frac{\mathrm{d}V(\rho)}{\mathrm{d}\rho}\,\psi = 0 \\ & \mathbf{E} - \kappa\,\hat{z}\times\mathbf{J} = 0 \\ & B + \kappa\rho = 0, \end{aligned} \tag{2.10}$$

with $\hat{z}$ the unit vector along the z direction. The equation for the electric field, combined with the continuity equation for the matter field $\partial_0\rho + \boldsymbol{\nabla}\cdot\mathbf{J} = 0$, is equivalent to the equation of motion for the magnetic field. Thus, one sees that the flux attachment condition is simultaneously the equation of motion of the gauge field and the local symmetry constraint of the theory. This is a property of topological gauge theories, i.e theories that do not have independent propagating degrees of freedom for the gauge field, and is analogous to what happens for electrodynamics in one dimension.

2.2 Chiral BF theory

In the 90's, Refs. [44,45] introduced a possible reduction of Chern-Simons theory from two to one spatial dimension that could conserve its main topological features.

This theory is obtained from the Jackiw-Pi model of eq. (2.6) by removing the dependence in the y spatial coordinate setting $A_2 = m\mathcal{B}$, where $\mathcal{B}$ is a new bosonic field. Making the additional replacements $A^0 \to A^0 - m\mathcal{B}^2/2$ and $\kappa \to m\kappa$, the Lagrangian density becomes

$$\mathcal{L}_{\text{BF}} = \frac{1}{2\kappa}\mathcal{B}\epsilon^{\mu\nu}F_{\mu\nu} - A_\mu J^\mu + \mathcal{L}_{\text{matter}}, \tag{2.11}$$

with $\mu = 0, 1$. Due to the form of the gauge field term (which replaces the Chern-Simons form $\epsilon^{\mu\nu\sigma}A_\mu F_{\nu\sigma}$, see eq. (2.6)) this model receives the name of BF theory. Because it does not include any derivative of $\mathcal{B}$, the equation of motion of the gauge field is $F_{\mu\nu} = 0$ even in the presence of matter. This means that in this one-dimensional problem the $\mathcal{B}$ and A_μ fields can be completely decoupled from matter, eliminating them from the problem by a phase redefinition of Ψ. The matter-matter interactions would then be solely determined by V, making the theory trivial. Refs. [44–48] therefore add to the theory a kinetic term for the gauge field, which is of the form $\dot{\mathcal{B}}\mathcal{B}'$ and of strength λ. Here and in the following, the prime indicates the spatial derivative, e.g. $\mathcal{B}' \equiv \partial_1\mathcal{B}$. This so-called chiral boson term explicitly breaks the Galilean invariance and is the simplest non-relativistic combination that endows the system with chiral dynamics, so the behaviour of the edges of the original 2D system is reproduced. The resulting model is the so-called chiral BF theory, whose Lagrangian density reads

$$\mathcal{L}_{\text{cBF}} = \frac{1}{2\kappa}\mathcal{B}\epsilon^{\mu\nu}F_{\mu\nu} + \frac{\lambda}{2\kappa^2}\dot{\mathcal{B}}\mathcal{B}' - A_\mu J^\mu - V(\rho). \tag{2.12}$$

Alternatively, we can specify the electromagnetic field tensor in components and obtain when neglecting global spatial derivatives

$$\mathcal{L}_{\text{cBF}} = A^0\left(\frac{\mathcal{B}'}{\kappa} - \rho\right) - \frac{\mathcal{B}}{\kappa}\dot{A} + \frac{\lambda}{2\kappa^2}\dot{\mathcal{B}}\mathcal{B}' + i\psi^*\dot{\psi} + \frac{1}{2m}\psi^*(\partial_1 - iA)^2\psi - V(\rho). \tag{2.13}$$

Here, the vector potential A is now a scalar as in $d = 1$ it has only one component. From eq. (2.13) we readily identify the local symmetry constraint of the chiral BF theory

$$\mathcal{B}' = \kappa\rho, \tag{2.14}$$

which is the equivalent to the *flux attachment* condition in Chern-Simons theory or the Gauss law in electromagnetism.

The equations of motion for the matter and gauge fields read

$$i\dot{\psi} + \frac{1}{2m}(\partial_1 - iA)^2\psi - \frac{\mathrm{d}V(\rho)}{\mathrm{d}\rho}\psi = 0$$

$$\begin{aligned} &\dot{\mathcal{B}} + \kappa J = 0,\ \mathcal{B}' - \kappa\rho = 0 \\ &E - \frac{\lambda}{\kappa}\dot{\mathcal{B}}' = 0 \end{aligned} \tag{2.15}$$

where the electric field E and the spatial part of the current $J = \left[\Psi^*(\partial_1 - iA)\Psi - ((\partial_1 + iA)\Psi^*)\Psi\right]/(2mi)$ are indicated as scalars because in $d = 1$ they have only one component.

As in the Chern-Simons case, the first of these equations describes the motion of matter coupled to a gauge potential A, and the two equations in the second line can be combined to yield the continuity equation for the matter field $\partial_0\rho + \partial_1 J = 0$. The last equation is the equation of motion of the "electromagnetic" field tensor, which can be rewritten as $F_{01} = E = \lambda\dot{\rho}$. Thus, we see that at the classical level the local symmetry constraint is equivalent to $E = \lambda\dot{\rho}$ or $A = -\lambda\rho + \partial_1\Lambda$ with arbitrary function Λ which only depends on the spatial coordinate.

In conclusion, we see that despite its simplicity the chiral BF theory already contains the main features of a topological field theory. It can thus be used as toy model to benchmark their quantum simulation with quantum gases. However, to achieve this we need to formulate it in Hamiltonian form.

2.3 Derivation of an encoded Hamiltonian for the chiral BF theory

In this section, we tackle the problem of deriving a quantum Hamiltonian for the chiral BF theory that is amenable to quantum simulation with ultracold atoms. Since the theory is subjected to the local constraint eq. (2.14) and the relation between $\dot{A}$ and $\dot{\mathcal{B}}$ and the conjugate momenta of A and $\mathcal{B}$, $-\mathcal{B}/\kappa$ and $\lambda\mathcal{B}'/(2\kappa^2)$ is singular, i.e. it cannot be inverted, it is not straightforward to perform the Legendre transform of eq. (2.13). To deal with the constrained system, we apply the first-order approach due to Faddeev and Jackiw[53,54]. It allows one to separate the dynamics from the local gauge symmetry constraints by progressively eliminating the dependent fields at the level of the Lagrangian. In this way, we avoid the complex Dirac treatment of constraints[59,60]. We end up with a Hamiltonian involving only the physical degrees of freedom of the system, and where the matter-dependent gauge degrees of freedom have been eliminated using the local symmetry constraint. That is, a Hamiltonian that has an *encoded* form similar to the one exploited to simulate the Schwinger model[25,27].

Since the Faddeev-Jackiw approach is not commonly used in quantum simulation, we first apply it to Maxwell's theory and show the emergence of the Gauss law and of Coulomb's Hamiltonian. We then perform an analogous consistent elimination for the chiral BF theory, obtaining the local symmetry constraint eq. (2.14) and

the encoded Hamiltonian.
In both cases, the elimination of the matter-dependent gauge field produces a non-trivial interaction for the matter field: an infinite-range Coulomb interaction in the case of electromagnetism, and an anomalous chiral interaction term in the chiral BF theory. The implementation of the encoded Hamiltonian in an experimental system reduces then to the engineering of the corresponding emerging interaction term.

2.3.1 Maxwell theory

The starting point of the Faddeev-Jackiw approach is the Lagrangian of the system in first-order form, i.e. eq. (2.2) in the case of Maxwell theory. There, the electric field of the system can be decomposed in longitudinal (i.e. stemming from the gradient of a function) and transverse (i.e. divergenceless) parts $\mathbf{E} = \mathbf{E}_\mathsf{L} + \mathbf{E}_\mathsf{T}$, and the Gauss law then used to express the longitudinal part in terms of the matter field $\mathbf{E}_\mathsf{L} = \nabla(\nabla^{-2}\rho)$. Here $\nabla^{-2}\rho$ is simply minus the electrostatic potential. By substituting in the Lagrangian and decomposing also the vector potential in longitudinal and transverse parts, $\mathbf{A} = \mathbf{A}_\mathsf{L} + \mathbf{A}_\mathsf{T}$, we find up to total derivatives

$$\begin{aligned}\mathcal{L}_\mathsf{M} = &-\mathbf{E}_\mathsf{T}\cdot\dot{\mathbf{A}}_\mathsf{T} + i\psi^*\dot{\psi} + \rho\nabla^{-2}(\boldsymbol{\nabla}\cdot\dot{\mathbf{A}}_\mathsf{L}) \\ &- \frac{1}{2}\left(\mathbf{E}_\mathsf{T}^2 - \rho\nabla^2\rho + \mathbf{B}^2\right) + \frac{1}{2m}\psi^*\left(\nabla - i\mathbf{A}\right)^2\psi - V(\rho). \quad (2.16)\end{aligned}$$

Here, we have exploited that the inverse Laplacian can be integrated by parts like the other differential operators, $\int \mathrm{d}^3\mathbf{r} f\nabla^{-2}g = \int \mathrm{d}^3\mathbf{r}\,\nabla^{-2}f\,g$. The expression eq. (2.16) shows that the transverse components of the gauge field and the matter field are the dynamical degrees of freedom of the theory: the pairs $(\mathbf{A}_\mathsf{T}, -\mathbf{E}_\mathsf{T})$ and $(\psi, i\psi^*)$ are equivalent to position and momentum of a mechanical system, (q, p). While the first two terms in eq. (2.16) have the canonical form $p\dot{q}$, the third term does not because there is no momentum field conjugated to $\mathbf{A}_\mathsf{L}$. This simply reflects the fact that the longitudinal component of the gauge field is not physical. The key point of the Faddeev-Jackiw treatment is that such non-canonical terms can always be removed by field redefinitions.

Indeed, if we redefine the matter field through the gauge transformation $\psi = \exp\left[i\nabla^{-2}(\boldsymbol{\nabla}\cdot\mathbf{A}_\mathsf{L})\right]\phi$, we obtain

$$\begin{aligned} i\psi^*\dot{\psi} + \rho\nabla^{-2}(\boldsymbol{\nabla}\cdot\dot{\mathbf{A}}_\mathsf{L}) &= i\phi^*\dot{\phi} \quad \text{and} \\ \frac{1}{2m}\psi^*\left(\nabla - i\mathbf{A}_\mathsf{L}\right)^2\psi &= \frac{1}{2m}\phi^*\nabla^2\phi, \end{aligned} \quad (2.17)$$

where in the second expression we have used that $\nabla^{-2}(\boldsymbol{\nabla}\cdot\mathbf{A}_\mathsf{L}) = f_\mathsf{L}$ implies $\boldsymbol{\nabla}\cdot\mathbf{A}_\mathsf{L} = \nabla^2 f_\mathsf{L}$, and thus $\mathbf{A}_\mathsf{L} = \nabla f_\mathsf{L}$.

Substituting this into eq. (2.16), the Lagrangian density takes the canonical form

$$\mathcal{L}_{\mathrm{M}} = -\mathbf{E}_{\mathrm{T}} \cdot \dot{\mathbf{A}}_{\mathrm{T}} + i\phi^* \dot{\phi} - \mathcal{H}_{\mathrm{C}}^{\mathrm{enc}} \tag{2.18}$$

and we can read off the encoded Hamiltonian density

$$\mathcal{H}_{\mathrm{C}}^{\mathrm{enc}} = \frac{1}{2}\left(\mathbf{E}_{\mathrm{T}}^2 - \rho\nabla^{-2}\rho + \mathbf{B}^2\right) - \frac{1}{2m}\phi^*\left(\nabla - i\mathbf{A}_{\mathrm{T}}\right)^2\phi, \tag{2.19}$$

which is nothing else than Coulomb's Hamiltonian. Interestingly, this result has been derived without assuming any gauge choice.

The derivation above is valid also when we restrict ourselves to two or one spatial dimensions. In $d = 1$, there is no traverse component and the Hamiltonian simply contains the kinetic term of matter and the Coulomb interaction, which is of infinite range as $E_{\mathrm{L}} = \int \mathrm{d}x\, \rho$ and thus $-\rho\nabla^{-2}\rho = (\int \mathrm{d}x\, \rho)^2$. It has precisely the same form as the interaction term in the lattice Hamiltonian of the Schwinger model after encoding[27], where the integral of the density is replaced by the sum of the charges (represented as spins by a Jordan-Wigner transformation) over the sites of the lattice. It is the experimental implementation of such exotic interaction term that makes the realization of the encoded Hamiltonian difficult, a challenge that was successfully tackled with trapped ions[25,26]. In $d > 1$, encoded formulations of the Maxwell lattice gauge theory Hamiltonians that exploit the electromagnetic duality have been proposed[61–64], while link model dual formulations have been investigated in Refs. [65,66].

2.3.2 Chiral BF theory

We now apply the Faddeev-Jackiw procedure to the Lagrangian of the chiral BF model eq. (2.11) in order to derive the corresponding encoded Hamiltonian. Since only the matter field enters canonically in the Lagrangian density, this is the dynamical field, as the BF equations of motion eq. (2.15) also indicate.

In order to consistently formulate the theory in Hamiltonian form, separating the dynamics from the constraints, we start by redefining the matter field as

$$\Psi = \exp\left[i\left(\int_{x_0}^{x} \mathrm{d}y\, A(y,t) + \int_{t_0}^{t} \mathrm{d}t' A^0(x_0,t') - \frac{\lambda}{2\kappa}\mathcal{B}(x_0,t)\right)\right]\psi, \tag{2.20}$$

where x_0 and t_0 are specific values of the space and time coordinates. This gauge transformation, which is similar to the one performed in Ref. [48] on the equations of motion, allows us to rewrite the Lagrangian (up to total derivatives) in the form

$$\mathcal{L}_{\mathrm{cBF}} = \tilde{A}^0\left(\frac{\mathcal{B}'}{\kappa} - \rho\right) - \frac{\lambda}{2\kappa}\dot{\mathcal{B}}(x_0,t)\rho + \frac{\lambda}{2\kappa^2}\dot{\mathcal{B}}\mathcal{B}' + i\psi^*\dot{\psi} + \frac{1}{2m}\psi^*\psi'' - V(\rho), \tag{2.21}$$

with the Lagrange multiplier $\tilde{A}^0 \equiv -\int_{x_0}^{x} \mathrm{d}y\, F_{01}(y,t)$. We thus see that the effect of the gauge transformation eq. (2.20) is to separate the dynamical part of the gauge field, proportional to the bosonic gauge field $\mathcal{B}$, from the "trivial" part represented by the Lagrange multiplier $\tilde{A}_0$. The latter imposes the constraint $\mathcal{B}' = \kappa\rho$ or, equivalently,

$$\mathcal{B}(x,t) = \kappa \int_{x_0}^{x} \mathrm{d}y\, \rho(y,t) + \mathcal{B}(x_0,t), \tag{2.22}$$

which as we explained in section 2.2, is the local symmetry constraint of the chiral BF theory. To derive the encoded Hamiltonian, we replace the symmetry constraint eq. (2.22) in eq. (2.21), obtaining a Lagrangian where the gauge field has been completely eliminated and only the matter field appears

$$\mathcal{L}_{\mathrm{cBF}} \quad = \quad i\,\psi^* \left(\partial_0 - i\frac{\lambda}{2}\int_{x_0}^{x} \mathrm{d}y\, \dot{\rho}(y,t)\right)\psi \;+\; \frac{1}{2m}\psi^*\psi'' \;-\; V(\rho). \tag{2.23}$$

However, the resulting expression is non-local, and thus not easily amenable to quantum simulation. Moreover, the canonical quantization of eq. (2.23) would lead to a quantum field that is not bosonic. This was to be expected, since in two spatial dimensions Chern-Simons theory is a field theory for anyons, and its one-dimensional reduction, the chiral BF theory, was originally constructed as a possible model for anyons in a line[44,45]. Indeed, although in the original papers the quantum mechanical model proposed as microscopic realization of the theory was not correct[46–48], the chiral BF theory has been subsequently shown to be the field theory corresponding to the Kundu model, a well-defined microscopic model for linear anyons, in the regime of weak interactions[67].

Our final step to derive an encoded Hamiltonian suitable for the quantum simulation of the chiral BF theory is to remove the non-locality of eq. (2.23) by performing the Jordan-Wigner transformation

$$\psi = \exp\left[i\frac{\lambda}{2}\int_{x_0}^{x} \mathrm{d}y\, \rho(y,t)\right]\phi, \tag{2.24}$$

after which the matter field ϕ is again bosonic. This yields the local Lagrangian density

$$\mathcal{L}^{\mathrm{enc}}_{\mathrm{cBF}} = i\,\phi^*\dot{\phi} - \mathcal{H}^{\mathrm{enc}}_{\mathrm{cBF}} \tag{2.25}$$

from which we read off a Hamiltonian density that is canonical and can be quantized

$$\begin{aligned}\mathcal{H}^{\mathrm{enc}}_{\mathrm{cBF}} &= -\frac{1}{2m}\phi^*\left(\partial_1 + i\frac{\lambda}{2}\rho\right)^2\phi + V(\rho)\\ &= -\frac{1}{2m}\phi^*\phi'' + \frac{\lambda}{2}J\rho + \tilde{V}(\rho).\end{aligned} \tag{2.26}$$

Here $J = \left(\phi^* \phi' - \phi^{*'} \phi\right)/(2mi)$ is the spatial current for the non-relativistic boson ϕ and $\tilde{V}$ includes now a positive cubic term, $\tilde{V}(\rho) = V(\rho) + \lambda^2 \rho^3/(8m)$. Thus, the encoded model corresponds to that of a bosonic field with effective chiral and three-body interactions besides the original ones

$$\mathcal{H}_{\text{int}} = \mathcal{H}_{\text{int}}^{\text{chiral}} + \mathcal{H}_{\text{int}}^{\text{3B}} + V(\rho) = \frac{\lambda}{2} J \rho + \frac{\lambda^2}{8m} \rho^3 + V(\rho). \tag{2.27}$$

For small values of λ, the three-body term $\mathcal{H}_{\text{int}}^{\text{3B}} \propto \lambda^2$ becomes negligible, and the encoded model reduces to that of a bosonic field with additional chiral interactions $\mathcal{H}_{\text{int}}^{\text{chiral}} \propto \lambda$. Therefore, and similarly to the Maxwell case, the elimination of the gauge field through the local symmetry constraint produces an interaction in the encoded Hamiltonian, which in the case of the chiral BF theory is not Coulomb-like but dominantly of current-density form. This interaction is chiral and breaks Galilean invariance as the chiral BF theory before the encoding does. For localized wavepackets, it is equivalent to a density-density term with a coupling that changes with the velocity of the wavepacket itself (see section 2.4 for further details). Conversely, a non-relativistic boson displaying a current-density interaction is described by a chiral BF theory, i.e. we can measure all the observables of the latter in the former.

The encoded Hamiltonian eq. (2.26) provides a simple prescription for obtaining the quantum chiral BF theory, since it is sufficient to normal order it to have a second-quantized Hamiltonian operator[47,48]. Through the local constraint, we can then determine the expectation value of all the observables. For instance, the expectation value of the electric field of the chiral BF theory before encoding can be obtained by measuring the time derivative of the expectation value of the density $\langle \hat{E} \rangle = \lambda \langle \hat{\rho} \rangle$. Note that an analogous strategy was used to determine the electric field when simulating the encoded Schwinger model with trapped ions[25,27].

Interestingly, the chiral interaction in eq. (2.26) can alternatively be interpreted as the coupling of the matter field ϕ to a density-dependent vector potential $\mathcal{A} = -\lambda\rho/2$. Indeed, it was precisely this property of the encoded theory that inspired the first theoretical proposal for its implementation in a Raman-coupled BEC with imbalanced interactions[52]. However, note that this vector potential $\mathcal{A}$ of the encoded Hamiltonian is not equal to the gauge potential of the chiral BF theory $A = -\lambda\rho$ which we inferred from the equation of motion of the "electromagnetic" field tensor, see eq. (2.15).

2.4 Properties of a chiral BEC from a gauge theory perspective

Chiral BECs have been predicted to display a number of unconventional properties, including the existence of chiral solitons[52,68–70], density-dependent persistent currents and anomalous expansion dynamics[52], unconventional collective modes[71–73], and peculiar vortex patterns[74,75]. Previous works from the group of Prof. Öhberg group viewed these properties as a result of the current-density interaction term of eq. (2.27) or, equivalently, of the coupling of the matter field to the density-dependent gauge potential of the encoded Hamiltonian $\mathcal{A}$. Here, we show that the correspondence to the underlying chiral BF gauge theory provides a more intuitive interpretation of these results. Specifically, we review the main observables of the chiral BF theory that can be accessed by performing measurements on a chiral BEC, and discuss their potential experimental observation.

2.4.1 Chiral solitons.

One of the defining properties of the chiral BF theory is the existence of chiral soliton solutions for the matter field[46–48]. We first shortly introduce solitons and afterwards detail how chiral solitons arise as solution of the encoded Hamiltonian of the chiral BF theory.

Solitons are stationary solutions for a condensate in effectively one dimension and propagate without dispersion, i.e. without modifying their shape[76]. Bose-Einstein condensates in effectively one dimension can exhibit two different types of solitons: dark and bright solitons. Dark solitons exist in BECs with repulsive interactions. They manifest themselves as dip in the condensate density and are accompanied by an abrupt change of its phase[77,78]. In contrast, bright solitons can arise in BECs with attractive interactions and constitute a self-bound wavepacket, or in other words a density peak[79]. In this thesis, we will focus on bright solitons.

In order to understand better how bright solitons arise, we briefly review the energy of the ground state of a BEC in an external trapping potential V, with attractive interaction strength $g < 0$ and without Raman coupling. We assume that the trapping potential V strongly confines the transversal dynamics and allows the evolution along an unconfined (or very weakly confined) in x-direction, so $V = m\omega_r^2 r^2/2$ with radial trapping frequency ω_r and negligible trapping frequency ω_x in x-direction. Following Ref. [80], its static properties are governed by the time-independent Gross-Pitaevskii equation

$$\mu\Phi = \left(-\frac{\hbar^2}{2m}\nabla^2 + V + g\rho\right)\Phi \tag{2.28}$$

with the chemical potential μ. Here, we have not set $\hbar$ to 1. The energy of the system is given by $E = \int d^3\mathbf{r}\mathcal{E}$ with energy density

$$\begin{aligned}\mathcal{E} &= \mathcal{E}_{\text{kin}} + \mathcal{E}_{\text{trap}} + \mathcal{E}_{\text{int}} \\ &= \frac{\hbar^2}{2m}|\nabla^2\Phi|^2 + V\rho + \frac{g}{2}\rho^2.\end{aligned} \tag{2.29}$$

We can obtain the stable solutions of the system by minimizing the energy defined by eq. (2.29). To this end we follow a variational approach and take a Gaussian Ansatz for the wavefunction: $\Phi = \sqrt{N}/(\pi^{3/4}\sqrt{\sigma_x\sigma_r^2})\exp\left(-x^2/(2\sigma_x^2) - r^2/(2\sigma_r^2)\right)$, where the variational parameter are the longitudinal and radial widths σ_x and σ_r. With this Ansatz we find for the energy[80]

$$E(\sigma_x, \sigma_r) = N\hbar\omega_r\left[\frac{1}{4}\left(\frac{2a_{\text{ho}}^2}{\sigma_r^2} + \frac{a_{\text{ho}}^2}{\sigma_x^2}\right) + \frac{1}{4}\frac{2\sigma_r^2}{a_{\text{ho}}^2} + \frac{a_{\text{ho}}^3}{\sqrt{2\pi}\sigma_r^2\sigma_x}\frac{Na}{a_{\text{ho}}}\right] \tag{2.30}$$

with harmonic oscillator length $a_{\text{ho}} = \sqrt{\hbar/m\omega_r}$ and scattering length a defined by $g = 4\pi\hbar^2 a/m$. In eq. (2.30) we identify the dimensionless ratio

$$\eta = \frac{N|a|}{a_{\text{ho}}} \tag{2.31}$$

as relative measure between the contributions from interactions on the one hand and kinetic and trapping effects on the other hand. Whereas for $\eta \gg 1$ interactions dominate, they can safely be neglected for $\eta \ll 1$.

For a BEC with attractive interactions ($g < 0$), the ratio η determines whether there exists a stable solution for the condensate. For $\eta > 1$ the system will collapse as the energy in eq. (2.30) has no minimum as also observed experimentally[81–83]. However, a condensate can have a stable solution for attractive interaction if the dispersion caused by quantum pressure $\mathcal{E}_{\text{kin}} \propto (1/\sigma_r^2 + 1/\sigma_x^2)$ in the trap compensates the attractive non-linearity $\mathcal{E}_{\text{int}} \propto 1/(\sigma_r^2\sigma_x)$. In this case a bright soliton is formed. The variational Ansatz presented above predicts that a local minimum only exists below a critical value of η_c[80,84], similarly to what happens for a BEC in a three-dimensional trap[85]. For the waveguide geometry as considered in this thesis, the value is $\eta_c \approx 0.776$. The variational calculation is known to overestimate the stability of the soliton[85], numerical calculations give a value of $\eta_c \approx 0.627$[85,86]. The collapse criterion shows that solitons can only exist if the interaction energy $g\rho \approx gN/a_{\text{ho}}^3$ is smaller than the transversal trapping energy $\hbar\omega_r$. Thus, solitons can only form in quasi one dimensional geometries.

We now turn to chiral solitons. These are self-bound wavepackets of the matter field that propagate without dispersion only when moving along one direction. On the contrary, wavepackets with the opposite centre of mass momentum cannot form solitons and spread. Thus, chiral solitons are collective excitations of the

one-dimensional system and can be seen as "particles" which only exist for a given propagation direction.
Chiral solitons are solutions of the classical equation of motion for the matter field of the encoded BF Hamiltonian eq. (2.26), which is an effective one-dimensional extended Gross-Pitaevskii equation of the form[46,52]

$$i\hbar\dot{\phi} = -\frac{\hbar^2}{2m}\left(\partial_x - i\mathcal{A}\right)^2\phi + \left(g\rho + \frac{\hbar\lambda}{2}J\right)\phi, \tag{2.32}$$

where we have neglected the external transverse trapping potential V. Here, and to simplify the comparison with the available literature, we use the same notation as in section 2.3 but restoring $\hbar$. The vector potential $\mathcal{A}$ of the encoded Hamiltonian is density-dependent and thus cannot be removed by a standard gauge transformation. However, by performing a non-local transformation, i.e. a Jordan-Wigner transformation of form $\Phi = \exp\left(-i\int_{-\infty}^{x} \mathrm{d}x\,\mathcal{A}\right)\phi$, we can eliminate $\mathcal{A}$ from the kinetic term. We then obtain

$$i\hbar\dot{\Phi} = -\frac{\hbar^2}{2m}\Phi'' + (g\rho + \hbar\lambda J)\Phi. \tag{2.33}$$

If we consider a matter wavepacket of centre of mass momentum k and group velocity $v = \hbar k/m$, the current reads $J = \rho\hbar k/m = \rho v$. Then, eq. (2.33) becomes completely analogous to the usual Gross-Pitaevskii equation in eq. (2.28) but with $\tilde{g} = g + \lambda\hbar^2 k\rho/m$. The additional momentum-dependent part of the coupling constant corresponds to the chiral interaction term of the matter field in the encoded theory $\mathcal{H}_{\text{int}}^{\text{chiral}} = \lambda\hbar^2\rho^2 k/2m$, see section 2.3. When $\tilde{g} < 0$, the system supports a bright soliton solution. If the condensate at rest has $g \geq 0$, reversing its group velocity will yield a repulsively interacting system ($\tilde{g} > 0$) where no soliton solutions exist[52], as we indeed observed experimentally (see chapter 7). Thus, the bright soliton solution of eq. (2.33) is chiral, and constitutes the many-body analogue of edge states in quantum Hall systems. It directly reflects the chirality of the underlying gauge theory, which can be traced back to the self-dual term $\dot{\mathcal{B}}\mathcal{B}'$ of the chiral BF model before encoding, eq. (2.21).

2.4.2 Electric field.

In its encoded form, the chiral BF theory involves only matter fields. However, the relation between the gauge and matter classical fields derived in section 2.3 translates into a relation between the expectation values of the corresponding quantum fields. Specifically, one has $\langle\hat{E}\rangle = \lambda\langle\dot{\hat{\rho}}\rangle$ and can therefore determine the BF electric field by measuring the temporal evolution of the matter density $\hat{\rho}$. Changes in the matter density induce an electric force that acts back into the chiral BEC and endows it with rich dynamics, especially when the system is confined in a harmonic trap.

For instance, Refs. [71–73] showed that the current-density term of the eGPE eq. (2.32) leads to a coupling of the monopole and dipole collective modes of the system, eventually leading to chaotic dynamics. Here, we interpret this coupling in terms of the induced BF electric field. Indeed, in a chiral BEC, the compression of the gas due to the excitation of the breathing mode generates a synthetic electric field. The corresponding electric force displaces the centre of mass of the cloud and excites the dipole mode. Thus, the coupling of the monopole and dipole modes is a direct manifestation of the back action between matter and gauge fields.

An even stronger manifestation of the BF electric field is the distortion of the density profile of the cloud upon expansion of the chiral BEC into an optical waveguide, an effect that we study in chapter 7 experimentally following the theoretical prediction of Ref. [52]. In this situation, the density of the gas drops in the centre of the cloud and increases on its edges, leading to an inhomogeneous distribution of electric forces. These forces skew the density profile of the chiral BEC, which develops an asymmetric shape during the expansion.

2.5 Conclusion

In this chapter we illustrated the differences between dynamical and topological gauge theories by analysing the Lagrangian of electromagnetism and Chern-Simons theory. Afterwards, we introduced a prototypical version of a topological gauge theory: the chiral BF theory constructed in Ref. [44–47]. The theory is obtained from a dimensional reduction of the Abelian U1 Chern-Simons theory and supplemented with a chiral boson term. We explicitly derived the Hamiltonian from the constrained Lagrangian by applying the Faddev-Jackiw formalism[53,54]. In the encoded Hamiltonian, all gauge field degrees of freedom are eliminated and expressed through the matter degrees of freedom by the local symmetry constraint of the theory. This encoding approach as we have chosen is analogous to the encoding of the Schwinger model implemented in trapped ion digital quantum simulators[25,31]. Whereas the encoding in the Schwinger model leads to long range interactions, local but chiral interactions are introduced in the case of the chiral BF theory. In the end, we summarized the proposed properties of BECs with such chiral interactions. We focused on chiral solitons and the modified expansion dynamics and discussed how the latter one can be used to extract the gauge fields of the chiral BF theory.

3 Approach to simulate the chiral BF theory in a Bose-Einstein condensate

This chapter presents our approach for realising the chiral BF theory in a Bose-Einstein condensate based on effective interactions which are chiral in nature. We engineer those by combining optical coherent coupling via *two Raman beams and state dependent interactions. We first focus on single particle effects of the Raman-coupled condensate and establish a description for a Raman-coupled BEC in momentum space. Afterwards we derive an effective one-component Hamiltonian for the whole system including interactions. We show that the effective Hamiltonian describes chiral interactions and for certain parameters corresponds to the encoded Hamiltonian of the chiral BF theory derived in the previous chapter.*

In this section, we establish a theoretical description for a two-component Bose-Einstein condensate with interactions, subjected to an external magnetic field and optically coupled *via* two counter-propagating Raman beams. After introducing the basics of the Raman coupling in section 3.1, we focus in section 3.2.1 and 3.2.2 on single particle effects introduced by the Raman coupling. We review the Raman-dressed dispersion relation in the dressed state picture and the commonly used series expansion of the lower dispersion branch around zero momentum which allows to interpret the Raman-dressed atoms as particles with an effective mass and subjected to a synthetic static gauge potential. Afterwards in section 3.3, we include interactions in the Raman-coupled states into the description and introduce a series expansion around a generic value of the momentum. From this and following our manuscript "Encoding a one-dimensional topological field theory in a Raman-coupled Bose-Einstein condensate", we derive an effective single-component Hamiltonian and investigate how it maps to the Hamiltonian of the chiral BF theory.

3.1 Raman coupling scheme

In our experiment, we start with a Bose Einstein-condensate subjected to a homogenous external field B in a harmonic trap. We then coherently couple two hyperfine sub-levels $\sigma = \{|\downarrow\rangle, |\uparrow\rangle\}$ of the ground-state manifold, which are separated by an energy $\hbar\omega_0$, as illustrated in the left panel of Fig. 3.1. For the coherent coupling, we employ two counter-propagating Raman laser beams with wavelength λ_R and slightly different frequencies ω_1, ω_2 with $\Delta\omega = \omega_1 - \omega_2$ and wavevectors k_1, k_2, respectively. The setup is sketched in Fig. 3.1 on the right. Each single Raman beam is off-resonant to any atomic transition. If the frequencies of the two Raman beams are chosen such that $\Delta\omega = \omega_0$, the two-photon detuning $\delta_0 = \Delta\omega - \omega_0$ is zero and the transition between the coupled states $|\downarrow\rangle$,$|\uparrow\rangle$ is resonantly driven.

In the resonant case, we can understand the Raman coupling in the following intuitive way: the atoms in state $|\downarrow\rangle$ get excited to a virtual intermediate level by absorbing a photon with frequency ω_1 from the first Raman beam and fall into the $|\downarrow\rangle$ state by subsequent stimulated emission of a photon with frequency ω_2 in the second counter-propagating laser beam. In this Λ-type coupling, the change of the internal spin state is locked to a momentum transfer from the Raman beams. Thus the internal state dictates the momentum of the atom and vice versa. The momentum transfer is the difference between the Raman wavevectors k_1 and k_2. In the case of a system's geometry as shown in Fig. 3.1, i.e. counter-propagating Raman beams along the x-direction, the momentum transfer is maximized and equals twice the Raman recoil momentum $k_R = 2\pi/\lambda_R$

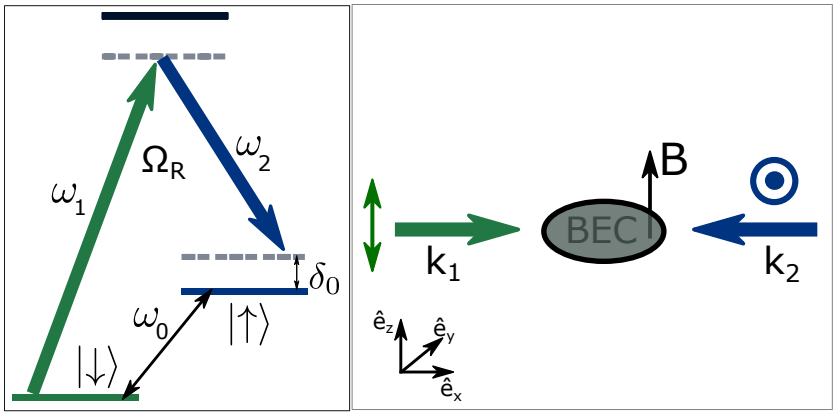

Figure 3.1: Raman two-photon coupling scheme. **Left:** two levels $|\downarrow\rangle, |\uparrow\rangle$, separated in energy by $\hbar\omega_0$, are coupled by two Raman lasers via a higher virtual level. The Raman beams have frequencies ω_1, ω_2 and couple the states with two-photon coupling strength Ω_R. **Right:** The Raman beams are counter-propagating along $\hat{e}_x$, have orthogonal polarization and wavevectors k_1,k_2, respectively. The magnetic field is applied along the $\hat{e}_z$-axis. For counter-propagating beams, each spin transfer is accompanied with a momentum change of twice the recoil momentum k_R.

3.2 Description of single particle effects in a Raman-dressed BEC

In the following, we only consider the specific system's geometry shown in Fig. 3.1, which is the one that is experimentally implemented in this thesis.

3.2.1 Raman coupling in the dressed state picture

In this section, we investigate the Hamiltonian of a two-component BEC subjected to Raman coupling in momentum space to obtain its eigenstates and the energy-momentum relation. As introduced in section 3.1, the two coupled internal states always differ in momentum by $2k_R$ due to the momentum transfer from the Raman photons.Therefore it is convenient to work in the quasi-momentum frame, where the basis is composed out of $\sigma \in \{|\downarrow, k_x - k_R\rangle, |\uparrow, k_x + k_R\rangle\}$. Here, k_x is the quasi-momentum along x-direction of the particle in the Raman-dressed dispersion relation. In the following, we omit the momenta and just refer to the states as $|\downarrow\rangle$ and $|\uparrow\rangle$.

We consider the combined atom-Raman light Hamiltonian In the frame rotating at $\Delta\omega$[87,88]. In the basis of $|\uparrow\rangle, |\downarrow\rangle$ and in momentum space, the single-particle Hamiltonian (kinetic energy and Raman coupling) are described by

$$\hat{H}_{\text{kin}} = \int \frac{d^3\mathbf{k}}{(2\pi)^3} \sum_{\sigma_1,\sigma_2} \hat{\phi}^\dagger_{\sigma_1}(\mathbf{k}) \mathcal{H}_{\text{kin},\sigma_1,\sigma_2} \hat{\phi}_{\sigma_2}(\mathbf{k}) \tag{3.1}$$

with the field operator $\hat{\phi}_\sigma^\dagger(\mathbf{k})$ ($\hat{\phi}_\sigma(\mathbf{k})$) which creates (annihilates) a particle in state $|\sigma\rangle$ and $\mathcal{H}_{\text{kin},\sigma_1,\sigma_2}$ denoting a matrix element of

$$\mathcal{H}_{\text{kin}} = \begin{pmatrix} \frac{\hbar^2}{2m}(\mathbf{k}_\perp^2 + (k_x + k_R)^2) - \hbar\delta_0/2 & \hbar\Omega_R/2 \\ \hbar\Omega_R/2 & \frac{\hbar^2}{2m}(\mathbf{k}_\perp{}^2 + (k_x - k_R)^2) + \hbar\delta_0/2 \end{pmatrix}. \tag{3.2}$$

Here $\mathbf{k}_\perp$ is the momentum perpendicular to the x-direction, which is not affected by the Raman coupling. From Hamiltonian (3.2) it is evident that the Raman light splits the energy levels by the detuning $\hbar\delta_0$ and couples them by $\hbar\Omega_R$.

The single photon recoil energy of the Raman beams, namely $E_R = \hbar^2 k_R^2/2m$, defines the natural energy unit of the system. It is $E_R/h = 8.2$ kHz and $E_R/h = 8.6$ kHz for ^{41}K and ^{39}K, the two potassium isotopes we use in our experiment. In the remaining part of this chapter, we express energies and momenta in units of E_R and k_R, respectively. Moreover, we set E_R, k_R and $\hbar$ to unity. Then we have $\mathbf{k}_\perp = \mathbf{k}_\perp^{'} k_R \equiv \mathbf{k}_\perp^{'}$, $k_x = k_x^{'} k_R \equiv k_x^{'}$ and for the energies $\hbar^2\mathbf{k}_\perp^2/2m = \mathbf{k}_\perp^{'2} E_R \equiv \mathbf{k}_\perp^{'2}$ and similarly $\hbar^2 k_x^2/2m = k_x^{'2} E_R \equiv k_x^{'2}$. In the following we omit the apostrophes and obtain for the Hamiltonian matrix in these dimensionless units:

$$\mathcal{H}_{\text{kin}} = \begin{pmatrix} \mathbf{k}_\perp^2 + (k_x + 1)^2 - \delta_0/2 & \Omega_R/2 \\ \Omega_R/2 & \mathbf{k}_\perp{}^2 + (k_x - 1)^2 + \delta_0/2 \end{pmatrix}. \tag{3.3}$$

The bare states $\sigma \in \{|\uparrow\rangle, |\downarrow\rangle\}$ are not eigenstates of matrix (3.3). However, the matrix can be diagonalized by a basis rotation to the dressed basis $\hat{\phi}_\pm(k_x) = \sum_\sigma U_{\pm,\sigma}(k_x)\hat{\phi}_\sigma(k_x)$ defined by the unitarity transformation:

$$U(k_x) = \begin{pmatrix} \sin\theta(k_x) & -\cos\theta(k_x) \\ \cos\theta(k_x) & \sin\theta(k_x) \end{pmatrix}. \tag{3.4}$$

The two new eigenstates $|-\rangle, |+\rangle$ fulfil $H|\pm\rangle = \mathcal{E}_\pm|\pm\rangle$ and are a superposition of the bare states. We refer to them as lower and higher dressed state respectively. The matrix entries of U are a function of the mixing angle θ and can be expressed as $\sin(\theta) = \frac{1}{\sqrt{2}}\sqrt{1-P}$ and $\cos(\theta) = \frac{1}{\sqrt{2}}\sqrt{1+P}$, respectively. The polarization P indicates the spin composition of the system. For a value of $P = -1$ the atom is in state $|\downarrow\rangle$, for $P = +1$ in state $|\uparrow\rangle$. At $P = 0$ the atom is in a 50/50 superposition between $|\uparrow\rangle$ and $|\downarrow\rangle$. For a given ratio of detuning to coupling strength, the polarization is determined by the quasi-momentum, because the Raman beams couple the spin to momentum. More precisely, the polarization can be expressed as $P = \tilde{\delta}/\tilde{\Omega}_R$ with the generalized detuning $\tilde{\delta}(k_x) = \delta_0 - 4k_x$ and generalized Rabi frequency $\tilde{\Omega}_R(k_x) = \sqrt{\Omega_R^2 + \tilde{\delta}^2(k_x)}$, where detuning and coupling strength in their generalized form are functions of the quasi-momentum. The special case of $P = 0$ occurs at $\tilde{\delta} = 0$, so for $k_x = \delta_0/4$ or in the case of $\delta_0 = 0$ and $k_x = 0$.

It is important to notice that the momentum dependence of $\tilde{\delta}$ is a characteristic

of coherent coupling *via* Raman beams. For a coherent coupling realized without momentum transfer, e.g. with radio-frequency as we investigate in section 4.2.2, the generalized detuning reduces to $\tilde{\delta}(k_x) = \tilde{\delta} = \delta_0$. Subsequently we have $\tilde{\Omega}_R(k_x) = \tilde{\Omega}_R = \sqrt{\Omega_R^2 + \delta_0^2}$ and the polarization is constant for all values of k_x.

For the Raman-dressed system, the single particle eigenenergies corresponding to Hamiltonian (3.3) are

$$\mathcal{E}_\pm(k_x) + \mathbf{k}_\perp^2, \text{ with } \mathcal{E}_\pm(k_x) = k_x^2 + 1 \pm \frac{1}{2}\tilde{\Omega}_R(k_x) \tag{3.5}$$

for $|+\rangle, |-\rangle$ respectively. In analogy to particles in lattice potentials, the dispersion relations $\mathcal{E}_\pm$ are commonly called energy bands.

In all of our experiments, we load the atoms into the lower dressed band and the energy gap $\tilde{\Omega}_R(k_x)$ is larger than all other energy scales and therefore prevents collisions which excite atoms occupying the ground-state to the upper dressed state. Therefore, we limit the description of our system to the lower dressed state $|-\rangle$ and only investigate the lower energy band $\mathcal{E}_-$.

3.2.2 Effective gauge potential and mass of Raman-dressed atoms

The Raman coupling leads to a synthetic vector potential and a modified effective mass of the atoms, as further outlined below.

The connection between atom-light interactions and an effective gauge potential was first pointed out by R. Dum and M. Olshanii in Ref. [89] and P.M. Visser and G. Nienhuis in Ref. [90]. Subsequently, concrete experimental schemes for ultracold quantum gases were proposed [91–95] and the progress of the field reviewed in Refs. [87,88,96]. These results are obtained in position space and in the adiabatic approximation, which is valid for large coupling strengths. We here briefly retrace the conceptual idea, following the review of Prof. Dalibard in Ref. [96]. We consider atoms moving in a laser field with generalized coupling strength $\tilde{\Omega}_R$. The state of the systems for different times t is $\Psi(\mathbf{r}, t) = \sum_n c_n(\mathbf{r}, t)\,|\Psi_n(\mathbf{r})\rangle$ with the probability amplitudes $c_n(\mathbf{r}, t)$ to find an atom at position $\mathbf{r}$ in the internal state $|\Psi_n(\mathbf{r})\rangle$ and the index n runs over all eigenstates of the system. The internal states are just the dressed states $|-\rangle$ $|+\rangle$ in position space, which are position-dependent as the mixing angle θ depends on $\tilde{\Omega}_R(\mathbf{r})$ and in position space the states in addition depend on the laser phase. We now consider the time evolution when the position $\mathbf{r}$ is varying in time. We assume that the change is adiabatic, i.e. atoms follow adiabatically the eigenstate in which they were initially prepared, i.e. $\Psi(\mathbf{r}, t) = c_l(\mathbf{r}, t)\,|\Psi_l(\mathbf{r})\rangle$, if $\Psi(\mathbf{r}, 0) = |\Psi_l(\mathbf{r})\rangle$. In this case, one can derive the

following time evolution for the parameter $c_l(\mathbf{r}, t)$ from the Schrödinger equation:

$$i\frac{\partial c_l(\mathbf{r}, t)}{\partial t} = \left[(\mathbf{k} - \mathbf{A}_l(\mathbf{r}))^2 - \frac{\tilde{\Omega}_R(\mathbf{r}(t))}{2} + \mathcal{V}\right] c_l(\mathbf{r}, t). \tag{3.6}$$

where we have used the dimensionless units of this chapter and $\mathcal{V}$ is a scalar potential. Moreover, we have defined

$$\mathbf{A}_l(\mathbf{r}) = i\langle \Psi_l(\mathbf{r})|\nabla \Psi_l(\mathbf{r})\rangle, \tag{3.7}$$

which is the so-called Berry connection and arises due the implicit time dependence of the state: $\partial_t \Psi(\mathbf{r}, t) = \partial_t c_l(\mathbf{r}, t)\,|\Psi_l(\mathbf{r})\rangle + c_l(\mathbf{r}, t)\mathbf{k}\,|\nabla \Psi_l(\mathbf{r})\rangle$. Eq. (3.6) has the same structure as the Schrödinger equation of a charged particle coupled to the vector potential of electromagnetism. Therefore $\mathbf{A}_l(\mathbf{r})$ can be identified with an effective vector potential. Its name Berry connection points to the fact that atoms under the influence of the vector potential $\mathbf{A}_l(\mathbf{r})$ pick up a geometric phase $\phi_{\text{geom}}(T) \propto \int_0^T \mathbf{k}\mathbf{A}_l(\mathbf{r})dt = \oint \mathbf{A}_l(\mathbf{r})dr$ when completing a contour in position space in time T. The geometric phase does not depend on the time T but only on the trajectory of the atom. This is equivalent to the Berry phase acquired by neutral atoms with magnetic moment slowly moving in an external applied inhomogeneous magnetic field[97]. Therefore, the atom-light interaction in this adiabatic approximation leads to an effective gauge potential of geometric origin.

However, the synthetic gauge potential can also be understood in momentum space. This approach, that was first formulated by Prof. Spielman in Ref. [94], has proven to be very successful and is the one more commonly used to describe the experiments. Here, we follow this approach and review how the synthetic gauge potential and in addition an effective mass arises in terms of the energy-momentum relation $\mathcal{E}_-$ of the lower Raman-dressed state which is strongly modified due to the Raman coupling.

Let us first investigate how the dispersion depends on the coupling field parameters Ω_R and δ_0. The dispersion relation for the lower dressed state for $\delta = 0$ and various coupling strengths is depicted in the left panel of Fig. 3.2. At low coupling strength, namely $\Omega_R \ll 4$, the dispersion exhibits a double-well structure. With increasing Ω_R, the two wells start to merge. At $\Omega_R = 4$, the dispersion has a flat regime, more precisely $\partial^2\mathcal{E}_-/\partial^2 k_x = 0$ at $k_x = 0$. For larger coupling strengths with $\Omega_R > 4$, the dispersion relation develops a single minimum. In all our experiments, we work in the single minimum regime with $\Omega_R > 4$, on which we will concentrate in the following. Above a certain coupling strength, the adiabatic approximation in position space as introduced previously holds. In this regime, the dispersion is parabolic, so the effective mass becomes equal to the real mass of the atoms. In our experimental system, the adiabatic approximation starts to be

valid at values of $\Omega_R \sim 85$, where the corrections due to the non-parabolic shape of the dispersion are below 5%.

We now consider the case of non-zero detuning in the very large Rabi coupling limit. The right panel of Fig. 3.2 shows the dispersion $\mathcal{E}_-$ in the large coupling limit at $\Omega_R = 100$ and different values of the two-photon detuning δ_0. For values of $\delta_0 < 0$ ($\delta_0 > 0$), the minimum of the dispersion k_{min} gets shifted to positive (negative) values of quasi-momentum k_x.

In Fig. 3.3 we show the energy-momentum relations for both dressed states for our typical experimental coupling strength $\Omega_R = 4.5$ and the case $\delta_0 = -1.2$. The dashed lines indicate the energies of the bare states in the quasi-momentum frame. The colour encodes the previously introduced spin polarization P: green represents an atom in state $|\downarrow\rangle$ ($P = -1$), blue an atom in state $|\uparrow\rangle$ ($P = +1$).

For these parameters, namely away from the strong coupling limit and $\delta_0 \neq 0$, the dispersion relation gets modified in two manners. First, the minimum of the dispersion is shifted as described previously. As we outline further below, the shift can be interpreted as synthetic vector potential acting on the atoms. Second, the dispersion relation becomes non-parabolic. This is described by the momentum-dependent curvature of the modified dispersion relation, which is $\partial^2\mathcal{E}/\partial k^2$. Analogously to the parabola of the free particle case, we define the effective mass $m^*(k_x)$

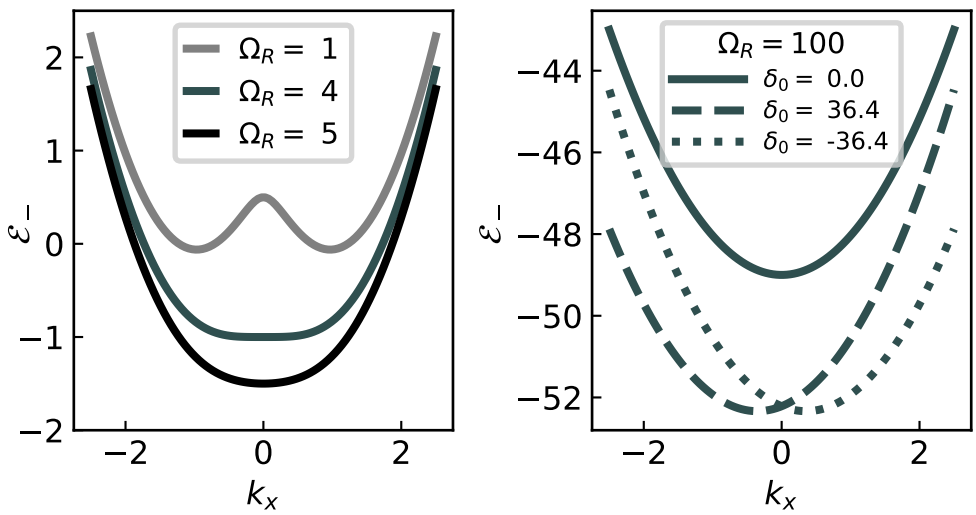

Figure 3.2: Raman-dressed dispersion for different parameter of the coupling field. **Left:** dispersion of the lowest dressed state $|-\rangle$ for $\delta_0 = 0$ and different values of the Raman coupling strength Ω_R. **Right:** dispersion of $|-\rangle$ for $\Omega_R = 100$ and three values of the detuning. Energies and frequencies (Ω_R, δ_0) are given in dimensionless units of E_R and $E_R/\hbar$, respectively.

with $m^*(k_x) = 2(\partial^2\mathcal{E}/\partial k^2)^{-1}$ in dimensionless units. We obtain

$$m^*(k_x) = \left[1 - 4\frac{\Omega_R^2}{\tilde{\Omega}_R^3(k_x)}\right]^{-1}. \tag{3.8}$$

In contrast to the free particle case, the curvature and thus effective mass is not constant, but rather a function of the momentum k_x. In section 6.3, we study the effect of the Raman induced effective mass $m^*(k_x)$ on the expansion dynamics of a condensate, similarly as done in the work by the group of Prof. Engels[98].

A convenient description for the lower energy band in the single minimum regime but away from the parabolic limit is given by the expansion of $\mathcal{E}_-$ around $k_x = 0$, as first introduced by Prof. Spielman in Ref. [94]. To lowest order in $1/\tilde{\Omega}$ and second order in k_x, we find

$$\mathcal{E}_- \approx k_x^2 + 1 - \frac{1}{2}\tilde{\Omega}_R(0) + \frac{2\delta_0}{\tilde{\Omega}_R(0)}k_x - \frac{4}{\tilde{\Omega}_R(0)}k_x^2 \tag{3.9}$$

$$= \left(\frac{\tilde{\Omega}_R(0)}{\tilde{\Omega}_R(0) - 4}\right)^{-1}\left(k_x^2 - \frac{\delta_0}{4 - \tilde{\Omega}_R(0)}\right)^2 + \frac{2 - \tilde{\Omega}_R(0)}{2} + W \tag{3.10}$$

where $W = -(\delta_0^2(\tilde{\Omega}_R(0) - 4))/((4 - \tilde{\Omega}_R(0))^2\tilde{\Omega}_R(0))$ is a constant energy term.

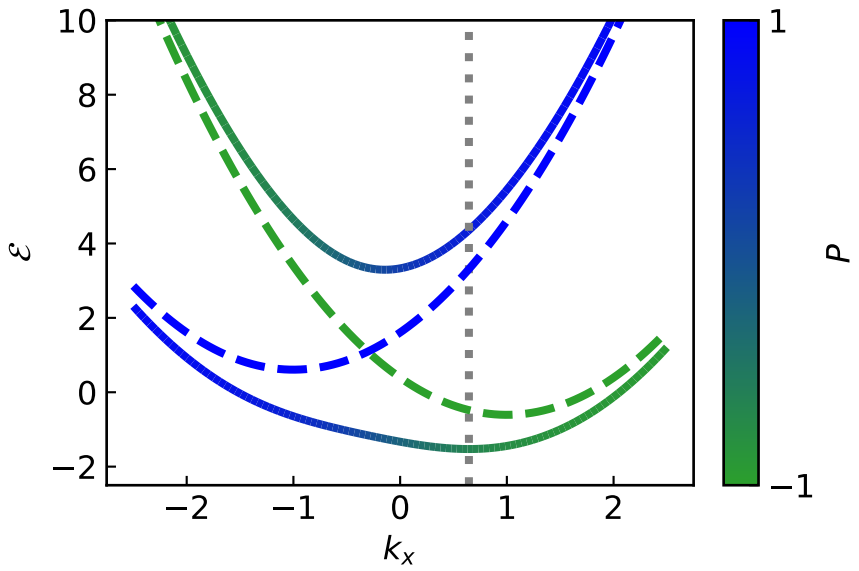

Figure 3.3: Energy-momentum relation for the two Raman-dressed states $|+\rangle, |-\rangle$ for a typical experimental setting with $\Omega_R = 4.5$ and $\delta_0 = -1.2$.The colour encodes the spin polarization P. The dashed lines are the energies of the bare states in the quasi-momentum frame $|\downarrow\rangle, |\uparrow\rangle$. The dotted line indicates the minimum of the energy band.

From the expansion in eq. (3.10), we can deduce the following changes for atoms in the Raman-dressed dispersion:

- The minimum of the Raman-dressed dispersion, which is defined as

$$\partial\mathcal{E}_-/\partial k|_{k=k_{\min}} = 0. \tag{3.11}$$

  is shifted as previously investigated qualitatively. From eq. (3.10) it is evident that

$$k_{\min} = \frac{\delta_0}{4 - \tilde{\Omega}_R(0)}. \tag{3.12}$$

  which implies $k_{\min} = 0$ for $\delta_0 = 0$.

- The atoms have an effective (dimensionless) mass $m_0^* = \frac{\tilde{\Omega}_R(0)}{\tilde{\Omega}_R(0)-4}$. Note that in contrast to the effective mass $m^*(k_x)$ defined in eq. (3.8), m_0^* is not a function of the quasi-momentum. Instead, it is the evaluation of $m^*(k_x)$ at $k_x = 0$ and small values of detuning δ_0. In the large coupling limit, the effective mass approaches 1, which implies the Raman-dressed dispersion becomes parabolic as in the free particle case. This is precisely the regime of the adiabatic approximation in position space.

- The energy of an atom is shifted by the constant contributions $1 - \tilde{\Omega}_R(0)/2$ and W respectively.

Expanding the energy up to second order in k_x is only a good approximation for an expansion point close to the minimum of the dispersion. We have performed the expansion around $k_x = 0$ and therefore eq. (3.10) is only valid for small values of detuning, as $k_{\min} = 0$ only for $\delta_0 = 0$.

Expressing the expansion with the newly introduced parameters $k_{\min}$ and m_0^* gives

$$\mathcal{E}_- = \frac{(k_x - k_{\min})^2}{m_0^*} + 1 - \frac{\tilde{\Omega}_R(0)}{2} + W, \tag{3.13}$$

which has a similar structure as we found in the adiabatic approximation in position space, see eq. (3.6). The dimensionless Hamiltonian describing the gauge field A_0 of electromagnetism has the form $H = (k_x - A_0)^2$, where the charge e has been set to 1. A comparison to eq.(3.13) shows that the shift of the minimum can be associated with an effective static vector gauge potential: $k_{\min} = A_0$. Thus, the atoms in the Raman-dressed dispersion can be described as synthetic particles with a larger effective mass m_0^* and subjected to a synthetic static vector potential $A_0 = k_{\min} = \delta_0/\left(4 - \tilde{\Omega}_R(0)\right)$. This gauge potential is bounded by the momentum difference of the bare states: $-1 \leq A_0 \leq +1$ and its strength can be tuned by the easily controllable Raman light field parameters Ω_R and δ_0. Its experimental

investigation was pioneered by the group of Prof. Spielman[94] in Refs. [99–102].

The scalar potential W can also be expressed in terms of the vector potential A_0. By direct substitution we obtain for it $W = -A_0^2/m_0^*$.

3.3 Full effective single-component Hamiltonian

In the previous paragraphs we have investigated Raman coupling at the single particle level, i.e. considered a system described by $\hat{H} = \hat{H}_{\text{kin}} + \hat{H}_{\text{Raman}}$. However, the full Hamiltonian consists out of a kinetic and an interaction part:

$$\hat{H} = \hat{H}_{\text{kin}} + \hat{H}_{\text{Raman}} + \hat{H}_{\text{int}}, \tag{3.14}$$

where we have neglected any trapping potential for simplicity. The third term $\hat{H}_{\text{int}}$ captures the intra- and interspin interactions in the system in the absence of Raman coupling, and which are microscopically described by contact potentials, parametrized by the dimensionless coupling constants $g_{\sigma_i\sigma_j}$ where $\sigma_i, \sigma_j \in \{\downarrow, \uparrow\}$. As we will see in the remaining part of the chapter, including interactions is the crucial ingredient to endow the synthetic vector potential with an appropriate density dependence and engineer the chiral BF model in its encoded form. To this end, we will derive an effective single-component form of the full Hamiltonian (3.14).

In the adiabatic approximation as introduced for eq. (3.6), an effective description for the interacting system in the lower dressed state was first established by the Öhberg group in Ref. [52]. The authors consider $\hat{H}$ in position space and treat the interaction part as small perturbation. By applying perturbation theory to first order they derive the dressed states $|\chi_\pm\rangle \approx \left|\chi_\pm^{(0)}\right\rangle + \left|\chi_\pm^{(1)}\right\rangle$ where $\left|\chi_\pm^{(1)}\right\rangle = \pm\frac{g_{\downarrow\downarrow}-g_{\uparrow\uparrow}}{8\Omega_R}\rho_\pm \left|\chi_\mp^{(0)}\right\rangle$ admixes the two dressed states with a magnitude depending on the difference of the interaction strengths and the density $\rho_\pm$ of the dressed states. Because these formulas were derived under the assumption that the coupling strength is the dominant energy scale, only the dressed state under consideration is occupied: $\rho_- \approx 0$ or $\rho_+ \approx 0$. By projecting onto the perturbed lowest dressed state $|\chi_-\rangle$, they obtain an effective Hamiltonian, in the dimensionless units of this chapter given by:

$$\hat{H}_\pm \approx (\mathbf{k} - \mathbf{A}_\pm[\mathbf{r}, \rho_\pm(\mathbf{r}, t)])^2 + W \pm \frac{\Omega_R}{2} + \frac{g}{2}\rho_\pm \tag{3.15}$$

with W a scalar potential contribution and $g = (g_{\downarrow\downarrow} + g_{\uparrow\uparrow} + 2g_{\downarrow\uparrow})/4$. The Hamiltonian $\hat{H}_\pm$ describes a system which behaves as if subjected to a vector potential $\mathbf{A}_\pm = \mathbf{A}_0 \pm \mathbf{A}_\rho$ minimally coupled to the momentum. In addition to the standard static vector potential $\mathbf{A}_0 = -\nabla\phi/2$ with the gradient of the Raman laser phase ϕ, this vector potential has a density-dependent contribution

$\mathbf{A}_\rho = \nabla\phi(g_{\downarrow\downarrow} - g_{\uparrow\uparrow})\rho_\pm(\mathbf{r})/8\Omega_R$. As explained in chapter 3, the minimal coupling to a density-dependent vector potential is key for the experimental realization of the chiral BF theory in its encoded form, and therefore the proposal of the Öhberg group in Ref. [52] paves the way for the exploitation of Raman-coupled BECs towards this goal. However, the single-component effective description derived in Ref. [52] is valid only in the limit of extremely large coupling strengths, for our experimental system we would need $\Omega_R \gtrsim 85\ E_R$. Such conditions are unfeasible in our experimental system, due to severe heating of the atomic cloud by the Raman light with consequent atom losses (see chapter 5).

Here, we present a novel effective single-component description for the interacting 1D Raman-coupled system which is able to reveal a more accessible regime of Raman parameters where the minimal coupling to a density-dependent vector potential is still preserved. In contrast to the approach of Ref. [52], this description is developed in the momentum space and along the lines of Spielman's work and in particular of his series expansion as introduced in the previous section. This description was developed in collaboration with Prof. Alessio Celi and our experimental team formed by Prof. Leticia Tarruell, Craig Chisholm, Dr. Elettra Neri and Dr. Ramón Ramos and myself. It is also the subject of the manuscript "Encoding a one-dimensional topological field theory in a Raman-coupled Bose-Einstein condensate", currently in preparation for submission. Below we follow in major parts our manuscript and report in detail on the derivation of the effective single component Hamiltonian.

3.3.1 Derivation in momentum space

For each of the two contributions $\hat{H}_{\text{kin}}$ and $\hat{H}_{\text{int}}$ of Hamiltonian (3.14), we obtain a single-component description by working in second quantization in momentum space and restricting the creation and annihilation operators to the lower dressed state. Furthermore, for both contributions, we perform a series expansion around a generic value of the quasi-momentum k_0. Afterwards we recombine both contributions into one full effective Hamiltonian.

Low momentum expansion for the kinetic part

The kinetic part corresponds to the Hamiltonian in eq. (3.3), i.e. describes the free particle dispersion along y- and z- direction and the single particle effects of the Raman coupling along the x-axis, and was investigated in section 3.2.1. We derive a single-component description by defining in momentum space:

$$\hat{H}_{\text{eff,kin}} = \int \frac{\mathrm{d}^3\mathbf{k}}{(2\pi)^3}\hat{\phi}_-^\dagger(\mathbf{k})[\mathcal{E}_-(k_x) + \mathbf{k}_\perp^2]\hat{\phi}_-(\mathbf{k}). \tag{3.16}$$

with $\mathcal{E}_-$ the energy of the lower dressed state. Our previous expansion of $\mathcal{E}_-$, see eq. 3.13, was obtained from an expansion around $k_x = 0$ and is only valid for small values of detuning δ_0 and quasi-momenta k_x around zero. In this section we want to obtain a more general description and therefore perform an expansion of the energy momentum relation $\mathcal{E}_-$ of the lowest dressed state around a general value of k_x.

For atoms of an ultracold atomic cloud with centre of mass momentum close to k_0 along the x-axis, we can recast the momentum along the Raman coupling direction as $k_x = k_0 + q$, with $q \ll 1$, accounting for any centre of mass momentum away from k_0 and the momentum spread. By substituting this in eq. 3.5, we have for the energy of the lowest dressed state

$$\mathcal{E}_-(k_x) = 1 + k_0^2 + k_\perp^2 + 2qk_0 + q^2 + \frac{1}{2}\tilde{\Omega}_R(k_0)f(u). \tag{3.17}$$

with $f(u) = \sqrt{1 - 8u(\tilde{\delta}/\tilde{\Omega}_R) + 16u^2}$ and $u = q/(\tilde{\Omega}_R(k_0))$. With a Taylor expansion around $u = 0$, we obtain for this function

$$f(u) = f(0) + f^{'}(0)u + \frac{1}{2}f^{''}(0)u^2 + \frac{1}{6}f^{'''}(0)u^3 + \mathcal{O}(u^4), \tag{3.18}$$

taking the expansion parameter u up to the third order into account. Inserting this expansion in the single particle energy gives

$$\begin{aligned}\mathcal{E}_-(k_x) &= \mathcal{E}_-^{(0)} + \mathcal{E}_-^{(1)} + \mathcal{E}_-^{(2)} + \mathcal{E}_-^{(3)} + \mathcal{O}(q^4) \\ &= \mathcal{E}_-(k_0) + 2qk_0 + q^2 + 2\frac{\tilde{\delta}(k_0)}{\tilde{\Omega}_R(k_0)}q - 4\frac{\Omega_R^2}{\tilde{\Omega}_R^3(k_0)}q^2 - 16\frac{\tilde{\delta}(k_0)\Omega_R^2}{\tilde{\Omega}_R^5(k_0)}q^3 + \mathcal{O}(q^4).\end{aligned} \tag{3.19}$$

where $\mathcal{E}_-^{(n)}$ denotes the contribution of n-th order in q. We will use this abbreviation in chapter 7 when estimating the validity of eq. (3.19) for our experimental parameters.
Analogously as in the previous section, we can rewrite this equation in terms of an effective mass which now is determined by k_0:

$$m^*_{k_0} = \left(1 - \frac{4\Omega_R^2}{\tilde{\Omega}_R^3(k_0)}\right)^{-1} \tag{3.20}$$

and obtain for the lowest dressed energy band the same structure as in eq. (3.13):

$$\mathcal{E}_-(k_x) = \mathcal{E}_-(k_0) + \frac{(q - A_0)^2}{m^*_{k_0}} + W + \mathcal{O}(q^4). \tag{3.21}$$

Where we have introduced the static gauge potential

$$A_0 = -m^*_{k_0}\left(k_0 + \frac{\tilde{\delta}(k_0)}{\tilde{\Omega}_R(k_0)} - 8\frac{\tilde{\delta}(k_0)\Omega_R^2}{\tilde{\Omega}_R^5(k_0)}q^2\right), \tag{3.22}$$

and the scalar energy contribution $W = -A_0^2/m^*_{k_0}$. For small values of detuning and for $k_0 = 0$ we recover $m^*_{k_0} = m^*_0$ and $A_0 = -m^*_0\tilde{\delta}(0)/\tilde{\Omega}^3_R(0) = \delta_0/\left(4 - \tilde{\Omega}_R(0)\right)$ to second order in q. Hence, these equations agree with the result from the common expansion around $k_0 = 0$ (eq. 3.13 in the previous section). However, now the parameters $m^*_{k_0}, A_0$ and W depend on the momentum k_0. To third order in q, A_0 acquires a momentum dependence that can be interpreted as the effect of the q-dependent part of the momentum dependent mass $m^*(k_x) = m^*(k_0 + q)$[52] (defined in eq. (3.8)). We can cancel out this effect by setting $\tilde{\delta} = 0$, which corresponds to a balanced superposition of the two states with $P = 0$ or, equivalently, to the choice $k_0 = \delta_0/4$.

By inserting eq. (3.21) into the effective kinetic Hamiltonian of eq. (3.16) and transforming to position space, we obtain

$$\hat{H}_{\text{eff,kin}} = \int \mathrm{d}^3\mathbf{r}\hat{\phi}^\dagger(r)\left[\mathcal{E}_-(k_0) + W - \nabla_\perp^2 - \frac{(\partial_x - iA_0)^2}{m^*_{k_0}}\right]\hat{\phi}(r). \tag{3.23}$$

Here we have dropped the indices of the lower band, so $\hat{\phi}_- = \hat{\phi}, \hat{\phi}^\dagger_- = \hat{\phi}^\dagger$.

Low momentum expansion for the interaction part

The interaction part $\hat{H}_{\text{int}}$ of the Hamiltonian, describing two atoms colliding with incoming and outgoing momenta $\mathbf{k}_1, \mathbf{k}_2$ and $\mathbf{k}_3, \mathbf{k}_4$ respectively, is in second quantization and in momentum space

$$\hat{H}_{\text{int}} = \int \frac{\mathrm{d}^3\mathbf{k}_1}{(2\pi)^3}\frac{\mathrm{d}^3\mathbf{k}_2}{(2\pi)^3}\frac{\mathrm{d}^3\mathbf{k}_3}{(2\pi)^3}\frac{\mathrm{d}^3\mathbf{k}_4}{(2\pi)^3}\hat{V}. \tag{3.24}$$

with

$$\hat{V} = \frac{1}{2}\sum_{\sigma_1,\sigma_2} g_{\sigma_1,\sigma_2}\hat{\phi}^\dagger_{\sigma_1}(\mathbf{k}_4)\hat{\phi}^\dagger_{\sigma_2}(\mathbf{k}_3)\hat{\phi}_{\sigma_1}(\mathbf{k}_2)\hat{\phi}_{\sigma_2}(\mathbf{k}_1)\delta^3(\mathbf{k}_4 + \mathbf{k}_3 - \mathbf{k}_2 - \mathbf{k}_1). \tag{3.25}$$

The delta function in this equation ensures momentum conservation, i.e. the sum of the incoming momenta $k_1 + k_2$ is equal to the sum of the outgoing momenta $k_3 + k_4$.

As a next step, we express $\hat{V}$ in the dressed basis $\hat{\phi}_\pm(\mathbf{k})$ and restrict ourselves to the lowest energy band $\hat{\phi}_-(\mathbf{k})$. This approximation is justified when the energy gap to the upper dressed state $|+\rangle$ is much larger than all interaction energies,

so processes that couple the lower to the higher dressed state are negligible. In the following, we drop the $-$ subscript in the field operators. The interaction Hamiltonian in the dressed basis then reads

$$\begin{aligned}\hat{H}_{\text{int}} = \int \frac{\mathrm{d}^3\mathbf{k}_1}{(2\pi)^3}\frac{\mathrm{d}^3\mathbf{k}_2}{(2\pi)^3}\frac{\mathrm{d}^3\mathbf{k}_3}{(2\pi)^3}\frac{\mathrm{d}^3\mathbf{k}_4}{(2\pi)^3}\frac{1}{2} g_{\text{eff}}(k_{1,x}, k_{2,x}, k_{3,x}, k_{4,x}) \\ \hat{\phi}^\dagger(\mathbf{k}_4)\hat{\phi}^\dagger(\mathbf{k}_3)\hat{\phi}(\mathbf{k}_2)\hat{\phi}(\mathbf{k}_1)\delta^3(\mathbf{k}_4+\mathbf{k}_3-\mathbf{k}_2-\mathbf{k}_1)\end{aligned} \tag{3.26}$$

where we have introduced the generalized interaction strength

$$g_{\text{eff}}(k_{1,x}, k_{2,x}, k_{3,x}, k_{4,x}) = \sum_{\sigma_1,\sigma_2} g_{\sigma_1,\sigma_2} U_{-,\sigma_1}(k_{4,x}) U^\dagger_{-,\sigma_1}(k_{2,x}) U_{-,\sigma_2}(k_{3,x}) U^\dagger_{-,\sigma_2}(k_{1,x}) \tag{3.27}$$

which is the effective coupling constant of the system, describing the interactions between atoms in the lower Raman-dressed band. In particular, g_{eff} is a function of the quasi-momenta of the colliding atoms. It is interesting to notice that eq. (3.27) also describes the interactions among atoms in the lower band for the case of vanishing momentum transfer ($k_R = 0$), i.e. in the case of rf-coupling. In that case, g_{eff} results in $g_{--} = g_{\uparrow\uparrow}\cos^4(\theta) + g_{\downarrow\downarrow}\sin^4(\theta) + (1/2)g_{\downarrow\uparrow}\sin^2(2\theta)$ with the mixing angle θ independent of the momentum. This case will be the object of study in section 4.2.2.

Up to now, the modified coupling constant was investigated only in this particular case of rf-coupling and $g_{\uparrow\uparrow} \neq g_{\downarrow\downarrow}$ [103–106] or for non-zero Raman transfer $k_R \neq 0$ but identical intra- and interspin interactions ($g_{\uparrow\uparrow} = g_{\downarrow\downarrow} = g_{\downarrow\uparrow}$) [107]. In this work, we present the first investigation of the modified coupling constant for both $k_R \neq 0$ and $g_{\uparrow\uparrow} \neq g_{\downarrow\downarrow}$ (see chapter 7 for the experimental study).

As previously done for the kinetic part, we write for the momenta along the Raman coupling direction $k_x = k_0 + q$ and expand the interaction Hamiltonian to first order in $q/\tilde{\Omega}_R(k_0)$. We obtain

$$\begin{aligned} g_{\text{eff.}}(k_{1,x}, k_{2,x}, k_{3,x}, k_{4,x}) &= g^{(0)}_{\text{eff.}} + g^{(1)}_{\text{eff.}} + \mathcal{O}(q_i^2) \\ &= g_1 + \frac{\tilde{\Omega}(k_0)\lambda}{2m^*_{k_0}}\sum_{i=1}^{4}\frac{q_i}{\tilde{\Omega}(k_0)} + \mathcal{O}(q_i^2), \end{aligned} \tag{3.28}$$

where $g^{(0)}_{\text{eff.}}, g^{(1)}_{\text{eff.}}$ represent the contributions of zeroth and first order in q. This notation will be used in chapter 7 to give an estimate for the validity of eq. (3.28) for our experimental realization. The sum in eq. (3.28) runs over the incoming and outgoing momenta of the colliding atoms. The expansion coefficients are

$$g_1 = g_{\text{eff}}(k_0, k_0, k_0, k_0), \tag{3.29}$$

$$\lambda = \frac{4m^*_{k_0}}{\tilde{\Omega}(k_0)}\left(\frac{\tilde{\delta}(k_0)}{\tilde{\Omega}(k_0)}g_1 + g_{\downarrow\downarrow}\sin^4\theta(k_0) - g_{\uparrow\uparrow}\cos^4\theta(k_0)\right). \tag{3.30}$$

Substituting these expressions into eq. (3.24), the interaction Hamiltonian in position space becomes to leading order $\hat{H}_{\text{int}} = \int \mathrm{d}^3\mathbf{r}\hat{\mathcal{H}}_{\text{int}}$ with

$$\begin{aligned}\hat{\mathcal{H}}_{\text{int}} &= \frac{1}{2}\int \frac{\mathrm{d}^3\mathbf{q}_1}{(2\pi)^3}\frac{\mathrm{d}^3\mathbf{q}_2}{(2\pi)^3}\frac{\mathrm{d}^3\mathbf{q}_3}{(2\pi)^3}\frac{\mathrm{d}^3\mathbf{q}_4}{(2\pi)^3} g_{\text{eff}}\phi^\dagger(\mathbf{q}_3)\phi^\dagger(\mathbf{q}_4) \\ &\qquad \phi(\mathbf{q}_1)\phi(\mathbf{q}_2)\exp[i(\mathbf{q}_1+\mathbf{q}_2-\mathbf{q}_3-\mathbf{q}_4)\cdot\mathbf{r}] \\ &= \frac{1}{2}g_1\hat{\rho}(r)[\hat{\rho}(r)-1] + \frac{\lambda}{2im^*_{k_0}}\hat{\phi}^\dagger(r)[\hat{\phi}^\dagger(r)\partial_x\hat{\phi}(r) - (\partial_x\hat{\phi}^\dagger(r))\hat{\phi}(r)]\hat{\phi}(r)\end{aligned} \tag{3.31}$$

Apart from the usual non-linearity, scaling with g_1, the interaction Hamiltonian in eq. (3.31) features an additional term scaling with λ. In this term, we recognize the current operator of eq. (2.26) which reads in our dimensionless units: $\hat{J} = 1/(im^*_{k_0})(\hat{\phi}^\dagger\partial_x\hat{\phi} - (\partial_x\hat{\phi}^\dagger)\hat{\phi})$. Accordingly, the additional term precisely corresponds to the chiral interaction term $\lambda\hat{J}\rho/2$ of the encoded chiral BF theory (see eq. (2.26)). It explicitly breaks the Galilean invariance and provokes interactions which depend on momentum and hence are chiral. Thus, to first order in λ, eq. (3.31) is identical to the quantum version of the interaction term of the encoded chiral BF theory in eq. (2.26).

Full effective Hamiltonian

Combining eq. (3.23) and eq. (3.31), we obtain for the full Hamiltonian in position space:

$$\begin{aligned}\hat{H}_{\text{eff}} = &\int \mathrm{d}^3\mathbf{r}\hat{\phi}^\dagger(r)\left[\mathcal{E}_-(k_0) + W - \nabla_\perp^2 - \frac{(\partial_x - iA_0)^2}{m^*_{k_0}}\right]\hat{\phi}(r) \\ &+ \int \mathrm{d}^3\mathbf{r}\left[\frac{1}{2}g_1\hat{\rho}(r)(\hat{\rho}(r)-1) + \frac{\lambda}{2im^*_{k_0}}\hat{\phi}^\dagger(r)\left[\hat{\phi}^\dagger(r)\partial_x\hat{\phi}(r) - (\partial_x\hat{\phi}^\dagger(r))\hat{\phi}(r)\right]\hat{\phi}(r)\right].\end{aligned} \tag{3.32}$$

In the case of $\tilde{\delta} = 0$ (implying $P = 0$), the static vector potential A_0 does not depend on the quasi-momentum k_x and we can recast the Hamiltonian in terms of a covariant current-nonlinearity:

$$\begin{aligned}\hat{H}_{\text{eff.}} = \int \mathrm{d}^3\mathbf{r}\hat{\phi}^\dagger(r)\Big[&\mathcal{E}_-(k_0) + W - \nabla_\perp^2 - \frac{(\partial_x - iA_0)^2}{m^*_{k_0}} \\ &+ \frac{1}{2}\left(g_1 + \frac{2\lambda A_0}{m^*_{k_0}}\right)\hat{\rho} + \frac{\lambda}{2}\hat{J}(r)\Big]\hat{\phi}(r)\end{aligned} \tag{3.33}$$

with the current operator

$$\hat{J}(r) = \frac{1}{im^*_{k_0}}\left[\hat{\phi}^\dagger(r)(\partial_x - iA_0)\hat{\phi}(r) - ((\partial_x + iA_0)\hat{\phi}^\dagger(r))\hat{\phi}(r)\right]. \tag{3.34}$$

The Hamiltonian eq. (3.33) describes a system of bosonic particles around arbitrary momentum k_0 that are subjected to a synthetic vector potential A_0 and have an effective mass $m^*_{k_0}$ along the x-axis. These Raman-dressed bosons have standard density-density interactions of coupling strength $g_1 + 2\lambda A_0/m^*_{k_0}$, but also anomalous current-density interactions $\lambda \hat{J}\rho$ which are characteristic for the encoded version of the chiral BF theory.

The encoded Hamiltonian of the chiral BF theory (see eq. (2.27)) includes in addition a three-body interaction term. In the dimensionless units employed in this chapter, this energy term reads

$$E_{3B} = \int d^3\mathbf{r} \frac{\lambda^2}{4m^*_{k_0}} |\phi|^6. \tag{3.35}$$

Since it scales with λ^2, it is negligible in the regime of $\Omega_R \gg g_{\uparrow\uparrow}\rho, g_{\downarrow\downarrow}\rho$ and $g_{\downarrow\uparrow}\rho$ we are working in. Therefore, we can complete the square in the effective Hamiltonian of eq. (3.33) which allows us to rewrite the non-linear current term into the kinetic part:

$$\hat{H}_{\text{eff.}} = \int \mathrm{d}^3\mathbf{r} \hat{\phi}^\dagger(r) \Bigg[\mathcal{E}_-(k_0) + W - \nabla_\perp^2 - \frac{(\partial_x - i\hat{A})^2}{m^*_{k_0}} + \frac{1}{2}\left(g_1 + \frac{2\lambda A_0}{m^*_{k_0}} \right) \hat{\rho} \Bigg] \hat{\phi}(r) + \mathcal{O}(\lambda^2) \tag{3.36}$$

In this case, the Hamiltonian describes a bosonic field minimally coupled to a vector potential which has a single particle and a density-dependent contribution: $\hat{A} = A_0 - \frac{\lambda}{2}\hat{\phi}^\dagger(r)\hat{\phi}(r)$. Note that in the assumed case of $\tilde{\delta} = 0$, the first part of the vector potential is constant as $A_0 = -m^*_{k_0} k_0$ and can be removed by a standard gauge transformation. Moreover, the evaluation of the coupling strength g_1 simply yields $g_1 = (g_{\uparrow\uparrow} + g_{\downarrow\downarrow} + 2g_{\downarrow\uparrow})/4$ which is equivalent to the coupling strength g of the non-linearity in eq. (3.15) out of Ref. [52]. The factor λ also simplifies to $\lambda = m^*_{k_0}(g_{\downarrow\downarrow} - g_{\uparrow\uparrow})/\tilde{\Omega}_R$, so the magnitude of the density-dependent vector potential scales linearly with the unbalance in the intrastate interaction strengths. The result in eq. (3.36) connects our momentum-space derivation of the effective Hamiltonian to the real-space derivation of Ref. [52] yielding eq. (3.15), and shows that the latter is the classical limit of the former.

Apart from constant energy contributions, the effective Hamiltonian of eq. (3.36) for $\tilde{\delta} = 0$ is identical to the encoded Hamiltonian of the chiral BF theory in eq. (2.26), supplemented with an additional density non-linearity of $2\lambda A_0 |\hat{\phi}(r)|^2/m^*_{k_0}$ and where the mass of the atoms is replaced by $m^*_{k_0}$. Therefore, a two-component Raman-dressed BEC with unbalanced interactions (implying $\lambda \neq 0$) described by

the effective Hamiltonian eq.(3.36), is a well-suited platform to experimentally realize the chiral BF theory in its encoded form. The system described by the effective Hamiltonian has the properties discussed in section 2.4 for the chiral BF theory. In particular, chiral soliton solutions exist and the expansion dynamics is modified, effects we indeed observe experimentally (see chapter 7).

My group also performed numerical simulations to validate the Hamiltonian of eq. (3.36) as effective description for our experimental parameters. To this end, the effective single-component Hamiltonian was compared with the complete two-component description with respect to density profiles and experimental observables. Details can be found in our publication "Encoding a one-dimensional topological field theory in a Raman-coupled Bose-Einstein condensate". The simulations were performed by my colleague Craig Chisholm, and will thus be included in his PhD thesis.

3.4 Conclusion

In this chapter we discussed to which extent the effective Hamiltonian of a BEC where two internal states with unequal interactions are coupled by Raman light maps to the encoded Hamiltonian of the chiral BF theory presented in chapter 2. While the mapping was originally proposed by the Öhberg group in Ref. [52], where the effective Hamiltonian was obtained with perturbation theory in the adiabatic approximation in position space, we presented in this chapter an alternative approach based on a momentum-space picture. Building upon the work of Ref. [107], we derived the effective Hamiltonian in momentum space and in the dressed state basis from a microscopic view. Our description holds for arbitrary momenta and interaction strengths in the Raman-coupled states. It allowed us to derive the effective Hamiltonian of the system restricted to the lowest dressed band outside the adiabatic approximation which demonstrates that its implementation is also possible for experimentally less demanding values of the Raman coupling strength. We also included finite values of the two-photon detuning, and found that the effective Hamiltonian maps to the encoded chiral BF theory as long as $\tilde{\delta} \approx 0$. Moreover, the mapping remains valid on the quantum level, so the chiral BF theory beyond the mean-field approximation could be explored.

4 Experimental platform and interaction control using coherent coupling

This chapter gives an overview over the experimental platform on which we experimentally realize the encoded chiral BF Hamiltonian. We start with a description of our apparatus capable of producing Bose-Einstein condensates of ^{41}K or ^{39}K. Afterwards we focus on methods to control the interactions in the isotope ^{39}K. In particular, we investigate coherent coupling via radio-frequency as novel method to tune the effective interactions of the system in a broad, flexible and fast manner.

After chapter 1,2 and 3, we have set the theoretical ground for a realistic experimental investigation of the chiral BF theory. In the following, we turn to the experimental part of our work. In this chapter, we start by introducing the experimental setup. Thereafter, we turn to the interaction control in ^{39}K by coherent coupling, which is one of the main requirements for realizing the encoded chiral BF theory (see chapter 3). We study the effective interactions present in a coherently-coupled ^{39}K BEC with unequal interaction strengths which was derived in section 3.3.1 in a general form. In this chapter, we realize the coherent coupling not with Raman light as in the rest of the thesis, but instead *via* radiofrequency. Hence, the interactions are not chiral as the internal state is not locked to the momentum. This allows us to investigate the concept of effective interactions in a simple setting, before combining the interaction control and Raman coupling in chapter 7.

4.1 Experimental apparatus

All our experiments are performed with a Bose-Einstein condensate of potassium ^{41}K or ^{39}K. Our experimental apparatus as well as the cooling sequence and techniques utilized to achieve condensation, are described in detail in the PhD thesis of Dr. Cesar Cabrera[108] and Dr. Julio Sanz[109], who played the most significant role in building up the apparatus. I started my research on the potassium experiment in January 2018. Although I started with an apparatus readily built, several improvements and maintenance tasks were necessary. In particular, in the first half of 2018 my PhD colleague Dr. Julio Sanz and I replaced and implemented a new *in situ* imaging setup and added a second high resolution objective for addressing potentials to the experiment. This steps required major rebuilding, e.g. removing most of the MOT optics and a re-optimizing of the established cooling sequence.

In this section, we give a short overview over the different isotopes of potassium, the cooling sequence and the parts of our apparatus relevant for the measurements described in this thesis. In addition, we summarize important parameter of the *in situ* imaging and our procedure to build in two high resolution objectives.

4.1.1 The potassium atom

Potassium is an alkali atom, it has a single electron in its valence band. This makes it relatively easy to cool down potassium to quantum degeneracy in comparison to dipolar or alkaline-earth metals. Potassium has three stable isotopes. The most common is the bosonic ^{39}K with 93.3 % abundance, followed by the bosonic ^{41}K with 6.7 % and the fermionic ^{40}K with 0.012 % abundance. All three isotopes of potassium have been cooled down to quantum degeneracy for the first time

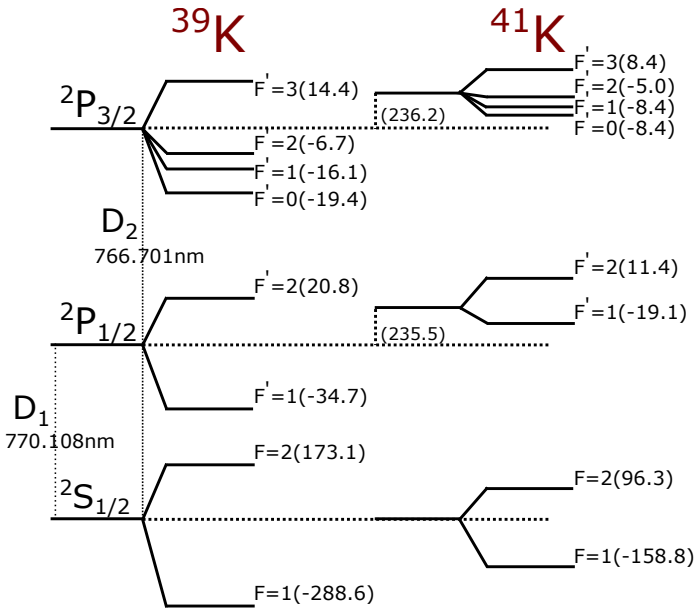

Figure 4.1: Fine- and hyperfine structure of the two potassium isotopes ^{39}K and ^{41}K. The hyperfine energy shifts in parenthesis are given with respect to the corresponding energy level of the fine structure. The spacing of the levels are not to scale and values are taken from Ref. [113].

between 2001 and 2007[110–112]. Our experimental apparatus is currently capable of condensing both bosonic isotopes and we performed experiments with ^{39}K as well as with ^{41}K.

The atomic energy levels arising from the fine structure and hyperfine structure splitting are depicted in Fig. 4.1 for the two potassium isotopes ^{41}K and ^{39}K. The level scheme is shown in terms of the quantum number F, which describes coupling of the electronic angular momentum and spin and the nuclear spin. We use the electronic transitions at $\lambda = 766.701$ nm (D2 line) and at $\lambda = 770.100$ nm (D1 line) to cool down and image the atoms. Our experimental sequence is described in the next paragraph.

4.1.2 Route to Bose-Einstein condensation

In order to produce a ^{39}K or ^{41}K Bose-Einstein condensate we employ a standard cooling sequence of Doppler cooling, sub-Doppler cooling, rf evaporation cooling in a magnetic trap and evaporative cooling in an optical dipole trap. A peculiarity of our apparatus is that we cool down ^{39}K and ^{41}K simultaneously. In fact, the sympathetic cooling steps for ^{39}K crucially rely on the presence of ^{41}K. Because the background interaction strength of ^{39}K is negative, we employ the large repulsive collisional properties between ^{39}K and ^{41}K to achieve thermalization. The cooling

sequence for both isotopes is in principle the same and consists out of the following main steps:

- We start the sequence in a vacuum chamber with high vapour pressures of ^{39}K and ^{41}K. Out of these, we sequentially produce cold atomic beams with a 2D Magneto-optical trap (2D MOT) on the D2-transition.

- We push the atoms optically to a distinct ultra-high vacuum chamber where ^{39}K and ^{41}K are sequentially captured by a 3D Magneto-optical trap (3D MOT) on the D2-transition. If we want to condense ^{41}K, we remove the loading time of the ^{39}K MOT. Afterwards the density of the cloud is increased in a compressed hybrid D1-D2 MOT.

- We perform sub-Doppler cooling of ^{39}K and ^{41}K with a grey optical molasses on the D1-transition.

- We optically pump atoms into state $|F = 2, m_F = 2\rangle$ which is a low-field seeking state. The atoms get captured in a magnetic quadrupole trap, where we use radio-frequency (rf) evaporation on the hyperfine transition to cool ^{41}K. The isotope ^{39}K is sympathetically cooled due to the positive and large background interaction strength between ^{39}K and ^{41}K. Typical atom numbers at this stage are 4×10^7 and 2.5×10^7 for ^{41}K and ^{39}K at a temperature of ~ 30 μK.

- We apply magnetic field gradients to shift the centre of the quadrupole trap to the geometric centre of the vacuum cell. This step is needed as our imaging setup with high NA objective is designed for imaging objects in the geometric centre.

- We load the atoms to a hybrid trap formed by a reduced quadrupole trap and an additional optical dipole trap beam. Atoms are evaporatively cooled down and we remain with an atom number of $\sim 1 \times 10^6$ atoms in both isotopes with a temperature of ~ 1 μK.

- We transfer the atoms to a purely optical dipole trap formed by two crossed laser beams. If we want to condense ^{39}K, we blow away ^{41}K with an optical pulse on resonance with the ^{41}K D2 transition. Afterwards, we prepare the atoms in the lowest state of the $F = 1$ manifold via radio-frequency sweeps.

- We increase the magnetic field strength to a value close to a Feshbach resonance of ^{39}K (around 33 G or 402 G) and achieve Bose-Einstein condensation by forced evaporation. We have atom numbers up to 120×10^3 and 140×10^3 for ^{41}K and ^{39}K, respectively.

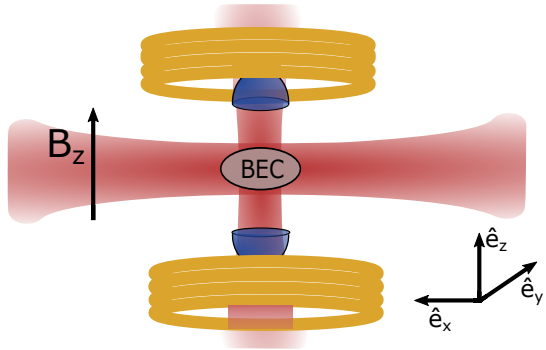

Figure 4.2: Sketch of the experimental setup. The atoms are trapped in a crossed optical dipole trap, formed by laser beams along the $\hat{e}_x$- and $\hat{e}_z$-axis. A homogenous bias field in $\hat{e}_z$-direction is applied through a pair of coils in Helmholtz configuration. Two high NA objectives are installed on the top and bottom of the chamber for imaging and projecting potentials on the atoms.

4.1.3 Details of operation

Optical dipole traps

The starting point of all our experiments is a Bose-Einstein condensate in a optical dipole trap formed by two laser beams propagating along the $\hat{e}_x$- and $(\hat{e}_x+\hat{e}_y)/\sqrt{2}$-axis. Unless explicitly stated otherwise, we transfer the atom into a optical trap formed by the trapping laser beam along $\hat{e}_x$ and an additional laser beam along $\hat{e}_z$ direction. The geometry of the setup is sketched in Fig. 4.2. In most measurements we investigate the dynamics of system only along the direction of $\hat{e}_x$. In this case we initialize the experiment by switching off the axial confinement and allow the cloud to expand in the remaining waveguide potential along the $\hat{e}_x$-axis. The remaining axial trap frequency caused by the residual curvature of the magnetic field is in the order of $\omega_x/2\pi = 4$ Hz at 400 G .

Magnetic fields

All magnetic fields in our apparatus are produced by electric currents. The main fields are produced by a couple of coils aligned along $\hat{e}_z$ and placed at the top and bottom of the vacuum chamber. The coils have a distance of $\sim$ 27 mm to the atoms and have a Bitter design[114], which allows an efficient water cooling. The configuration of the coils can be switched between anti-Helmholtz and Helmholtz configuration by an H-bridge circuit. Thus the coils are used to produce the quadrupole field for the magnetic trap stage as well as the homogenous field oriented along $\hat{e}_z$ direction during condensation and measurement stage. The current is supplied by a power supply with a range of $(0-400)$ A [1]. In this thesis

[1] Delta Elektronika SM 15-400

we employ magnetic fields strengths between $(50 - 400)$ G, which corresponds to currents between $\sim (21 - 170)$ A. The magnetic field strength has a stability of $\sim \pm 2$ mG at 50 G and $\sim \pm 15$ mG at 400 G, measured with rf spectroscopy and Ramsey interferometry[115].

In addition to the main coils we have a set of four coils in cloverleaf configuration both at the bottom and top of the vacuum chamber, and a set of round coils around each window of the chamber. All these coils are winded with copper-wire and are not water cooled. These coils allow us to compensate curvatures or gradients produced by the main coils. Moreover, they are essential for optimizing the transfer of atoms from the hybrid to the optical dipole trap which has a fixed position to ensure that the atoms are in the focus of our imaging objectives. In addition, we use the coils to realize a strong magnetic field gradient along $\hat{e}_z$ in some imaging sequences. The earth magnetic field and ambient stray magnetic fields are compensated with a set of three coils located outside the optical table.

Internal state control

The internal state of the atoms in the BEC can be controlled and manipulated by means of radio-frequency fields. Depending on the application, i.e. rf-sweeps or rf-pulses, we use either a FPGA based[2] or analogue[3] frequency generator, respectively. The signal is amplified with a high power amplifier[4] and forwarded to an antenna. The impedance between amplifier and antenna is matched to maximize the strength of the RF in the vacuum chamber. We also use optical Raman coupling to control the internal state (see chapter 5).

Imaging

In order to extract information from the atomic cloud we either extract its momentum or spatial distribution. The momentum distribution of the cloud is reconstructed *via* time of flight (ToF) imaging. In ToF imaging, the optical traps are turned off abruptly and the cloud ballistically expands for time duration t_{ToF}, so the momentum distribution is mapped into position space. We have a time of flight duration of ~ 21 ms after which the cloud's size is in the order of hundreds of micrometres. Therefore it is sufficient to use standard absorption imaging in the horizontal plane along the $\hat{e}_x + \hat{e}_y$ direction. We use light on the D2-transition, which after passing through the atomic cloud is shed on a CCD camera [5]. The geometry of our vacuum chamber implies a long working distance of > 150 mm and therefore a relatively low numerical aperture (NA) of < 0.25 and resolution

[2] Signadyne, SD AOU-H3444-PXIe-1G
[3] Rhode and Schwarz, SMC100A
[4] ZHL-100W-GAN+, Mini-Circuits
[5] Chameleon, USB CMLN-13S2M-CS

power. In the absorption imaging sequence, we apply a magnetic field gradient along the $\hat{e}_z$ direction during time of flight expansion, which is referred to as Stern Gerlach pulse. This pulse spatially separates different magnetic spin states along the vertical axis. Hence, we are able to measure not only the total atom number, but also the spin resolved populations.

To reconstruct the spatial distribution of the atomic density, we make instead use of an *in situ* imaging with a high numerical aperture objective, oriented along the vertical $\hat{e}_z$-direction and based on the polarization phase contrast effect. This imaging setup is described in more detail in the next section.

4.1.4 High NA objectives for imaging and addressing

The design, implementation and characterization of the *in situ* imaging objectives are thoroughly described in Ref.[109]. Here below, we summarize the main aspects of the imaging setup, its alignment and performance.

Imaging setup

The imaging setup allows to image the cloud *in situ* along the $\hat{e}_z$-direction. It consists out of a homebuilt high NA objective, a camera and additional lenses to match the magnification to the pixel size of the camera. An illustration of the setup is shown in Fig. 4.3. The imaging laser light with $\lambda = 766.7$ nm illuminates the sample from the bottom view-port of the vacuum chamber and is collected by the high NA objective placed at the top of the chamber. The top objective in combination with three additional lenses results in a magnification of the light by 33, and finally the light is shined on a camera. The NA of our setup is mainly limited by the distance between the view-ports of our vacuum cell, the clear aperture and thickness of the windows. The objective is made out of a meniscus [6] and an asphere [7] with an effective focal length of $f = 48.6$ mm. The objective is designed for light with wavelength $\lambda_L = 766.7$ nm. The numerical aperture is 0.43 and the expected resolution 1.1 µm. The depth of focus is calculated to be 10 µm, the field of view 330 µm. As imaging device we use a Electron Multiplying Charged-Coupled Device camera (EMCCD) [8] with a pixel size of 16 µm. The large imaging magnification ensures that the resolution is not limited by this (large) size of the pixels.

[6] custom meniscus, Ross Optics Industries, N-BK-7
[7] Edmund Optics,L-BAL35
[8] Andor, Ixon DU 897U-CS0-EXF

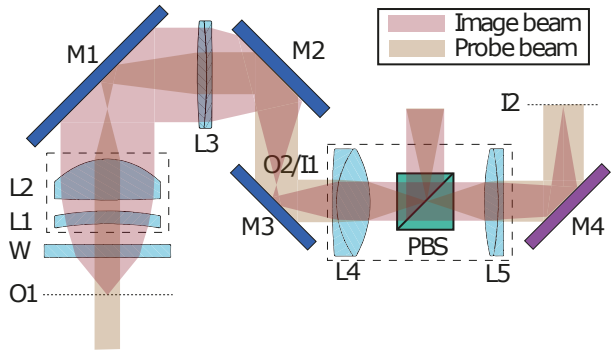

Figure 4.3: Schematics of the *in situ* imaging setup along $\hat{e}_z$. (O1) denotes the object plane, (W) the view-port window. The high NA objective consists out of meniscus (L1) and asphere (L2). The objective is followed by an achromat with $f = 500$ mm (L3), which together form a telescope with magnification of ~ 10.3. The second telescope with achromatic lenses with $f = 80$ mm (L4) and $f = 250$ mm (L5) results in a total magnification of ~ 33. The mirrors (M1,M2,M3) are dielectric mirrors with NIR broad-band coating. (M4) is a long-pass dichroic mirror to separate the imaging light and infrared light from our dipole trap. The polarizing beam splitter (PBS) maps changes in the polarization of the probe light into intensity differences in the camera. Picture is taken from J. Sanz out of Ref. [109].

Addressing setup

Additionally to the new high NA objective for imaging, we decided to add a microscope to the apparatus, which is capable of projecting arbitrary potentials onto the atomic plane. The microscope is placed on the bottom of the vacuum chamber and its design is identical to the imaging objective. The addressing setup is used to create a barrier potential for the atoms in chapter 7.

Alignment and characterization

The alignment of the objective is challenging and requires many steps. We removed the previous setup completely and started by characterizing the aberrations introduced by the windows (viewports) of our vacuum chamber. We investigated the effect of the view-ports by building an interferometer, where a large Gaussian beam passing twice through the two viewports interferes with a reference arm. The wavefront of the beam passing through the vacuum windows gets deformed and the interference signal shows an intensity distribution which is elliptical rather than circular along the axial direction, indicating that the viewports introduce astigmatism. We also performed tests with a shearing plate interferometer[9], where the reflections from the front and back of a wedged plate are interfered. If the input beam is perfectly collimated, the interference fringes are parallel to the propagation

[9]Shearing interferometer, Thorlabs, SI500

direction of the laser beam. If the beam is decollimated, the fringes are tilted. Our tests showed that an initially collimated beam gets slightly defocused after the vacuum chamber. The interference fringes are also different in orthogonal directions, so the vacuum windows introduce some astigmatism. Moreover, we observed a curvature of the fringes, indicating higher-order aberrations.

Afterwards, we installed the high NA objectives for imaging and addressing in the apparatus. We based our alignment procedure on reference beams which are geometrically centred and perpendicular to the viewports. Because the top and the bottom window have a tilt of $\sim 0.2\,^{\circ}$, we needed one reference beam for each window. To bring the two objectives into focus, we used the following procedure: at first we kept the top objective fixed at its rough focus position, namely at the planned distance form the vacuum window, and found the focus position of the bottom objective by collimating an initially collimated beam after passing through the two objectives with the shearing plate. Afterwards we found the final focus position of the top objective by imaging a test object. As test objects we used an USAF 1951 target[10] and an 1 µm pinhole[11]. In both cases we produced the respective image with the addressing objective in the plane of the atoms and imaged it with the imaging objective from top. The focused image exhibited strong astigmatism introduced by the view-ports as previously investigated. We decided to actively correct this astigmatism by compensating with a tilted glass plate placed between the achromat L3 and mirror M3 (see Fig. 4.3) which introduces astigmatism in the opposite direction.

In the final performance of the complete setup - addressing and imaging objective - we were able to discern element 6 of group 5 from the USAF target, which are separated by 1.09 µm in the object plane. Moreover, we could recover the point spread function of the 1 µm pinhole and measured radii of 1.1 µm and 1.5 µm in the EMCCD camera.

4.2 Interaction control in ^{39}K

As outlined in section 3.3, interactions in the systems play a key role in the realization of the encoded chiral BF theory. Therefore we need a good control over the intra- and interstate interactions of the internal states.

In section 3.3 we have described interactions *via* the coupling strength g. In the experimental parts we instead express the coupling strength in its commonly parametrized form of the s-wave scattering length a with $g = 4\pi\hbar^2 a/m$. The two isotopes ^{41}K and ^{39}K vastly differ in their scattering length a. Whereas ^{41}K has a

[10] R1DS1P, Thorlabs
[11] Mounted precision pinhole, P1H, Thorlabs

background scattering length of $\sim 60\ a_0$, ^{39}K possesses $\sim -33\ a_0$. Here a_0 is the Bohr radius. The background scattering lengths have important implications for the BEC production (see section 4.1.2). Moreover, in ^{41}K, the scattering lengths of the internal states are approximately constant and of same value. By contrast, in ^{39}K we can adjust the interaction strengths in the internal states of the BEC to different values. This allows us to explore different physics with the two isotopes.

In this section, we explain how we can tune the scattering length a in the ^{39}K condensate. We can either do so by means of magnetic Feshbach resonances or *via* coherent coupling. The following subsection explain in more detail these two methods.

4.2.1 Magnetic Feshbach resonances

In the isotope ^{39}K, the intra- and interstate scattering lengths can be widely tuned by means of magnetic Feshbach resonances[116]. In particular, we consider the scattering lengths of the magnetic sub-levels $m_F = \{1, 0, -1\}$ of the $F = 1$ hyperfine manifold. For our experiments, we are interested in the regions where for a pair of states both intrastate scattering lengths are positive and we can tune the strength of at least one in a wider range. This ensures we can prepare a stable condensate in both states and we can realize different interaction strengths in the two states - a crucial feature of all or experiments with ^{39}K. Up to 400 G, there are two windows of magnetic field strengths where these requirements are fulfilled for a pair of states. Fig. 4.4 displays the intra- and interstate scattering lengths for the relevant states in these magnetic field ranges. Namely, around $B \sim 57$ G and $B \sim 400$ G, which are in the vicinity of a Feshbach resonance of the $|F = 1, m_F = 0\rangle$ state (left panel in Fig 4.4) and $|F = 1, m_F = 1\rangle$ (right panel of Fig. 4.4), respectively. For the study of coherent coupling *via* radio-frequency as interaction control (see next paragraph 4.2.2), we work in the first magnetic field range of $\sim (56 - 58)$ G. The experiments with Raman coupling (see chapters 6,7) we instead perform in the magnetic field range between $B = (374 - 397)$ G, which offers additional advantages (see section 5.1.2)

The scattering lengths shown in Fig. 4.4 were calculated by A. Simoni with the ^{39}K model interaction potentials of Ref. [117]. The systematic uncertainty in a is dominated by the uncertainty of the position B_0 of the Feshbach resonances. For the high field range, we can compare the results of A. Simoni to calculations with different interaction potentials performed by the group of Prof. Kokkelmans, using the model potentials of Ref. [118]. The latter have been built based on the most recent calibrations of Feshbach resonances of the different potassium isotopes, including among others ^{39}K-^{41}K resonances observed by our group[119]. From the different results we estimate a systematic uncertainty in the theory pre-

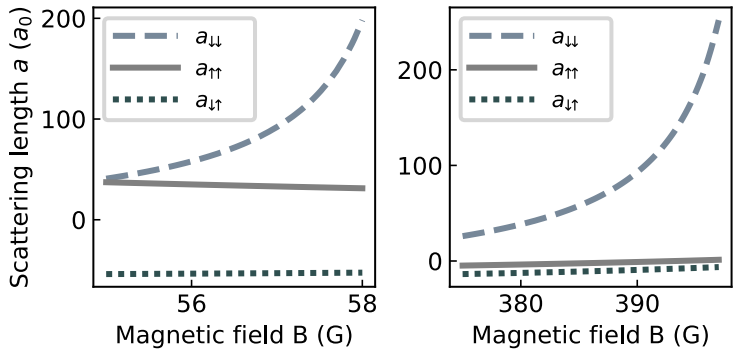

Figure 4.4: Magnetic Feshbach resonances in ^{39}K. **Left:** Intra- and interstate scattering lengths of $|\downarrow\rangle = |F = 1, m_F = 0\rangle$ and $|\uparrow\rangle = |F = 1, m_F = -1\rangle$ close to 57 G as function of applied magnetic field B. **Right:** Intra- and interstate scattering lengths of $|\downarrow\rangle = |F = 1, m_F = 1\rangle$ and $|\uparrow\rangle = |F = 1, m_F = 0\rangle$ around 397 G.

diction of approx. 200 mG for the position B_0 of the Feshbach resonance around 402 G. Using spectroscopy, we could in principle locate the Feshbach resonance experimentally much more precise[119]. However, the uncertainty in the theoretical prediction translates in a maximal uncertainty of $\sim 9\ a_0$ in the intra-state scattering length of state $|\downarrow\rangle$ at $B = 397$ G. This precision is already sufficient to interpret our experiments and does not affect the conclusions drawn in our work. Therefore we did not attempt to calibrate the scattering lengths more accurate.

4.2.2 Coherent coupling

In this section, we investigate an alternative method for controlling interactions in Bose-Einstein condensates which is fast, flexible and simple to implement experimentally. In our scheme, two internal states $|\downarrow\rangle, |\uparrow\rangle$ with different scattering lengths are coherently-coupled, which modifies the scattering properties of the corresponding dressed states, as we have investigated in section 3.3. Here we use radio-frequency fields for the coherent coupling, so in contrast to the more general equations derived in chapter 3 for Raman coupling, no momentum transfer is involved. Hence, the study of rf-coupling as interaction control can be seen as preparatory step in which we get familiar with the concept of effective scattering properties but do not add additional complexity caused by the momentum transfer.

Until now, the modified scattering length of rf-dressed atoms could only be observed indirectly through the change of miscibility in binary BEC mixtures[104,105,120], in a configuration where interactions were modified in a narrow range. In the following, we characterize the elastic and inelastic scattering properties in a rf-dressed ^{39}K BEC, which we can flexibly control by adjusting the parameters of the coupling field. We also demonstrate the interaction control in the attractive regime, where

we observe the stabilization of bright solitons formed by dressed-state atoms. Furthermore, we exploit the high temporal bandwidth of this technique to quench the interactions from repulsive to attractive values, and observe how the resulting modulational instability develops into a bright soliton train.

The study of rf-dressing as interaction control gave rise to the publication "Interaction control and bright solitons in coherently-coupled Bose-Einstein condensates"[106] in which I am second author and which was published in Physical Review Letters. It was performed in close collaboration with Dr. Julio Sanz, first author of this publication, Craig Chisholm and Dr. Cesar Cabrera. The work is presented in all its detail in the PhD thesis of Dr. Sanz[109]. Therefore, here I will report on the main results of the publication without major modifications.

This chapter describes experimental results without Raman coupling. Accordingly, we will change from the dimensionless units of the Raman recoil energy employed in the last theoretical chapters to SI units.

Theoretical base

We perform all experiments in the strong coupling limit, where the Rabi frequency Ω of the radio-frequency field dominates over all other energy scales of the system. We describe the system in the previously introduced dressed state picture (see section 3.2.1). For the coupling with radio-frequency, these formulas simplify as no momentum transfer is involved. Hence, $\tilde{\delta} = \delta_0$ and $\tilde{\Omega} = \tilde{\Omega}(0) = \sqrt{\Omega^2 + \delta_0^2}$. Therefore the dressed states $|-\rangle = \sin\theta\,|\downarrow\rangle - \cos\theta\,|\uparrow\rangle$ and $|+\rangle = \cos\theta\,|\downarrow\rangle + \sin\theta\,|\uparrow\rangle$, with $\cos^2\theta = (1+P)/2$ and $P = \delta_0/\tilde{\Omega}(0)$ that do not depend on the momentum. The energies of the two dressed states is shown as function of the detuning δ_0 in the upper panel of Fig. 4.5. The energy gap in the avoided crossing is $\hbar\Omega$. To describe the interactions between dressed states, we rewrite the interaction part of the Hamiltonian in the dressed-state basis[103]. The resulting collisional couplings account for elastic or inelastic scattering, so processes which either preserve the two-particle dressed state of the colliding atoms, or modify it. For a condensate in state $|-\rangle$, inelastic collisions in the strong coupling limit are energetically forbidden and only elastic processes remain. They can be described by the effective scattering length eq. (3.27) derived in section 3.3 when considering vanishing momentum transfer. This effective scattering length a_{--} depends on the scattering properties of the bare states and on the composition of the system. Therefore it can be tuned with the coupling field parameters. In contrast, for a BEC in state $|+\rangle$ both elastic and inelastic processes are relevant.

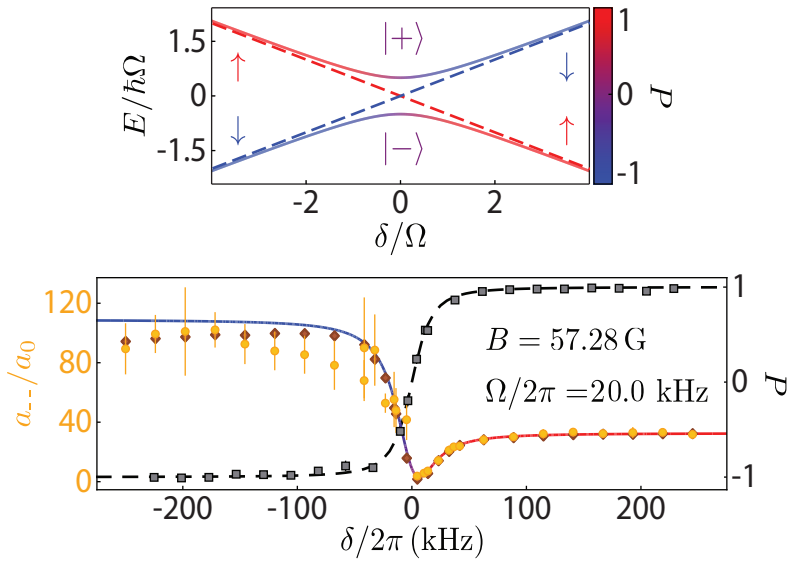

Figure 4.5: Elastic scattering properties of the lower dressed state. **Top:** energy E of states $|-\rangle$ and $|+\rangle$ as function of the detuning δ, normalized to the Rabi frequency Ω. $\uparrow$ and $\downarrow$ are the bare atomic states. The colorscale indicates the state composition in terms of $P = \delta/\tilde{\Omega}$. **Bottom:** experimental value of a_{--} obtained by scaling σ_x^5/N (orange circles, left axis) and the polarization P (gray squares, right axis) versus δ. The lines show the theory predictions, the brown diamonds represent the values obtained from an numerical simulation of the expansion. The colourscale of the a_{--} curve indicates the value of P. The error bars are obtained from the standard deviation of 5 independent measurements. Figure is taken from Ref. [106].

Methods

For the study presented in this section, we employ a ^{39}K BEC at magnetic fields of $B \sim (56 - 57)$ G. We exploit two magnetic sub-levels of the $F = 1$ hyperfine manifold $|\uparrow\rangle = |F = 1, m_F = -1\rangle$ and $|\downarrow\rangle = |F = 1, m_F = 0\rangle$, for which the intra-state scattering lengths are repulsive ($a_{\uparrow\uparrow}, a_{\downarrow\downarrow} > 0$), and the interstate scattering length is attractive ($a_{\uparrow\downarrow} < 0$) (see left panel of Fig. 4.4).

We coherently couple the two states with an rf-field, with $\Omega/2\pi > 8$ kHz. We prepare single dressed states through Landau-Zener sweeps, starting from state $|\uparrow\rangle$ (unless explicitly stated otherwise) and ramping the detuning δ to its final value. The detuning uncertainty is ± 1.5 kHz, limited by short-term magnetic field fluctuations in the order of ± 2 mG. This limits the minimal Rabi frequencies accessible in our setup, which are calibrated independently through Rabi oscillations. The ramp rates are limited from below by such fluctuations, and from above by diabatic transitions to the higher dressed state when the Landau-Zener adiabaticity

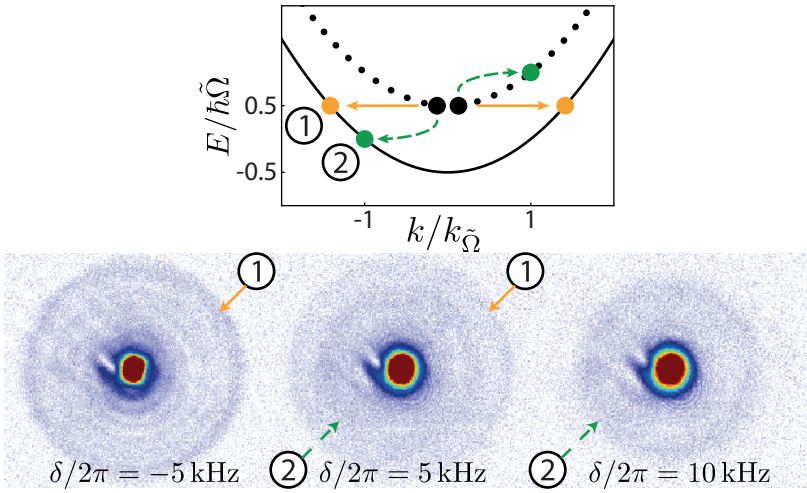

Figure 4.6: Inelastic decay of the higher dressed state. **Top:** sketch of possible dressed state changing collisions ①: $|{+}{+}\rangle \to |{-}{-}\rangle$ (orange, solid arrows) and ②: $|{+}{+}\rangle \to (|{+}{-}\rangle + |{-}{+}\rangle)/\sqrt{2}$ (green, dashed arrows). Energy E and momentum k are normalized by $\tilde{\Omega} = \sqrt{\Omega^2 + \delta^2}$ and $k_{\tilde{\Omega}} = \sqrt{m\tilde{\Omega}/\hbar}$. **Bottom:** momentum distribution of the collision products. Images are the average of 10 independent measurements. The likelihood of processes ① and ② depends on δ. Figure is taken from Ref. [106].

criterion $\dot{\delta} < \Omega^2$ is not fulfilled.

One peculiarity of the chosen states $|{\downarrow}\rangle$ and $|{\uparrow}\rangle$ is the vast difference in their three-body recombination rates. In our employed magnetic field range, the three-body loss rate measured for a thermal gas in state $|{\downarrow}\rangle$, $K_{\downarrow\downarrow\downarrow} \simeq 3\times10^{-27}$ cm^6/s, is almost 40 times larger than the three other relevant rates $K_{\uparrow\uparrow\downarrow}$, $K_{\downarrow\downarrow\uparrow}$, and $K_{\uparrow\uparrow\uparrow}$, which are compatible with the background value $K_{\uparrow\uparrow\uparrow} \simeq 7.8 \times 10^{-29}$ cm^6/s[86]. Therefore, the lifetime of the rf-dressed BEC is strongly reduced when the fraction of atoms in state $|{\downarrow}\rangle$ increases, i.e. for polarizations $P \to -1$, which corresponds to large and negative values of the detuning δ. The minimal value of the rf-dressed BEC lifetime is set by that of a single-component condensate in state $|{\downarrow}\rangle$, which for our typical densities and optical trap depths corresponds to tens of milliseconds. However, since the atom loss rate due to three-body recombination is much smaller than the Rabi frequency of the rf-coupling field $\Omega/2\pi > 8$ kHz, the latter is always able to keep P at its expected value. Thus, the net effect of the state-dependent three-body recombination rate is to induce losses of atoms with an effective rate K_3^{eff} that depends on the value of δ, increases as P approaches -1, and does not change the state composition of the system nor its effective scattering length.

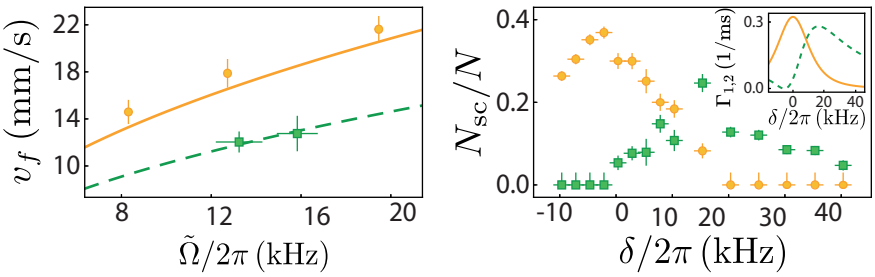

Figure 4.7: Quantization of the inelastic decay of the higher dressed state. **Left:** velocity of the scattered atoms v_f vs. $\tilde{\Omega}$. **Right:** fraction of scattered atoms N_{sc}/N as function of δ. Inset: Inelastic scattering rate $\Gamma_{1,2}$ versus δ for $n = 1.3 \times 10^{14}$ atoms/cm^3. In both panels, orange circles (green squares) correspond to process ① (②). The lines represent the non-interacting theory predictions. The error bars stem from the fit error (vertical) and uncertainty of δ and Ω (horizontal). Figure is taken from Ref. [106].

Elastic scattering in the lower dressed state

In a first series of experiments we focus on the elastic scattering properties of the lower dressed state $|-\rangle$. They are characterized by the effective scattering length eq. (3.27) with $k_R = 0$ which gives $a_{--} = a_{\uparrow\uparrow}\cos^4\theta + a_{\downarrow\downarrow}\sin^4\theta + \frac{1}{2}a_{\uparrow\downarrow}\sin^2 2\theta$. Thus the scattering properties depend on the state composition of the system *via* Ω and δ. We experimentally probe the dependency on δ by performing expansion measurements in an optical waveguide along $\hat{e}_x$ (see section 4.1.3 for our trap geometry).

To this end, we prepare a BEC in state $|-\rangle$ with $\Omega/2\pi = 20.0(6)$ kHz and variable detuning δ using a ramp rate of 0.83 kHz/ms. The magnetic field is set to $B = 57.280(2)$ G, for which the scattering lengths are $a_{\uparrow\uparrow}/a_0 = 32.5$, $a_{\downarrow\downarrow}/a_0 = 109$, $a_{\uparrow\downarrow}/a_0 = -52.9$, and we always have $a_{--} > 0$. After holding the gas for 5 ms at the final detuning, we abruptly switch off the axial confinement and allow it to expand for 21 ms along a single-beam optical dipole trap with radial trap frequency $\omega_r/2\pi = 133(1)$ Hz and axial frequency $\omega_x/2\pi \sim 1$ Hz. We finally image the gas *in situ* (see section 4.1.4 and Ref. [86,121]) and fit the images with a 2D Thomas-Fermi profile to extract the axial size σ_x and atom number N. We exploit the axial size of the cloud σ_x after the fixed expansion time to infer the scattering length a_{--}. In the Thomas-Fermi regime the two are related by $a_{--} \propto \sigma_x^5/N$[122]. Although this approximation is not strictly valid for all of our experimental parameters, we have verified by solving numerically the time-dependent Gross-Pitaevskii equation (GPE) that estimating a_{--} through this scaling law results in errors below our experimental uncertainties.

The lower panel of Figure 4.5 shows our determination of a_{--} for various values of

detuning (circles), which corresponds to different values of the polarization parameter P (squares). We determine the latter by Stern-Gerlach separation of the bare states during time-of-flight expansion, from which we extract their populations. In order to correct for systematic errors in the measurement and compare the results to the scattering length a_{--}, we have scaled σ_x^5/N to yield $a_{\uparrow\uparrow}$ at large positive δ. For large positive (negative) values of δ the effective scattering length should approach $a_{\uparrow\uparrow}$ ($a_{\downarrow\downarrow}$), and we expect a minimum at $\delta/2\pi = 6.5$ kHz ($P = 0.31$) due to the attractive character of the interstate interactions $a_{\uparrow\downarrow} < 0$. This is in good agreement with the experimental measurements. The data at large negative δ are in fair agreement with the limit $a_{\downarrow\downarrow}$. In this regime, also the scaling law yields the largest discrepancies with the GPE simulations (diamonds). For $\delta \ll 0$, the data suffers from larger uncertainties due to residual breathing excitations induced by the detuning ramp, which is associated to large changes of a_{--}, and the larger three-body recombination rate of state $|\downarrow\rangle$. The reduced atom number is also responsible for the breakdown of the Thomas-Fermi approximation.

Scattering in the higher dressed state

In the next series of experiments, we consider the scattering properties of the higher dressed state $|+\rangle$. There, besides elastic collisions, two-body inelastic collisions leading to a change of the two-particle dressed state are also allowed. For our typical experimental parameters they limit the lifetime of the BEC to ~ 1 ms. The upper panel of Fig. 4.6 sketches the two possible inelastic processes: ① $|{+}{+}\rangle \to |{-}{-}\rangle$ and ② $|{+}{+}\rangle \to (|{+}{-}\rangle + |{-}{+}\rangle)/\sqrt{2}$. Both lead to the creation of correlated atom pairs with opposite momenta. They are accompanied by an energy release of either $\hbar\tilde{\Omega}$ or $\hbar\tilde{\Omega}/2$ per atom, corresponding to the energy gap between the two-particle dressed states. Similar processes occur in Raman-coupled BECs[107].

To reveal these dressed-state changing collisions, we prepare rapidly with a ramp rate of 500 kHz/ms, a pure sample of $|+\rangle$ atoms. We then immediately switch off the trap and let the gas expand for a time t_{exp}. During the first 1 ms the rf-field is kept on, allowing us to characterize the decay processes in the absence of the trap. As depicted in the lower panel of Fig. 4.6, the time-of-flight images reveal the presence of halos of atoms expanding away from the condensate.

Since atoms in a BEC scatter with extremely low relative momenta, the halo radius R_H at time t_{exp} directly reflects the velocity of the collision products $v_f = R_H/t_{\mathrm{exp}}$. Processes ① and ② can be distinguished because the velocities are given by $v_1 = \sqrt{2\hbar\tilde{\Omega}/m}$ and $v_2 = \sqrt{\hbar\tilde{\Omega}/m}$ respectively, where m is the mass of ^{39}K. In these expressions, we have neglected the released mean-field energy of the BEC since the corresponding correction remains well below our experimental resolution.

Interestingly, we observe that the likelihood of the two processes depends on the dressed state composition, and thus on δ.

Figure 4.7 presents a more systematic study of these inelastic processes as a function of the parameters of the coupling field. Therefore, we model the halo by a spherical shell with a Gaussian profile centred around the BEC and extract its parameters by fitting the time-of-flight images with its forward Abel transform. The left panel of Fig. 4.7 depicts the velocity of the atoms in each halo versus $\tilde{\Omega}$, determined by measuring R_H for different values of t_{exp}. For simplicity, we perform the experiments at only two particular values of δ. This ensures that only one of the two inelastic decay processes is significant in each measurement and the images have a single halo. The measurements are in excellent agreement with the theory predictions neglecting the BEC mean-field energy without any fitting parameters (solid and dashed lines).

The scattering cross section of the two processes strongly depends on detuning. This can be clearly seen in the right panel of Fig. 4.6, where we plot the fraction of atoms scattered in each halo N_{sc}/N as a function of δ extracted from the same set of images as Fig. 4.6(d). The rate equation describing the evolution of the density in the initial state reads $\dot{\rho} = -2(\Gamma_1 + \Gamma_2)\rho = -2G^{(2)}(\sigma_1 v_1 + \sigma_2 v_2)(\rho^2/2)$. Here $\Gamma_{1,2}$ are the inelastic scattering rates for processes ① and ②, $G^{(2)} = 1$ is the BEC two-body correlation function, $\rho^2/2$ is the density of atom pairs, and $\sigma_1 = \pi\left[(a_{\uparrow\uparrow} + a_{\downarrow\downarrow} - 2a_{\uparrow\downarrow})\sin^2 2\theta\right]^2/2$ and $\sigma_2 = 4\pi[\left(a_{\uparrow\uparrow}\sin^2\theta - a_{\downarrow\downarrow}\cos^2\theta + a_{\uparrow\downarrow}\cos 2\theta\right)\sin 2\theta]^2$ are the corresponding scattering cross sections[103]. Our measurements agree qualitatively with the expected $\Gamma_{1,2}$ line shapes, see inset. For a quantitative prediction, the simultaneous reduction of ρ due to the 1 ms expansion of the cloud (which depends on δ *via* a_{++}) must be taken into account. For $\delta \sim 0$, the expansion can be neglected and $\sigma_2 \sim 0$, greatly simplifying the dynamics. In this regime, integration of the rate equation yields $N/N_{\mathrm{sc}} \sim 0.28$ for an initial density $\rho \sim 1.3 \times 10^{14}$ atoms/cm^3, in good agreement with the experiment.

Rf-dressed solitons

After demonstration of the different collisional couplings present in dressed BECs, we refocus on the lower dressed state $|-\rangle$ and exploit the broad tunability of its effective scattering length to explore attractively interacting systems. In optical waveguides, this situation enables the study of bright solitons: matter-wave packets that propagate without changing their shape because attractive non-linearities balance the effect of dispersion along the unconfined direction[79,123].

In coherently-coupled systems, they are formed by dressed atoms constituting dressed-state bright solitons. Compared to conventional bright solitons, they are bound by an additional mean-field attractive non-linearity which scales with density

as an effective three-body force. This term results from the density-dependent detuning appearing when $a_{\downarrow\downarrow} \neq a_{\uparrow\uparrow}$, which yields a differential mean-field frequency shift. For our experimental parameters, its effects are small and remain below our experimental resolution. The dressed-state bright solitons are only stable while the gas is effectively one dimensional, with an interaction energy that remains below $\hbar\omega_r$ [85,124,125].

To observe this new type of bright soliton, we study the dynamics of a BEC in state $|-\rangle$ after release in the optical waveguide. The magnetic field is set to $B = 56.000(2)$ G, where $a_{\uparrow\uparrow}/a_0 = 35.1$, $a_{\downarrow\downarrow}/a_0 = 57.9$, $a_{\uparrow\downarrow}/a_0 = -53.5$, and a_{--} can take negative values, see top panel of Fig. 4.8. We adiabatically prepare the system at different values of the detuning with a ramp rate of 1 kHz/ms. For $a_{--} < 0$ we keep the initial atom number below $N \sim 3000$ to avoid collapse. To prepare such small samples, we start with a BEC in state $|\downarrow\rangle$ and exploit its large three-body recombination rate to reduce the atom number. We then remove the axial confinement in 15 ms, allowing for free evolution in the waveguide. The lower panel of Fig. 4.8 shows *in situ* images after an evolution time t_g. Whereas for $\delta/2\pi = \pm 250$ kHz the gas expands, as expected for a repulsive BEC in states $|\uparrow\rangle$ or $|\downarrow\rangle$, for $\delta = 0$ its shape remains unchanged. Here $a_{--}/a_0 = -3.5$ and we observe the formation of a single dressed-state bright soliton.

Interaction quench into the attractive regime

In the last series of experiments, we explore the response of the system to a quench of the effective scattering length from repulsive to attractive values. As demonstrated in recent experiments [126,127], this triggers a modulational instability in the BEC: a mechanical instability where fluctuations in the condensate density are exponentially enhanced by the attractive non-linearity. Consequently, the gas splits into several components. The growth of the density modulation is dominated by the most unstable Bogoliubov modes, which have characteristic momentum $k_{\mathrm{MI}} \sim 1/\xi$. Here $\xi = a_{\mathrm{ho}}/\sqrt{4\,|a_{--}|\,\rho_{1\mathrm{D}}}$ is the healing length of the BEC in the waveguide, $a_{\mathrm{ho}} = \sqrt{\hbar/m\omega_r}$ is the radial harmonic oscillator length, and $\rho_{1\mathrm{D}}$ is the line density of the system before the quench. The characteristic length and time scales of this process are $\lambda = 2\pi/k_{\mathrm{MI}}$ and $\tau_{\mathrm{MI}} = 2m/\hbar k_{\mathrm{MI}}^2$, respectively. For $t > \tau_{\mathrm{MI}}$, each of the components evolves into a bright soliton, forming a soliton train [123,128–131]. For a system of size L at the moment of the quench, the average number of solitons is expected to be $N_S = L/\lambda$ from length scale arguments [129]. This prediction has been verified experimentally only in a restricted range of scattering lengths due to limitations in the quench timescales [126,127].

Our experimental sequence is summarized in the top panel of Fig. 4.9. The starting point is a BEC of $65(15) \times 10^3$ atoms confined in a crossed trap. The

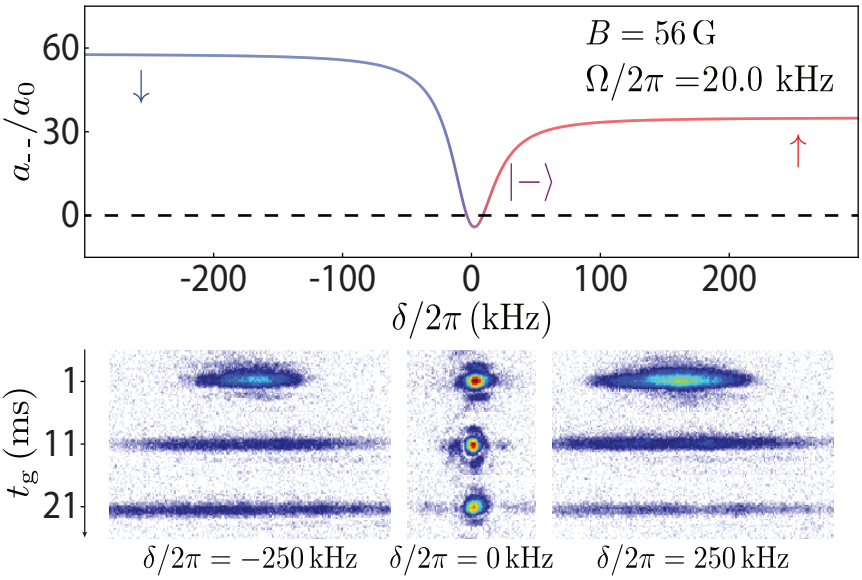

Figure 4.8: Formation of a dressed-state bright soliton. **Top:** calculation of a_{--} versus δ with eq. (3.27) for rf-coupling ($k_R = 0$). Near zero detuning, the effective scattering length becomes negative: $a_{--} < 0$. **Bottom:** *in situ* dynamics of the gas after an evolution time t_g in the optical waveguide. For $\delta/2\pi = 0$ ($a_{--}/a_0 = -3.5$) a self-bound bright soliton forms. For $\delta/2\pi = 250$ kHz ($N = 9(2) \times 10^4$) and $\delta/2\pi = -250$ kHz ($N = 1.0(2) \times 10^4$), $a_{--} > 0$ and the gas expands. Figure is taken from Ref. [106].

initial trap frequencies in the crossed optical dipole trap are $(\omega_x, \omega_y, \omega_z)/2\pi = (26(1), 190(1), 188(1))$ Hz, and the radial frequency in the optical waveguide is $\omega_r/2\pi = 188(1)$ Hz. At $t = 0$ we switch off the axial confinement and let the atoms expand in the waveguide for $t_g = 11$ ms, reaching a size $L \sim 112\,\mu$m. At this point, we abruptly change δ with a ramp rate of 1 kHz/μs, effectively quenching the scattering length from $35.1\,a_0$ to its final value. An additional expansion time of 10 ms allows the development of the modulational instability and the formation of a soliton train, which we image *in situ*.

The lower panel of Fig. 4.9 shows the average number of components observed per image N_S as a function of the final detuning. We determine the number of components with an algorithm similar to the one presented in Ref. [127]. Whereas the initial BEC has $N_S = 1$, for all values of δ such that $a_{--} < 0$ we measure $N_S > 1$. The maximum number of solitons in a train is observed at $\delta/2\pi = 2.3$ kHz, which corresponds to the most attractive value of $a_{--}/a_0 = -4.2$. This value is 2.5 larger than in previous experiments, where interactions were controlled using magnetic Feshbach resonances[126,127]. Indeed, our dressed-state approach enables ramp rates orders of magnitude faster, ensuring a clear separation of timescales vs.

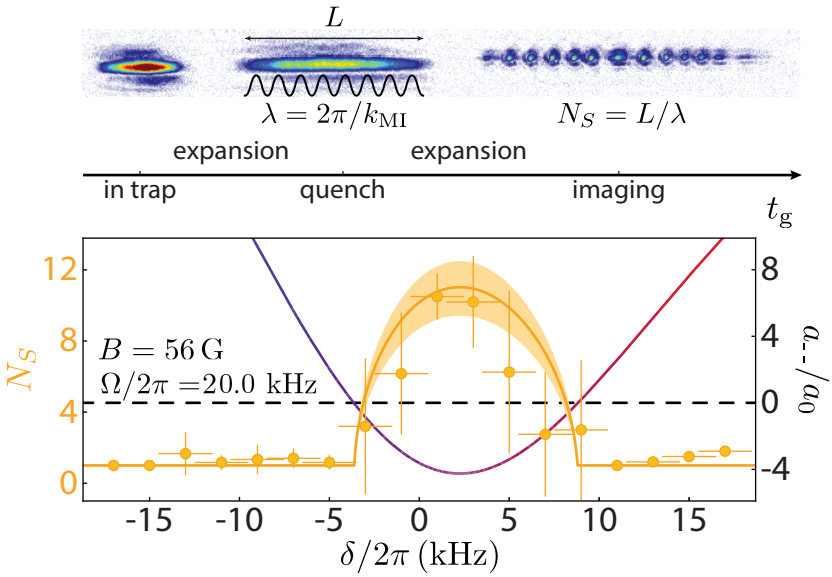

Figure 4.9: Modulational instability and formation of bright soliton trains. **Top:** sketch of the experimental sequence and exemplary *in situ* images. **Bottom:** number of components observed per image N_S vs. δ after the interaction quench (orange circles). Error bars indicate the standard deviation of 4 to 6 independent measurements (vertical) and the uncertainty of δ (horizontal). Orange line, left axis: theory prediction $N_S = L/\lambda$ (shaded area: uncertainty due to the systematic error in the atom number). Colored line, right axis: a_{--} (colorscale: value of P). Figure is taken from Ref. [106].

τ_{MI} and making three-body recombination processes during the quench negligible. As a result, we are able to verify the validity of the scaling prediction $N_S = L/\lambda$ in a much broader range of parameters. Quantitative studies of the modulational instability require a timescale for the interaction quench that is clearly separated not only from τ_{MI}, but also from the characteristic three-body recombination time. Otherwise, atom losses during the quench modify the density of the gas, changing λ. Here we realize peak ramp rates $-5 \times 10^4 a_0/\mathrm{ms}$ with rf-dressing in contrast to $\sim -6\, a_0//\mathrm{ms}$ in Ref. [126] with a magnetic Feshbach resonance. This increased speed is key to maintain the separation of timescales and verify the scaling law in a broader range of interaction strengths.

General view on rf-coupling as technique for interaction control

In the last paragraphs we have investigated the elastic and inelastic scattering properties of rf-coupled Bose-Einstein condensates. Below, we shortly discuss rf-dressing in BECs as technique for interaction control on a more general level and comment on the tuning range and the rate of change of the effective scattering

length in principle available in experiments.

The effective scattering length in the lowest dressed state $|-\rangle$ can be rewritten in terms of the polarization $P = \delta/\widetilde{\Omega}$ as

$$a_{--} = a_1 + a_3 P + a_2 P^2, \tag{4.1}$$

where we have defined $a_1 = (a_{\uparrow\uparrow} + a_{\downarrow\downarrow} + 2a_{\uparrow\downarrow})/4$, $a_3 = (a_{\uparrow\uparrow} - a_{\downarrow\downarrow})/2$, and $a_2 = (a_{\uparrow\uparrow} + a_{\downarrow\downarrow} - 2a_{\uparrow\downarrow})/4$ following the notation of Ref. [132]. This expression shows that the range of tunability of a_{--} is maximized by selecting systems with large values of a_3 and/or a_2, i.e. situations where $a_{\uparrow\uparrow}$ and $a_{\downarrow\downarrow}$ are very different and/or where $a_{\uparrow\downarrow}$ is large. In practice, one should also be able to prepare the corresponding system. This imposes that at least one of the two intra-state scattering lengths ($a_{\uparrow\uparrow}$ or $a_{\downarrow\downarrow}$) is positive, to have a stable BEC in the initial state. For the experiments reported in this section, we use a configuration where both $a_{\uparrow\uparrow}$ and $a_{\downarrow\downarrow}$ are positive because this allows us to adiabatically prepare the rf-dressed states starting from both negative and positive values of the detuning. Moreover, due to the negative sign of $a_{\uparrow\downarrow}$ it is possible to set the effective scattering length to zero and to reverse its sign.

However, since the three bare scattering lengths have relatively small values, this configuration is clearly suboptimal concerning the range of tunability of a_{--}. In this respect, a more favourable configuration consists on maximizing a_3 by using states $|\downarrow\rangle = |F = 1, m_F = 1\rangle$ and $|\uparrow\rangle = |F = 1, m_F = 0\rangle$ at $B \sim 396$ G, where $a_{\downarrow\uparrow} \sim -6\,a_0$, $a_{\uparrow\uparrow} \sim 1\,a_0$, and $a_{\downarrow\downarrow} > 0$ is large and widely tunable using a Feshbach resonance[133]. This situation allows one to tune the scattering length on a much broader range. Another possibility is to maximize instead a_2, for example by using states $|\downarrow\rangle = |F = 1, m_F = 0\rangle$ and $|\uparrow\rangle = |F = 1, m_F = -1\rangle$ at $B \sim 114$ G. There, $a_{\downarrow\downarrow} \sim -22\,a_0$, $a_{\uparrow\uparrow} \sim 8\,a_0$, and $a_{\downarrow\uparrow}$ is large and widely tunable with a broad interstate Feshbach resonance[119].

When performing a detuning sweep, the rate of change of the effective scattering length in state $|-\rangle$ can be expressed as

$$\frac{\partial a_{--}}{\partial t} = \frac{\partial \delta}{\partial t}\frac{\partial P}{\partial \delta}\frac{\partial a_{--}}{\partial P} = \frac{\dot{\delta}}{\widetilde{\Omega}}\left(1 - P^2\right)\left(a_3 + 2Pa_2\right). \tag{4.2}$$

This expression shows that $\dot{a}_{--}$ varies with P during the detuning ramp, and that larger ramp rates can be obtained by selecting magnetic fields where a_3 and/or a_2 are large. From the experimental point of view, the detuning ramp must be sufficiently slow to avoid diabatic transitions from the lower to the higher dressed state. For a linear ramp, the probability of such transfer is given by the well-known Landau-Zener formula and imposes the adiabaticity condition $\dot{\delta} < \Omega^2$. For the maximal Rabi frequency and ramp rate used in the experiments $\Omega/2\pi = 20$ kHz

and $\dot{\delta}/2\pi \sim 1$ kHz/µs, we estimate a probability of transfer $< 2\%$, in agreement with our observations.

In our experiment, the Rabi frequency is limited by the available rf power. In principle, the ramp speed could be increased by several orders of magnitude if the coupling was performed optically, using two-photon transitions induced by co-propagating Raman beams. For a Raman wavelength corresponding to the potassium tune-out wavelength $\lambda = 769$ nm, which avoids parasitic trapping potentials, Rabi frequencies $\Omega/2\pi \sim 1$ MHz and ramp rates $\dot{\delta}/2\pi \sim 1$ MHz/µs should be readily accessible.

Moreover, dressed states can also be prepared *via* rf-pulses followed by a phase jump of the driving field[104]. This enables interaction quenches as fast as those obtained by performing a π-pulse between two states of different scattering lengths. Note however that, compared to an rf π-pulse, rf-dressing (implemented using rf-sweeps, as in this paper, or in a pulsed manner, as in Ref. [104]) is a more flexible interaction control tool. First, it allows one to control the interaction strength in a continuous manner between $a_{\uparrow\uparrow}$ and $a_{\downarrow\downarrow}$, without being limited to those two discrete values, and even yields systems with effective interaction strengths outside that range thanks to the effect of $a_{\uparrow\downarrow}$. Second, it enables interaction changes at any rate, from adiabatic to sudden, and is not just limited to quenches. And third, it allows one to perform fast temporal modulations of the effective scattering length with complex waveforms, such as those required to implement Floquet-engineering schemes of the interaction term[134–136].

4.3 Conclusion

In conclusion, we investigated the effective scattering properties in a ^{39}K BEC where two components with unequal intrastate interaction are coherently coupled *via* radio-frequency. The effective single-component interaction depends on the bare state scattering lengths and the spin composition of the system, and thus can be tuned by the parameters of the coupling field.

The effective interaction strength was derived in a more general form for Raman coupling in chapter 3 in eq. (3.27). In the case of $k_R \neq 0$ as in Raman coupling, eq. (3.27) was investigated in Ref. [107] for equal intrastate interactions. The exploration of $k_R \neq 0$ and additionally unequal intrastate interactions, will be subject of chapter 7. For $k_R = 0$ as for rf-coupling, the modification in the effective scattering length was previously only observed in a small range of interactions in the group of Prof. Oberthaler[104,105] and Prof. Hirano[120]. We here presented the first direct measurements of the effective elastic scattering length over a range of $100\,a_0$. We also explored rf-coupling as method to control interactions in the at-

tractive range and observed the formation of rf-dressed solitons. Moreover, we have demonstrated that the method also allows for fast temporal control by studying how the modulational instability triggered by an interaction quench develops into a bright soliton train.In a broader context, our study demonstrated coherent coupling as alternative method to control interactions in a Bose-Einstein condensate. Common techniques for interaction control are magnetic Feshbach resonances[137] or optical Feshbach resonances[138,139] which suffer however from temporal limitations or light-induced inelastic collisions, respectively[116]. These drawbacks can partially be overcome with optical control of magnetic Feshbach resonances[140–144]. As we have shown in this chapter, as complementary method coherent coupling could be employed, which can be used to control interactions in a fast and flexible manner and within a broad range of interactions strengths.

Our work suggests inelastic collisions from the higher dressed band as novel source for correlated atom pairs for atom optics experiments, complementary to other reported approaches[9,145–148]. Furthermore, rf-coupled BECs with attractive interactions are an exiting platform to investigate beyond mean-field (BMF) effects. As predicted in Ref. [149], they are expected to host novel types of non-linearities for which BMF corrections are relevant. In the weak coupling limit, these resemble three-body forces and could stabilize new types of quantum droplets. In fact, after publication of our work, the group of Prof. Bourdel reported in Ref. [150] the study of BMF effects in a rf-dressed condensate as function of the coupling strength and the observation of a three-body force caused by BMF effects. Moreover, they showed in Ref. [151] that an effective attractive three-body interaction with significant larger magnitude can be engineered on the mean-field level with rf-coupling. The concept is based on spin composition dependent effective interactions as investigated in this chapter and density induced mean-field shifts which affect the spin composition.

5 Experimental implementation of Raman coupling

This chapter is devoted to the implementation of Raman coupling in our potassium Bose-Einstein condensate. In order to find the most suitable experimental parameters, we introduce the atomic Hamiltonian in an external magnetic field and calculate the ratio between Raman coupling strength and inelastic photon scattering rate from the Raman beams. We discuss our choice of parameters like magnetic field, Raman wavelength and atomic states for the two bosonic isotopes of potassium, ^{39}K and ^{41}K. In the last part we describe the setup, the procedure of optical alignment and establish common techniques to characterize the Raman-coupled system.

In chapter 2, we have introduced the encoded Hamiltonian of the chiral BF theory we want to simulate. Afterwards, we have shown that a realization can be achieved with a Raman-coupled BEC with unequal intrastate interactions (see chapter 3). We presented our experimental system, a potassium BEC of ^{39}K or ^{41}K, in chapter 4 and studied the effective interaction control available in ^{39}K *via* coherent coupling. In this chapter, we turn to the second experimental ingredient for realizing an effective Hamiltonian identical to the encoded chiral BF theory: the experimental implementation of Raman coupling.

Raman dressing is a well-known technique in the toolbox for manipulating ultracold quantum gases. It was first used in the group of Prof. Spielman to generate an artificial light-induced vector potential in BECs of ^{87}Rb[99]. Thereafter, Raman coupling in continuum systems similar to what is considered in this thesis, continued to be used in Bose-Einstein condensates of ^{87}Rb, e.g. in Refs. [98–102,107,152–160]. It was also implemented in a BEC of ^{23}Na[161], where lattice band pseudospins instead of internal atomic states were coupled, as well as in fermionic degenerate gases of ^{40}K[162,163], ^{6}Li[164], ^{161}Dy[165] and ^{173}Yb[166]. Moreover, it has also been applied in lattice systems[167–170]. To our knowledge, we report for the first time on Raman coupling in a Bose-Einstein condensate of potassium atoms.

5.1 Relevant parameters of the Raman coupling scheme

This section deals with the parameters of Raman coupling, i.e. involved internal states, magnetic field, wavelength of the Raman light and frequency difference between the two beams. We start with the theoretical base, namely review the Hamiltonian of an atom in an external magnetic field to find the transition energies and calculate the ratio between Raman coupling strength and inelastic photon scattering rate from the beams. Afterwards we apply these findings to our experimental system and motivate our choice of experimental parameters.

5.1.1 Derivation of atom-light interaction rate

Hamiltonian of an atom in an external magnetic field

An atom at rest in an external magnetic field B is described with the Hamiltonian

$$H_a = H_F + H_{HF} \text{ with } H_F = c_f \mathbf{L}\cdot\mathbf{S}, H_{HF} = c_{hf1}\mathbf{L}\cdot\mathbf{I} + c_{hf2}\mathbf{S}\cdot\mathbf{I} \tag{5.1}$$

with c_f, c_{hf1}, c_{hf2} the fine and hyperfine constants. The part H_F captures the fine structure splitting of the atomic energy levels which is caused by the coupling between the electronic orbital momentum $\mathbf{L}$ and electronic spin $\mathbf{S}$. The second contribution H_{HF} stems from the coupling between the electronic angular momenta and nuclear spin $\mathbf{I}$.

An applied external magnetic field B leads to an additional contribution, so

$$H = H_F + H_{HF} + H_b \text{ with} \tag{5.2}$$

$$H_b = \mu \cdot \mathbf{B} = \mu_B(g_L \mathbf{L} + g_S \mathbf{S} + g_I \mathbf{I}) \cdot \mathbf{B}, \tag{5.3}$$

and μ_B the Bohr magneton, g_S the electron g-factor and g_L, g_I the orbital and nuclear gyromagnetic factors respectively. The Hamiltonian H_b energetically splits the eigenstates of $H_F + H_{FS}$ into magnetic sub-levels, which is the well-known Zeeman effect.

The overall Hamiltonian has eigenstates depending on the strength of the magnetic field. At low magnetic field values, the Hamiltonian H_b can be treated as perturbation. In this case an appropriate basis is $|J, F, m_F\rangle$, composed out of the atom's total momentum $\mathbf{F} = \mathbf{J} + \mathbf{I}$ and its projection m_F on the quantization axis with $-F \leq m_F \leq +F$. Here $\mathbf{J}$ is the quantum number of the total electronic angular momentum $\mathbf{J} = \mathbf{L} + \mathbf{S}$.

At sufficient high magnetic fields, the so called Paschen-Back regime, the energy splitting E_B given by eq. (5.3) gets large enough so it is appropriate to treat H_{HF} as perturbation instead. Then nuclear and electronic momenta get decoupled and the good basis is $|J, I, m_J, m_I\rangle$. At significantly higher magnetic field strengths, where $E_B \gg c_f$, even $\mathbf{L}$ and $\mathbf{S}$ get decoupled and the fine structure is mixed. However, $c_f \sim 2\pi\hbar \times 1$ THz for alkali-metal atoms and for all feasible magnetic field values in our experiment, the fine structure is robust against the magnetic field and $\mathbf{J}$ remains a good quantum number.

Even though the eigenstates change with the magnetic field, it can be shown that the eigenvalues in the case of an alkali atom in the ground state (which implies $J = 1/2$) for all magnetic field strengths are given by the analytic Breit-Rabi formula:

$$E_B(m_F) = -\frac{A_{hf}}{8} + g_I \mu_B m_F B \pm \frac{A_{hf}}{4}\left(I + \frac{1}{2}\right)\sqrt{1 + \frac{2m_F}{I + (1/2)}x + x^2} \tag{5.4}$$

with $x = 2\mu_B B(g_J - g_I)/(A_{hf}(I + (1/2)))$ and A_{hf} the hyperfine energy splitting between $F = 1$ and $F = 2$ of the $4^2S_{1/2}$ ground state. The energies of the ^{41}K and ^{39}K ground manifold as function of the magnetic field are shown in Fig. 5.2. In our experiment, we work with the $|\downarrow\rangle, |\uparrow\rangle$ states which are two Zeeman sub-levels of the $F = 1$ ground state manifold at low field. We can apply eq. (5.4) and the energy difference between the two can be calculated with $\hbar\omega_0 = E_B(\uparrow) - E_B(\downarrow)$ for all magnetic fields.

Ratio of coupling strength to inelastic scattering rate

In chapter 3, we have seen that Raman coupling offers great possibilities to engineer and control interesting energy-momentum relations. However, it has the drawback of reducing the atomic lifetime. The atoms inelastically scatter photons of the Raman beams with rate Γ_{in}. In the limit where the atom energy after the scattering process is much larger than the trap depth, the atom will be lost and the scattering rate corresponds directly to the atom loss rate. Otherwise the atom remains in the trap with an increased energy, thermalization then leads to an overall increase in temperature and hence atom loss due to evaporation of the most energetic atoms.

The effect of inelastic scattering is conveniently quantified by the ratio $\beta = \frac{\Omega_R}{\Gamma_{in}}$. This ratio describes the probability that an atom completes a Raman cycling transition before undergoing an inelastic scattering event. In particular, the larger β is, the more robust is the process against losses.
In our experiment we are interested in working in the single minimum regime, implying relatively high values of Ω_R, while minimizing the scattering rate. Thus, we identify the optimal settings of the coupling field at the point where β is maximized. In the following, we will present the calculation of R. Wei out of Ref. [171] without major modifications and retrace it to obtain the ratio β for our experimental parameters. In particular, we want to compute β as function of the magnetic field strength.

The two-photon Raman coupling strength Ω_R between $|\downarrow\rangle, |\uparrow\rangle$ is given by

$$\Omega_R = \sum_{\mu} \frac{\hbar\Omega_{1,\mu}\Omega_{2,\mu}}{4\Delta} + \sum_{\upsilon} \frac{\hbar\Omega_{1,\upsilon}\Omega_{2,\upsilon}}{4(\Delta + A_f)} \tag{5.5}$$

with $\Omega_{i,f}$ the single-photon Rabi frequency of the ground state g_i with $i \in \{\downarrow, \uparrow\}$ to the excited state e_f with $f \in \{\mu, \upsilon\}$. Here μ represents an excited state from the lower fine-structure manifold, corresponding to the $D1$ transition (see Fig. 4.1), υ one from the $D2$ manifold. A_f is the fine structure splitting, namely the splitting of the excited states $A_f = E_\upsilon - E_\mu$ and $\Delta = \hbar\omega - (E_\mu - E_g)$ is the detuning of the coupling light from the D1-transition. Note that we do not take any two-photon detuning δ_0 into account and we approximate the two frequencies ω_1, ω_2 of the coupling light with ω. The single-photon Rabi frequency $\Omega_{i,f}$ can be calculated with the electronic dipole $\mathbf{d} = e \cdot \mathbf{r}$:

$$\Omega_{i,f} = \frac{E\langle g_i|\mathbf{d}|e_f\rangle}{\hbar}. \tag{5.6}$$

where E is the electric field amplitude. Experimentally we can only measure the light intensity I which is related to E by $I = \epsilon_0 c E^2/2$ with the dielectric constant ϵ_0 and speed of light c.

The formula for the two-photon Rabi frequency in eq. (5.5) can be simplified, as noticed by the authors in Ref. [171]. The quadrupole matrix elements $\langle g_i|d_a d_b|g_j\rangle \neq 0$ only if $i = j$, as the dipole operator does not couple to the spin, and for dipole moments along the same direction: $a = b$ with $a, b \in \{x, y, z\}$. Therefore, the sum $\sum_\mu \Omega_{1,\mu}\Omega_{2,\mu} + \sum_\upsilon \Omega_{1,\upsilon}\Omega_{2,\upsilon} = 0$. By inserting this relation in eq. (5.5), the two-photon Raman coupling strength can be expressed as

$$\Omega_R = \frac{\hbar A_f}{4\Delta(\Delta - A_f)} \sum_\mu \Omega_{\downarrow\mu}\Omega_{\uparrow\mu}, \tag{5.7}$$

so it is sufficient to calculate the coupling strengths to the D1 manifold.

The inelastic photon scattering rate caused by the coupling field can be described by

$$\Gamma_{in} = \gamma \left(\sum_\mu \frac{\hbar^2(\Omega_{\downarrow\mu}^2 + \Omega_{\uparrow\mu}^2)}{4\Delta^2} + \sum_\upsilon \frac{\hbar^2(\Omega_{\downarrow\upsilon}^2 + \Omega_{\uparrow\upsilon}^2)}{4(\Delta + A_f)^2} \right) \tag{5.8}$$

Here, the two sums $\sum_\mu$ and $\sum_\upsilon$ represent the contributions of the D1- and D2-transitions, and take both the $|\downarrow\rangle$ and $|\uparrow\rangle$ state into account. Each sum contribution stems from the probability to excite an atom from the ground state g_i with $i \in \{\downarrow, \uparrow\}$ to a specific excited state e: $\hbar\Omega_{g,e}^2/2\Delta^2$, times the probability to decay back into the ground state manifold. The latter is approximated with the global linewidth γ for all transitions as we assume that the Raman light is largely detuned with respect to the hyperfine splitting.

The formulas in eq. (5.7) and (5.8) can be greatly simplified for values of detuning much larger than the fine structure splitting: $\Delta \gg A_f$. In this case we have $\Omega_R \propto A_f/\Delta^2$ and $\Gamma_{in} \propto \gamma/\Delta^2$.

For the calculation of eq. (5.7) to eq. (5.8), the single-photon Rabi frequencies $\Omega_{i,f}$, which are determined by the electric dipole element, are needed. As explained in the previous paragraph, the eigenstates of an atom in an external magnetic field strongly depend on the magnetic field strength. Hence we cannot use the basis $|J, F, m_F\rangle$ throughout the computation. Instead the eigenstates can be expressed as a sum $|J, Q\rangle = \sum_{m_L, m_S, m_I} \langle m_L, m_s|J, m_J\rangle c^Q_{m_J, m_I} |J, m_J, m_I\rangle$ for all magnetic field values, where Q denotes an eigenstate within the specific J manifold. The electric dipole element of a system in state $|J, m_J, m_I\rangle$ can be written in terms of the reduced dipole element

$$\langle J_i, m_{J,i}, m_{I,i}| er_q |J_f, m_{J,f}, m_{I,f}\rangle = \delta_{m_{I,i}, m_{I,f}} W^{J_f, J_i}_{m_{J,f}, q, m_{J,i}} \langle J_i| |er_q| |J_f\rangle, \tag{5.9}$$

where we have used the Wigner-Eckart theorem. The Kronecker delta function $\delta_{m_{I,i}, m_{I,f}}$ occurs because the electric dipole operator does not couple to the spin. For the same reason $m_{S,i} = m_{S,f}$ in the next steps. The abbreviation q denotes the

light polarization. Linearly polarized light is represented with $q = 0$, right circular and left circular with $q = \pm 1$ respectively. Momentum conservation during the atom light interaction is ensured by

$$W^{J_f,J_i}_{m_{J,f},q,m_{J,i}} = (-1)^{-J_f+1-m_{J,i}}\sqrt{2J_i+1}\begin{bmatrix} J_f & 1 & J_i \\ m_{J,f} & q & -m_{J,i}\end{bmatrix}, \tag{5.10}$$

where the square brackets denote the Wigner $3j$ symbol. As it is zero unless $m_{J,f} + q - m_{J,i} = 0$, circular polarized light is needed to change the magnetic quantum number m_J.

Summing up, for any eigenstate $|J, Q\rangle$ of Hamiltonian (5.3) one has

$$\langle J_i, Q_i| \, er_q \, |J_f, Q_f\rangle = \sum_{m_{L,i},m_{L,f},m_I,m_S} c_{m_{L,i},m_s,J_i,m_{J,i}} c^{Q_i}_{m_{J,i},m_I} c_{m_{L,f},m_s,J_f,m_{J,f}} c^{Q_f}_{m_{J,f},m_I} \\ W^{J_f,J_i}_{m_{J,f},q,m_{J,i}} \langle J_i| \, |er_q| \, |J_f\rangle \, . \tag{5.11}$$

Here $c_{m_{L,i},m_s,J_i,m_{J,i}} = \langle m_{L,i}, m_s|J_i, m_{J,i}\rangle$ and $c_{m_{L,f},m_s,J_f,m_{J,f}} = \langle m_{L,f}, m_s|J_f, m_{J,f}\rangle$. The reduced dipole matrix element $\langle J_i| \, |er_q| \, |J_f\rangle$ can be deduced from the lifetime τ_{m_i,m_f} of the transition between m_i and m_f. It is

$$A_{J_i,J_f,m_i,m_f} = \frac{1}{\tau_{m_i,m_f}} = \frac{\omega_0^3 |\langle J_i| \, |er_q| \, |J_f\rangle|^2}{3\pi\epsilon_0\hbar c^3} \\ \equiv \frac{\omega_0^3}{3\pi\epsilon_0\hbar c^3}(2J_i+1)|\langle J_i| \, |er_q| \, |J_f\rangle|^2 \sum_q \begin{bmatrix} J_f & 1 & J_i \\ m_f & q & -m_i\end{bmatrix}^2 \tag{5.12}$$

Usually the lifetimes of the different initial m_i states are not resolved in a measurement, instead the total lifetime τ is measured. Summing over all channels, we obtain for the reduced dipole matrix element

$$\langle J_i||d||J_f\rangle = \left(\frac{3\pi\epsilon_0\hbar c^3}{\omega_0^3\tau}\frac{(2J_f+1)}{(2J_i+1)}\right)^{1/2}. \tag{5.13}$$

We perform a numerical computation of Ω_R and Γ_{in} with the program Mathematica. The main task is the calculation of $c_{m_{L,i},m_s,J_i,m_{J,i}} c^{Q_i}_{m_{J,i},m_I}$ and $c_{m_{L,f}m_S}$, $c_{m_{L,f},m_s,J_f,m_{J,f}}$, $c^{Q_f}_{m_{J,f},m_I}$ in eq. (5.11), describing the probability that the corresponding sets of quantum numbers couple together. In the limit of low magnetic field, these would just correspond to the product of two Clebsch-Gordan coefficients. For arbitrary magnetic field values we can deduce these coefficients from the eigenvectors obtained by diagonalization of Hamiltonian (5.3) at one particular magnetic field value. The realization in Mathematica is straightforward, but care has to be taken to sort the

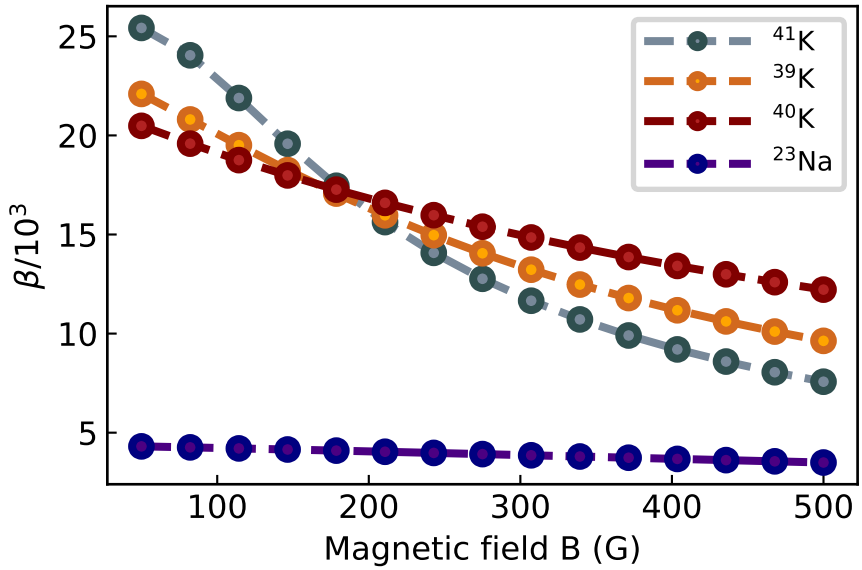

Figure 5.1: Numerical computation of the ratio $\beta = \Omega_R/\Gamma_{\text{in}}$ as function of the magnetic field B for $\Delta = -2\pi\hbar \times 100$ THz and the isotopes ^{23}Na, ^{41}K, ^{40}K and ^{39}K.

eigenvectors by increasing energy. Moreover, the eigenvectors calculated in Mathematica are not fully determined. The phase of the eigenvector is completely free. For different magnetic field values we can get arbitrary values for the phase, thus we get phase jumps which can be observed as sign changes in the values of the eigenvectors. To circumvent the problem, we specify additional constraints to fix the phase for all points. Concretely, we put the requirement that the maximum/or first non-zero value of each eigenvector has to be real. In addition, the eigenvectors are normalized.

The result of our numerical calculation is displayed in Fig. 5.1. We plot the ratio $\beta = \Omega_R/\Gamma_{\text{in}}$ in the magnetic field range $B = (50 - 400)$ G for different isotopes of potassium and ^{23}Na. To compare to the results of Ref. [171], the calculation is performed for a detuning of $\Delta = -2\pi\hbar \times 100$ THz. Moreover, we have assumed Raman beams with linear and circular polarization as $|\uparrow\rangle$, $|\downarrow\rangle$ differ in the magnetic quantum number. We find good agreement between our results and the values for ^{23}Na and ^{40}K reported in Ref. [171].

Our calculation in Fig. 5.1 illustrates two aspects: first, the ratio β is larger for heavier atoms. This is because heavier atoms have a larger fine structure splitting A_f than lighter atoms, e.g. $A_f = 2\pi\hbar \times 515$ GHz for ^{23}Na, whereas $A_f = 2\pi\hbar \times 1730$ GHz for ^{40}K. Second, the ratio β decreases with magnetic field. The reason lies in the hyperfine mixing with increasing magnetic field. The Raman

coupling can only couple to the orbital electronic momentum **L**, but not to the electronic or nuclear spin **S**, **I**. However, at low magnetic field, the coupling of **L**, **S**, **I** to the total atom's momentum **F**, leads to a coupling channel. As it diminishes with magnetic field, the coupling strength reduces while the inelastic photon scattering remains constant. It is interesting to notice that within the potassium isotopes, the ratio β decreases the fastest for ^{40}K, followed by ^{39}K and reduces the slowest for ^{41}K. This is compatible with the hyperfine structure splittings A_{hf} of the isotopes which fulfil $A_{\mathrm{hf},40} > A_{\mathrm{hf},39} > A_{\mathrm{hf},41}$. A smaller hyperfine structure splitting is less robust against the increasing magnetic field (i.e. the hyperfine levels get parallel earlier in the case of ^{41}K compared to ^{39}K as shown in Fig. 5.2) and the hyperfine mixing develops faster.

5.1.2 Choice of experimental parameters

Building on the theoretical understanding and predictions for the photon scattering rate *versus* magnetic field reported in the previous section, we explain in the following the chosen experimental settings for the Raman coupling scheme. We use the Raman recoil energy E_R and momentum k_R as natural units for all Raman parameters and momenta. However, we do not set E_R, k_R and $\hbar$ to 1. For other quantities we use SI units.

States

In our experiment, we prepare a Bose Einstein-condensate of ^{39}K or ^{41}K in a harmonic dipole trap in spin state $|{\downarrow}\rangle$ and couple it to state $|{\uparrow}\rangle$ with the Raman light. For all following experiments with Raman coupling we use different states than in chapter 4 where we investigated the modified effective interaction of rf-coupled states. From this point onwards, we use spin states which correspond at low magnetic field to two magnetic sub-levels of the $F = 1$ hyperfine ground manifold: $|{\downarrow}\rangle \equiv |1\rangle = |F = 1, m_F = 1\rangle$ and $|{\uparrow}\rangle \equiv |2\rangle = |F = 1, m_F = 0\rangle$ in the case of ^{39}K and $|{\downarrow}\rangle \equiv |2\rangle = |F = 1, m_F = 0\rangle$ and $|{\uparrow}\rangle \equiv |3\rangle = |F = 1, m_F = -1\rangle$ for ^{41}K. In the Paschen-Back regime these states correspond to

$$\begin{aligned} |{\downarrow}\rangle \equiv |1\rangle &= |I = 3/2, m_I = 3/2, J = 1/2, m_J = -1/2\rangle \\ |{\uparrow}\rangle \equiv |2\rangle &= |I = 3/2, m_I = 1/2, J = 1/2, m_J = -1/2\rangle \end{aligned} \tag{5.14}$$

for ^{39}K and

$$\begin{aligned} |{\downarrow}\rangle \equiv |2\rangle &= |I = 3/2, m_I = 1/2, J = 1/2, m_J = -1/2\rangle \\ |{\uparrow}\rangle \equiv |3\rangle &= |I = 3/2, m_I = -1/2, J = 1/2, m_J = -1/2\rangle \end{aligned} \tag{5.15}$$

for ^{41}K, respectively.
In some experiments, we make use of an auxiliary state, which is the remaining

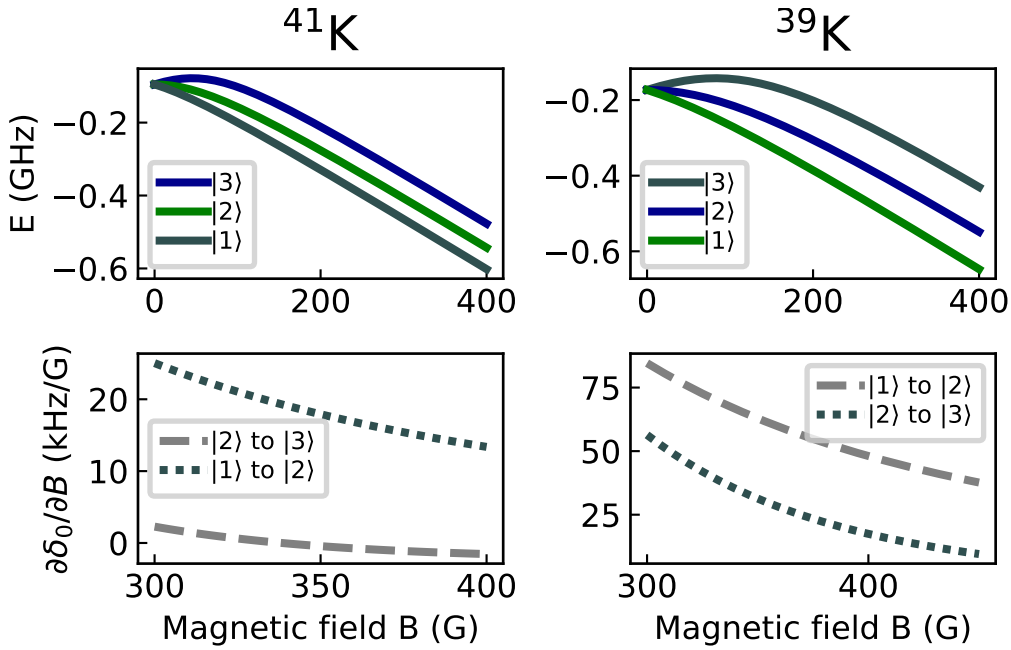

Figure 5.2: Magnetic field choice. **Top:** energy levels of the ground-state manifold as function of magnetic field B calculated with the Breit Rabi formula. **Bottom:** magnetic sensitivity of the transitions which we use as $|\downarrow\rangle$ to $|\uparrow\rangle$ and $|\downarrow\rangle/|\uparrow\rangle$ to $|\mathrm{aux}\rangle$ transitions in ^{41}K/^{39}K, respectively.

uncoupled state of the $F = 1$ hyperfine manifold. This means

$$\begin{aligned} |\mathrm{aux}\rangle \equiv |3\rangle &= |I = 3/2, m_I = -1/2, J = 1/2, m_J = -1/2\rangle \text{ for } ^{39}\mathrm{K} \\ |\mathrm{aux}\rangle \equiv |1\rangle &= |I = 3/2, m_I = 3/2, J = 1/2, m_J = -1/2\rangle \text{ for } ^{41}\mathrm{K} \end{aligned} \tag{5.16}$$

and $|\mathrm{aux}\rangle \equiv |3\rangle = |\mathrm{F} = 1, m_F = -1\rangle$ or $|\mathrm{aux}\rangle \equiv |1\rangle = |\mathrm{F} = 1, m_F = 1\rangle$ at low magnetic field, respectively.

Magnetic field

The choice of the magnetic field influences the Raman coupling in two ways. On the one hand - as we have seen in section 5.1.1 - the ratio β of Raman coupling strength to inelastic photon scattering rate monotonically decreases with increasing magnetic field. In this respect, it is in general more advantageous to work at lower magnetic field. On the other hand, the magnetic field defines the energy difference between the coupled states. The change in energy is in principle non-relevant, as we can easily realize the right frequency difference between the Raman beams with an adequate choice of acoustic-optical modulators (AOMs). However, it becomes important on the practical level because we have short term magnetic field fluctuations on the order of 15 mG. Because we couple states whose energies

depend on the magnetic field, these fluctuations directly translate into fluctuations of the two-photon detuning. In order to minimize changes in the detuning, one could invest much effort into an improved magnetic field stability involving an active feedback loop for ambient magnetic field noise. A much simpler solution is to consider the magnetic field sensitivity of the two-photon transition instead.

The energy of the magnetic sub-levels $|\downarrow\rangle$, $|\uparrow\rangle$ can be analytically calculated for all magnetic field strengths with the Breit-Rabi formula (see eq.5.4). We obtain the magnetic sensitivity of the Raman transition by taking the numerical derivative of the difference of the energy levels of the $|\uparrow\rangle$ and $|\downarrow\rangle$ state

$$\partial\delta_0/\partial B = \frac{1}{\hbar}\frac{\partial(E_\downarrow - E_\uparrow)}{\partial B}. \tag{5.17}$$

The magnetic sensitivity versus magnitude of magnetic field is shown in Fig. 5.2. As the latter is increased, the energy levels of $|\uparrow\rangle$, $|\downarrow\rangle$ are getting more parallel (see Fig. 5.2, upper panel) and hence the transition becomes less sensitive to magnetic field noise (lower panel). Analogously, we calculate the energy and magnetic sensitivity of the $|\mathrm{aux}\rangle$ state and the $|\mathrm{aux}\rangle$,$|\downarrow\rangle$ transition.

In the case of ^{41}K, the magnetic sensitivity of the $|\downarrow\rangle \equiv |2\rangle$ to $|\mathrm{aux}\rangle \equiv |1\rangle$ transition is slightly higher and therefore the $|\uparrow\rangle \equiv |3\rangle$, $|\downarrow\rangle \equiv |2\rangle$ states are a better choice for the Raman coupling. At a magnetic field of $B = 338.4$ G, we have for the transition between these states $\partial\delta_0/\partial B = 0$. Hence, the magnetic sensitivity of our chosen Raman transition is actually zero at this point and the two-photon detuning is insensitive to magnetic field changes. From Fig. 5.1 we conclude that the ratio β is still sufficiently high at this field strength. It reduces by ~ 2.5 from $\beta > 25 \times 10^3$ to $\beta = 10.7 \times 10^3$. Therefore, we choose to work at $B = 338.4$ G for all our experiments dealing with Raman coupling in ^{41}K.

In the case of ^{39}K, we have an additional constraint as we want to work in the vicinity of the Feshbach resonances of either $|\uparrow\rangle \equiv |2\rangle$ at ~ 57 G or $|\downarrow\rangle \equiv |1\rangle$ at ~ 400 G (see Fig.4.4). Because of the lower magnetic sensitivity we choose to work at the latter one. We choose the particular magnetic field value within a range of (374-397) G, depending on the scattering length needed in the experiment. At a magnetic field of 397 G, the magnetic sensitivity of the $|\downarrow\rangle \equiv |1\rangle$ to $|\uparrow\rangle \equiv |2\rangle$ transition is approx. 50 Hz/mG. Taking magnetic field fluctuations of 15 mG into account, this translates into a detuning uncertainty of approx. 750 Hz.

Interactions

For the isotope ^{41}K, the intra- and interspecies scattering lengths are nearly the same, precisely we have $a_{\downarrow\downarrow} = 61\ a_0$, $a_{\uparrow\uparrow} = 60.9\ a_0$ and $a_{\downarrow\uparrow} = 60.7\ a_0$ at $B = 338.4$ G.

For ^{39}K we can tune the scattering lengths between $a_{\downarrow\downarrow} \sim$ (25-252) a_0, $a_{\uparrow\uparrow} \sim$ (−5-1.5) a_0 and $a_{\downarrow\uparrow} \sim$ (−13.5-−6.5) a_0 in the operation range of $B =$ (374-397) G. The scattering lengths of ^{39}K as function of magnetic field are shown in the previous chapter in Fig. 4.4.

Wavelength of Raman light

For the Raman coupling we use light with wavelength $\lambda_R = 768.9$ nm, in the middle between the $D1$ and $D2$ resonances. This choice has two advantages: the first and most important one concerns the ratio $\beta = \Omega_R/\Gamma_{\text{in}}$ as derived in section 5.1.1 and shown as function of the detuning Δ of the light from the D1 resonance in Fig. 5.3. The two minima correspond to the coupling light on resonance with the D1- and D2-transition respectively, where the scattering rate is maximized. Moving away from the resonances, the scattering rate decreases faster than the coupling strength, so β is growing. At $\Delta \approx \pm 4A_f$, the ratio is saturated. In between the two resonances, at our chosen wavelength of $\lambda_R = 768.9$ nm implying $\Delta = A_f/2$, β has a global maximum. Therefore this choice is extremely beneficial for minimizing loss due to inelastic photon scattering from the Raman beams.

The second advantage concerns the scalar light shifts introduced by the Raman light. At the particular wavelength of $\lambda_R = 768.9$ nm, the so called "tuneout" wavelength, the scalar light shifts from the D1 and D2 transition cancel out exactly.

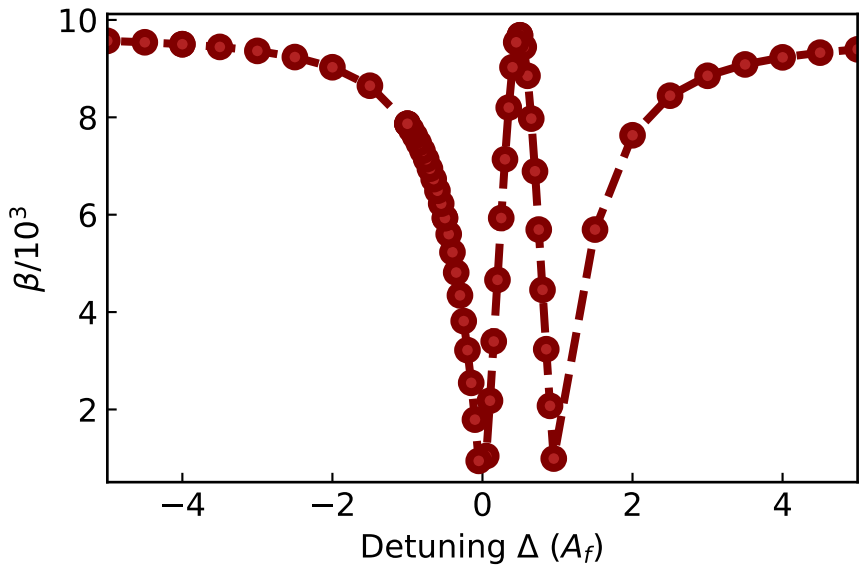

Figure 5.3: Numerical calculation of the ratio $\beta = \Omega_R/\Gamma_{\text{in}}$ for ^{39}K as function of the detuning Δ from the D1-transition at magnetic field of $B = 397$ G. The detuning Δ is given in units of the fine-structure splitting A_f.

Away from this wavelength, these shifts would alter the energy levels and thus affect the trapping potential, which is highly undesirable.

Frequency difference of Raman beams

We use eq. (5.4) to calculate the energies of the coupled states $|\downarrow\rangle, |\uparrow\rangle$ at our chosen magnetic field strength. For ^{41}K at $B = 338$ G, the energy difference is $\Delta E/h = 65.78$ MHz, whereas for ^{39}K at $B = 397$ G it is $\Delta E/h = 98.63$ MHz. Accordingly, we choose the frequencies of the Raman beams such that their frequency difference Δf fulfils $h\Delta f = \Delta + \delta_0$ for a desired two-photon detuning. Concretely, we set the two Raman frequencies to $\omega_1/2\pi = (c/\lambda_R) + 118.78$ MHz and $\omega_2/2\pi = (c/\lambda_R) + 53$ MHz for ^{41}K and to $\omega_1/2\pi = (c/\lambda_R) + 217.63$ MHz and $\omega_2/2\pi = (c/\lambda_R) + 118$ MHz for ^{39}K, respectively.

Polarization of Raman light

As depicted in the left panel of Fig. 3.1, the Raman beams have linear orthogonal polarization along $\hat{e}_y$ and $\hat{e}_z$. The linear polarization along $\hat{e}_y$ can be decomposed in a superposition between circular σ_+ and σ_- light. Thus we effectively drive transitions with π and σ_+ light and π and σ_- light, which can couple two spin states which differ by $\Delta m_J = \pm 1$. Therefore the two-photon Rabi frequency Ω_R given by eq. (5.7)-(5.10) is non-zero.

5.2 Raman setup

We have the following main requirements for the Raman setup: first, the optical alignment of the counter-propagating laser beams on the atomic cloud. Second, the frequency difference between the two beams is adjustable in a wider range so that we can realize the Raman coupling for different magnetic fields for both isotopes, ^{41}K and ^{39}K. Third, the frequency difference should be adjustable in a smaller range of ~ 500 kHz within milliseconds, corresponding to control over the detuning δ_0 during the experimental sequence. Last but not least, we also need temporal control in the microsecond range and an active stabilization over the intensity of the two beams, as we want to implement pulses as well as ramps of the coupling strength within one experimental cycle. The optical setup consists out of two parts:

1. The first part where two laser beams with the chosen wavelength, sufficient power and adjustable frequency difference between them is produced, and which allows for temporal control of the light. Special care was taken to suppress unwanted frequency components in the laser light, such that the atom loss due to photon scattering is optimized. This part of the setup is located on our "laser table" and is shown schematically in Fig. 5.4.

2. The laser light is send via optical fibers to the second part on the "experimental table", where the two beams are aligned on the atoms in the vacuum chamber. This part of the setup is sketched in Fig. 5.5.

The first part of the Raman setup was originally build up by master student Manon Ballu and former PhD student Dr. Julio Sanz. We use a commercial diode laser [1] to provide light at the tune-out wavelength $\lambda_R = 768.97$ nm, in the middle between the $D1$ and $D2$ resonance, which minimizes the inelastic photon scattering (see section 5.1.2). The laser is free running, during months of operation the drift in its wavelength typically remains below 0.1 nm. The laser light with a power of ~ 20 mW at the output of the optical fiber connected to its fiber dock, gets amplified with a homebuilt tapered amplifier[2] (TA). Following the TA, an optical isolator [3] prevents back-reflections after which we obtain a laser power of ~ 1.2 W. The TA not only emits light at the injection frequency, because of the broad gain curve (between $730 - 800$ nm), it also amplifies its spontaneous emission, so the light after the TA has an increased frequency background. Therefore, filtering the light after the TA and in particular diminishing the contributions of the D1 and D2 resonances is crucial to prevent excessive atom loss. In our final setup, the frequency filtering is performed by a combination of three distinct commercial interference filters[4]. The range of reflectance of the filters depends on the precise angle of incidence of the light. Hence, they are placed in homebuilt rotating mounts and aligned for minimal transmission for the laser light when tuned to the $D1$ and $D2$ resonance and maximal transmission for light at the Raman wavelength. After the filtering stage, the laser beam is split in two different paths. In each path, the frequency of the light is controlled with an acoustic-optical modulator (AOM) to produce the required frequency difference between the beams for the Raman coupling. Moreover, the AOMs also allow for temporal control. For the experiments with the isotope ^{41}K, we use AOMs[5] with centre frequencies at 110 and 60 MHz, respectively. This allows us to obtain a frequency difference of 65.78 MHz, matching the energy splitting between $|\downarrow\rangle$ and $|\uparrow\rangle$ at $B = 338$ G (see section 5.1.2). In order to be able to switch fast to a setup for Raman coupling in ^{39}K, we have built an additional path, with an AOM[6] at 200 MHz. In this way, we can use the 110 MHz and 200 MHz AOMs to match the energy splitting of 98.63 MHz between the $|\downarrow\rangle$ and $|\uparrow\rangle$ states in ^{39}K at $B = 397$ G. The two AOMs are controlled with two independent commercial frequency sources: a programmable

[1] Toptica, DL pro 780nm
[2] Eagleyard: EYP-TPA-0765-01500-3006-CMT03-0000
[3] Thorlabs, IOT-5-780-VLP
[4] LaserOptik: IF780/6deg, Semrock: LL01-780-12.5, Semrock: SP01-785RU-2.5
[5] Intraaction: ATM-1101A2, ATM601A2
[6] Intraaction: ATM-2001A2

frequency generator[7] and an FPGA based frequency generator[8].
After passing through the AOMs, the laser beams are coupled into independent polarization maintaining single-mode fibers[9],and sent to the second part of the setup, to our experimental table.

The purpose of this part is the alignment of the two different Raman beams on the atoms, counter-propagating along the x-direction, which coincides with our waveguide trap (see section 4.1). A simplified schematics of the setup is depicted in Fig. 5.5. The two fibers run to the two different sides of the vacuum chamber. The following beam paths are strongly constrained by the existing optics around the vacuum chamber. Moreover, they are partially overlapped with the infrared laser beam forming the waveguide potential along $\hat{e}_x$. This is achieved with two dichroic mirrors directly placed before and after the viewport windows of the vacuum chamber. The Raman beams also partially overlap with one of our ToF imaging paths. Therefore, one mirror along each Raman path is placed on a mount that can be manually flipped out of the imaging beam trajectory. From

[7] Rhode Schwarz: SMC100A 9kHz-1.1GHz
[8] Signadyne: SD-AOU-H3444-PXIe-1G
[9] Thorlabs: P3-630PM-FC-10

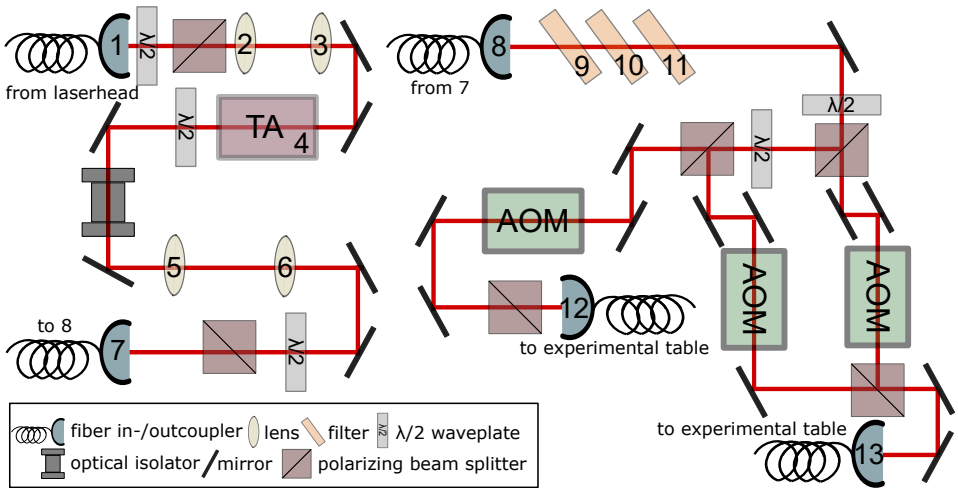

Figure 5.4: Sketch of the Raman setup on the laser table. The optical components are (1): 60FC-4-A6.2S-02 (Schäffter+Kirchhoff), (2): f=30 mm, (3): f=100 mm, (4): tapered amplifier, see footnote 2, (5): f=150 mm, (6): f=-50 mm, (7): C110-TMD-B-f=6.24 (Thorlabs), (8): 60FC-4.5S-02 (Schäffter+Kirchhoff), (9), (10), (11): see footnote 4, (12), (13), (14): see footnotes 5, 6. All mirrors are the BB1-E03 model from Thorlabs, all cubes used for power splitting the model PBS0649-650-850nm from Foctek, all cubes for polarization cleaning the model G335525000 from Qioptiq, all waveplates zero-order 768.4 nm waveplates from Foctek.

the fiber outcoupler[10] on both sides of the vacuum chamber, the light is picked up on a photodiode with a beamsampler [11] for an intensity stabilization. Afterwards, the two Raman beams are focussed on the atoms with a lens[12] of focal length $f = 300$ mm, which results in an $1/e^2$ diameter of $(150, 162)$ µm on the atoms. Compared to the atomic cloud size, which is typically ≤ 10 µm of diameter in the plane transversal to the Raman propagation direction, this is sufficiently large to consider the Raman intensity as uniform on the atomic's position. The polarization of the two beams is set by $\lambda/2$ plates to linear horizontal (along $\hat{e}_y$) and linear vertical (along $\hat{e}_z$) polarization before the chamber respectively.

5.3 Optical alignment

A good alignment of the Raman beams relative to each other and onto the atoms along the waveguide direction is quite challenging to achieve. In order to optimize it, we have established the following routine:

- As a starting point, the two beams are aligned on the dipole trap beam along the x-direction (waveguide potential).
- The position of the atoms is recorded in a camera with an imaging beam along the x-axis.
- We optimize the alignment of one of the Raman beams along the waveguide by monitoring its position on the camera relative to that of the atomic cloud.

[10] Schäffter+Kirchhoff: 60FC-4-A6.2S-02
[11] Thorlabs, BSN11 and Thorlabs, BSF10-B
[12] Thorlabs: LA4579-B-f=300mm

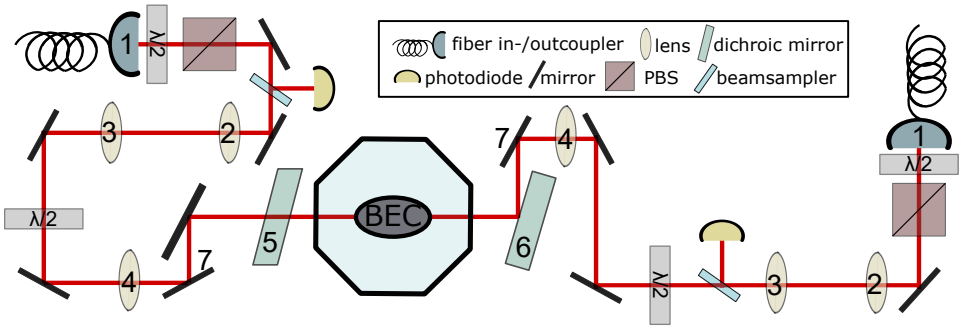

Figure 5.5: Simplified schematics of the Raman setup on the experimental table. The optical components are (1): 60FC-4-A6.2S-02 (Schäffter+Kirhhoff), (2) f=-100 mm, (3): f=150 mm, (4): f=300 mm, (5): DMSP1000L (Thorlabs), (6): DMLP950L (Thorlabs), (7) flipping mirror.

- Afterwards, the other Raman beam is overlapped with the first one. Fine-tuning is achieved by coupling this beam back into the fiber of the first Raman beam.

- In the last step, the alignment is improved with the atomic signal. The orientation of the last mirrors before the chamber is tuned on both sides in an iterative way to improve the atomic transfer during a pulse with the two Raman beams on resonance. In order to prevent confusion, one should use a time shorter than the expected π-pulse time. Otherwise a larger coupling strength could imply a smaller transfer at a fixed pulse period.

Each time the mirrors on the flipping mounts are moved in and out the path, the Raman alignment has to be checked.

5.4 Characterization of the Raman setup

As detailed in chapter 3, the effect of the Raman coupling can be understood in terms of a dressing of the bare coupling states $|\uparrow\rangle$ and $|\downarrow\rangle$ into a new ground state with modified energy dispersion. The new dispersion relation strongly depends on the coupling field parameter Ω_R and δ_0 and therefore, a precise knowledge of these is needed in our experiments. Moreover, the lifetime τ, set by the Raman inelastic photon scattering rate and therefore also dependent on the Raman light settings, is also crucial to our experiment as it limits the duration of all our measurements. In this section we describe how Ω_R, δ_0 are controlled and calibrated and τ is measured in the experiment.

Raman detuning

We control the relative detuning of the two counter-propagating Raman beams by means of single pass AOMs placed along the path of each beam on the 'laser table'(see section 5.2). One of the two AOMs is driven by the programmable rf source and sets the frequency of the respective Raman beam to $\omega_1/2\pi = 118.78$ or $\omega_1/2\pi = 217.36$ MHz for ^{41}K or ^{39}K, respectively. The second AOM, controlled by the FPGA-based frequency source, has a centre frequency of 60 MHz (110 MHz) for ^{41}K (^{39}K) and its frequency ω_2 is adjusted to match the desired detuning of the two-photon transition. We checked that the frequency output of the generators is precise within $\leq$ 100 Hz with a spectrum analyzer clocked externally with 10 MHz. For a fine adjustment of the two-photon detuning, we fix the frequencies of the Raman beams to the theoretically expected ones for a chosen magnetic field B_0 and tune the external magnetic field, controlled by the current in the coils, to this precise value. We use a transition between two internal states to find B_0 by optimizing the transfer probability from one hyperfine state to another *via* an rf

π-pulse with the theoretically expected frequency at B_0.

The magnetic field calibration is specific for each isotope and mainly relevant for ^{39}K. When working with ^{41}K, we cannot use the transition between the Raman states $|\downarrow\rangle, |\uparrow\rangle$ as they are magnetic insensitive as outlined above. Therefore we use the transition between the lowest states of the ground-state manifold $|\mathrm{aux}\rangle$ and $|\downarrow\rangle$ with a magnetic sensitivity of $\partial\delta_0/\partial B \approx 20$ Hz/mG. Instead, in ^{39}K we can use the $|\downarrow\rangle$ to $|\uparrow\rangle$ transition which has a magnetic sensitivity of $\partial\delta_0/\partial B \approx 50$ Hz/mG. In contrast to ^{41}K, we cannot perform the calibration with a condensate as the different interactions in the two hyperfine states introduce differential mean field shifts and therefore an effective detuning in the order of kHz. Therefore, the magnetic field calibration is obtained from an atomic cloud slightly above the condensation temperature.

A typical measurement of the transfer is shown in Fig. 5.6 for the case of ^{41}K. We mostly use an rf-coupling strength of $\Omega_{RF}/2\pi \sim 2$ kHz, corresponding to a π-pulse of duration ~ 220 µs. As function of the magnetic field we obtain the transfer probability $N_{\mathrm{aux}}/(N_\downarrow + N_{\mathrm{aux}})$ after the rf-pulse by extracting the atom numbers $N_{\mathrm{aux}}, N_\downarrow$ *via* ToF imaging and a Stern Gerlach pulse. The uncertainty of the magnetic field strength B_0 yielding the maximum transfer is ≤ 10 mG from fitting uncertainties, which translates into an uncertainty of ~ 200 Hz and ~ 500 Hz in detuning for ^{41}K and ^{39}K, respectively. We have considered to decrease the rf-coupling strength so the peak gets narrower, but the measurement gets more noisy and the accuracy of determining the centre of the peak does not necessarily improve.

Raman coupling strength

The strength of the Raman coupling is given by the intensity or optical power in the beams (see eq. (5.7)), which we control and stabilize with an active feedback loop. The Raman coupling strength is calibrated with the atomic signal. When the Raman beams are turned on abruptly for a time period Δt, i.e. the band-structure as described in chapter 3 is induced suddenly, the atoms undergo Rabi flopping dynamics between the bare states. The polarization P oscillates between -1 and 1 and the probability to find an atom in the upper state $|\uparrow\rangle$ is given by

$$P_\uparrow = \frac{\Omega_R^2}{\tilde{\Omega}_R^2} \sin^2\left(\frac{1}{2}\tilde{\Omega}_R t\right), \tag{5.18}$$

where we have assumed $P = -1$ initially, so all atoms are in state $|\downarrow\rangle$. In accordance with its physical meaning, $P_\uparrow$ runs from 0 to 1 as the time is varied, which is in contrast to the polarization for which $P \in [-1, 1]$ holds. We introduce such Rabi oscillations between $|\uparrow\rangle$ and $|\downarrow\rangle$ with a resonant Raman pulse with variable length.

The Raman pulse is on resonance if the condition $\Delta\omega = \omega_0 + \hbar^2(2k_R)^2/2m$ is fulfilled. The second contribution accounts for the additional energy separation due to the momentum transfer. We then determine $P_\uparrow$ by measuring the atom numbers $N_\downarrow, N_\uparrow$ of the two spin states with our spin resolvable absorption imaging and calculating $P_\uparrow = N_\uparrow/(N_\uparrow + N_\downarrow)$.

An example of a measured Rabi oscillation is shown in Fig. 5.6 up to a pulse duration of 750 µs. Within this timescale only minor damping is observed, and we fit a squared sine function to the data to extract the Rabi frequency. Usually we realize the optical pulse in the order of µs with a disabled intensity control, as the PID controller cannot react properly in this timescale. An alternative procedure is to keep the Raman beams at a fixed power for a few milliseconds and to change the detuning from far off resonance (e.g. $\delta_0/2\pi = -30.4\ E_R/h$) to resonance for the required pulse length. We do so by abruptly changing the rf input of the AOM between two distinct frequency sources at different frequencies with an rf switch. In this way, we are able to stabilize the power during the pulse with our active feedback loop. Both methods result in a very similar error in the coupling strength calibration, thus both do not suffer from additional uncertainty due to power fluctuations in the Raman beams. The error of the measured Ω_R, extracted from the covariances of the fit is in the order of 3%. We estimated numerically that the additional error in ^{39}K due to the damping caused by the mean field detuning is $\leq 3\%$.

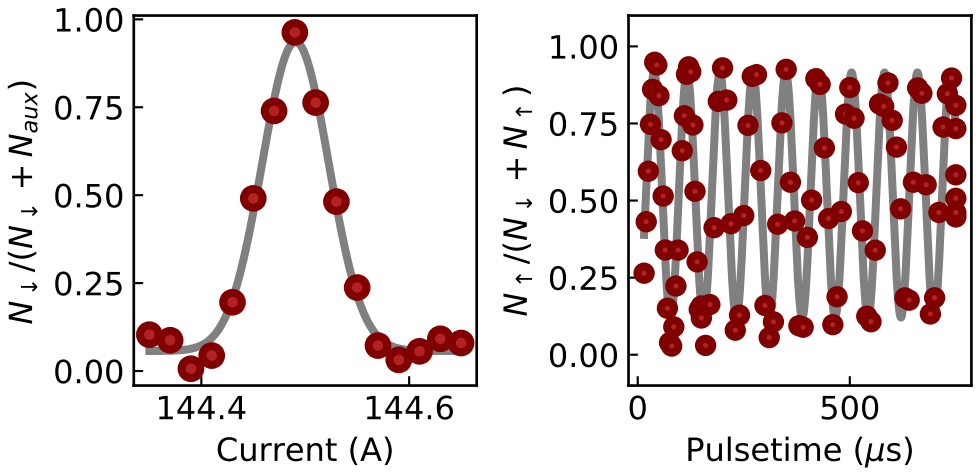

Figure 5.6: Calibration of coupling field parameter. **Left:** Typical transfer probability between $|\mathrm{aux}\rangle$ and $|\downarrow\rangle$ in ^{41}K with an RF π-pulse. The signal is used for a magnetic field/two-photon detuning calibration. **Right:** Rabi oscillations between $|\downarrow\rangle$ and $|\uparrow\rangle$ after a Raman π-pulse. The signal is used for a Raman coupling strength calibration.

Atomic lifetime under the presence of Raman coupling

We measured the atom loss of the Raman-dressed ^{41}K and ^{39}K Bose-Einstein condensate for a coupling strength of $\Omega_R/2\pi = 4.5\ E_R/h$. During these measurements we had a two-photon detuning of $\delta_0/2\pi = -30.4\ E_R/h$, so we only measure the effect from single particle photon scattering. The results are shown in Fig. 5.7. We fitted an exponential decay to the data and extracted an $1/\mathrm{e}$ value of $\tau = (39.2 \pm 1.9)$ ms for ^{41}K and $\tau = (38.7 \pm 1.6)$ ms for ^{39}K.

Our theoretical computation of the ratio $\beta = \Omega_R/\Gamma_{\mathrm{in}}$ (presented in section 5.1.1) predicts for $\Delta = -A_f/2$ a ratio of $\beta = 9.7 \times 10^3$ for ^{41}K at $B = 338$ G and $\beta = 9.6 \times 10^3$ for ^{39}K at 397 G. For $\Omega_R/2\pi = 4.5\ E_R/h$ the expected lifetime is $\tau = 1/\Gamma_{\mathrm{in}} \approx 41.8$ ms for both isotopes at these different magnetic field values, where we have assumed the energy transfer of the Raman beams leads to the immediate loss of the atom. Note that the computation gives the lifetime only accounting for single particle photon scattering as we also measure experimentally in Fig. 5.7. The result of the calculation is in very good agreement with the theoretical prediction. We conclude that the experimentally measured atomic lifetime is close to the ideally expected value and our filtering procedure after the TA is sufficient.

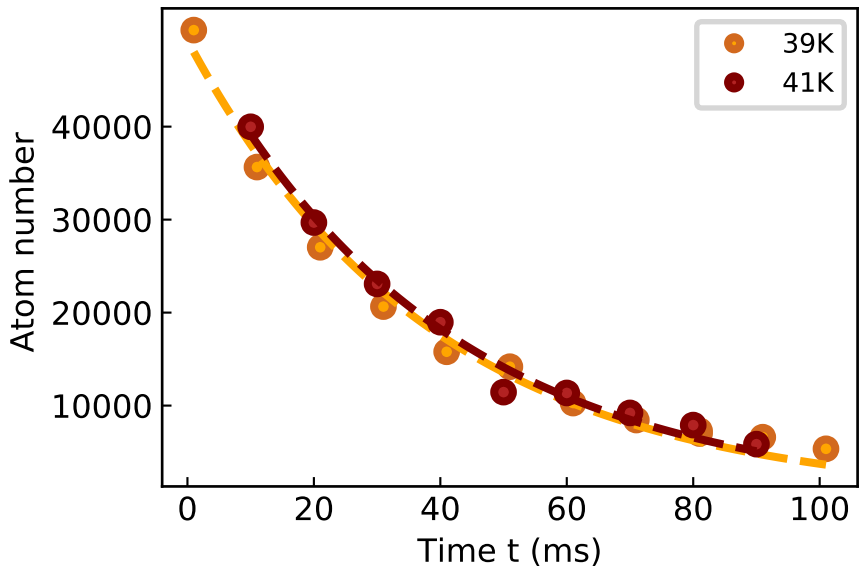

Figure 5.7: Measured atomic lifetime in the presence of Raman coupling. The graph shows the atom number after a time period t under the presence of the two Raman beams with $\Omega_R/2\pi = 4.5\ E_R/h$ and $\delta_0/2\pi = -30.4\ E_R/h$. Red data points correspond to ^{41}K at $B = 338$ G, orange data points to ^{39}K at $B = 397$ G. The dashed lines are an exponential fit with $(1/\mathrm{e})$ values of $\tau = (39.2 \pm 1.9)$ ms and $\tau = (38.7 \pm 1.6)$ ms for ^{41}K and ^{39}K, respectively.

5.5 Quasi- and mechanical momentum in the laboratory frame

In chapter 3, we have seen that the characteristics of the Raman coupling are a function of the quasi-momentum k_x, as any momentum introduces an effective detuning $\tilde{\delta} = \delta_0 - 4k_x$, which affects the atom's energy, polarization, its effective mass and the experienced effective gauge potential.

Assuming that the Raman dressing is switched on adiabatically, the group velocity of the cloud in the quasi-momentum frame coincides with the momentum in the minimum of the dispersion: $k_x = k_{\text{min}}$. However, as the process is never perfectly adiabatic and the atoms in the experiment also have a mechanical momentum k_{mech} on top, the total quasi-momentum is $k_x = k_{\text{min}} + k_{\text{mech}}$. Here below we explain how the momentum k_{min} and mechanical momentum k_{mech} can be directly seen in the laboratory frame.

In order to determine the quasi-momentum, we switch off abruptly the Raman beams and measure the momentum distribution with ToF imaging. In this way the Raman-dressed state is projected into the two bare states and k_x can directly be extracted from the difference Δx in the position of atoms which were and which were not coupled by the Raman beams: $k_x = \Delta x / t_{\text{ToF}}$. In the left panel of Fig. 5.8 we see an exemplary image obtained after $t_{\text{ToF}} = 21$ ms and Stern Gerlach separation of the spin states, for $\Omega_R/2\pi = 4\ E_R/h$ and $\delta_{0,\text{fin}}/2\pi = -0.37\ E_R/h$. The bare states $|\downarrow\rangle$, $|\uparrow\rangle$ are separated vertically. The dashed line marks the reference position of atoms in state $|\downarrow\rangle$ without Raman coupling. In order to understand the horizontal shift Δx observed after time of flight, one has to consider the physical momenta of the bare states. These are not k_x but $k_{\text{phys}} = k_x \pm k_R$, respectively, with $k_x = k_{\text{min}} + k_{\text{mech}}$. Because of the momentum transfer from the photons of the Raman beams to the atoms, the two components are always separated by $2k_R$. In particular, in our system, the $|\uparrow\rangle$ component is on the positive side (here left) with respect to $|\downarrow\rangle$, which is set by the propagation direction of the Raman beam with higher/lower frequency. If the atoms are transferred from $|\downarrow\rangle$ to $|\uparrow\rangle$ with a π-pulse, they will appear on the left at a distance $\Delta_\uparrow x = 2K_R/t_{\text{ToF}}$ from the rest position of the atoms in $|\downarrow\rangle$, if zero mechanical momentum $k_{\text{mech}} = 0$ is assumed. If instead the dressed state $|-\rangle$ is prepared by e.g. a detuning sweep from $|\downarrow\rangle$ towards $|\uparrow\rangle$, both spins composing $|-\rangle$ will be found again separated by $2K_R/t_{\text{ToF}}$, but commonly shifted by $k_{\text{min}}/t_{\text{ToF}}$ to the right, because $k_{\text{min}} < 0$. Therefore, $\Delta_\uparrow x = +2k_R/t_{\text{ToF}} - |k_{\text{min}}|/t_{\text{ToF}}$ for the shift of atoms in $|\uparrow\rangle$ and $\Delta_\downarrow x = -|k_{\text{min}}|/t_{\text{ToF}}$ for the atoms in state $|\downarrow\rangle$, respectively. The shift $k_{\text{min}}/t_{\text{ToF}}$ unveils the synthetic static vector potential A_0 present in the system. This is summarized in table 5.1, which gives the values of k_{min} and k_{phys} for the three limiting cases of the detuning.

	$\delta_{0,fin} \ll 0$	$\delta_{0,fin} = 0$	$\delta_{0,fin} \gg 0$
k_{min}	$+k_R$	0	$-k_R$
$k_{\text{phys}} - k_{\text{mech}}$	0 for $\|\downarrow\rangle$, $+2k_R$ for $\|\uparrow\rangle$	$-k_R$ for $\|\downarrow\rangle$, $+k_R$ for $\|\uparrow\rangle$	$-2k_R$ for $\|\downarrow\rangle$, 0 for $\|\uparrow\rangle$
k_{mech}	$1 \times (0 + k_{\text{mech}}) +$ $0 \times (2k_R + k_{\text{mech}})$	$0.5 \times (-k_R + k_{\text{mech}}) +$ $0.5 \times (k_R + k_{\text{mech}})$	$0 \times (-2k_R + k_{\text{mech}}) +$ $1 \times (0 + k_{\text{mech}})$

Table 5.1: Momenta of Raman-dressed atoms for three characteristic values of two-photon detuning. The detected momentum k_{phys} is $k_x - k_R$ for $|\downarrow\rangle$ and $k_x + k_R$ for $|\uparrow\rangle$ with $k_x = k_{\text{min}} + k_{\text{mech}}$. The mechanical momentum is the spin weighted sum of the momentum in the two bare states.

Fig. 5.8 shows the case of a finite negative detuning $\delta_0/2\pi = -0.37\, E_R/h$. Any discrepancy between the momenta extracted from the clouds positions and the expected k_{phys}, represents an additional k_{mech}, common to both spins. Practically, the contribution k_{mech} can be calculated over the spin weighted sum (see bottom line in Table 5.1):

$$k_{\text{mech}} = P_\uparrow k_{x,\uparrow} + (1 - P_\uparrow) k_{x,\downarrow}, \tag{5.19}$$

where $P_\uparrow = N_\uparrow/(N_\uparrow + N_\downarrow)$ is the probability to project the dressed state into $|\uparrow\rangle$ as previously introduced.

In our measurements we use two different methods to extract the quasi-momentum k_x from the condensate in the lower dressed state and to distinguish between k_{min} and k_{mech}. The first one is based on ToF images in combination with the centre of mass oscillation induced by the mechanical momentum in a dipole trap [101] and used to measure the synthetic static vector potential (see section 6.2 for more details). The second method relies on spin ejection spectroscopy [164] and is applied in the measurements on the modified free expansion dynamics caused by the effective mass or/and density-dependent vector potential (see section 6.3 and 7.3), where a precise knowledge of the generalized detuning $\tilde{\delta}$ is needed.

5.6 Preparation of atoms in the Raman-dressed band

In all our experiments we start with the condensate in $|\downarrow\rangle$ without Raman coupling. We then load the atoms in the Raman modified dispersion relation characterized by the final values $\Omega_{R,\text{fin}}, \delta_{0,\text{fin}}$. We aim to prepare the atoms with zero mechanical momentum, so the quasi-momentum is just given by the momentum in the minimum of the dispersion: $k_x = k_{\text{min}}$. However, this is challenging as any non-adiabatic preparation induces a mechanical momentum k_{mech} and we are limited in the time duration of the preparation by the atomic lifetime of ~ 39 ms.

The optimal preparation procedure we found for the isotope ^{39}K, consists out of the following steps:

1. We switch on the Raman beams at an initial two-photon detuning $\delta_0/2\pi$ below $= -0.46\, E_R/h$.

2. We ramp up the power of the Raman beams non-linearly to $\Omega_R/2\pi = 4\ E_R/h$ within time τ_1. The non-linear power ramp is of the form $\Omega_R(t) = 4\sqrt{(t/\tau_1)(2-(t/\tau_1))}$, which leads to a liner increase of the momentum in the minimum of the dispersion, $k_{\mathrm{min}} = \sqrt{1-(\Omega_R/4)^2}$ for $\Omega_R/2\pi < 4\, E_R/h$ and $\delta_0 = 0$.

3. We sweep the detuning linearly to its final value and simultaneously increase linearly the coupling strength to its final value in a time τ_2.

This preparation procedure is illustrated in Fig. 5.9. For the isotope ^{41}K we follow a similar scheme. Exact values and minor differences are peculiar to each measurement and detailed in the corresponding section.

The outlined steps ensure that we are above $\Omega_R/2\pi = 4\ E_R/h$ before sweeping the detuning δ_0 to values close to zero. This is necessary for the following reasons:

- The first reason resides in the phase diagram of the Raman-coupled condensate, which was calculated for ^{39}K by my colleague Craig Chisholm[172].

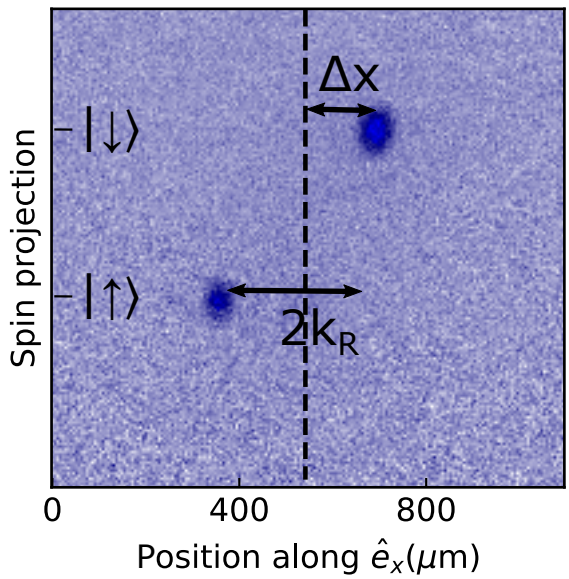

Figure 5.8: Example of an absorption image of the Raman-dressed condensate for $\Omega_R/2\pi = 4.5\, E_R/h$ and $\delta_0/2\pi = -0.37\ E_R/h$ obtained after time of flight of 21 ms. The dressed atoms get projected into the bare states $|\downarrow\rangle$,$|\uparrow\rangle$ and separated vertically during a Stern Gerlach pulse. The dashed line indicates the reference position of atoms in $|\downarrow\rangle$ without Raman coupling present. Δx is the shift due the quasi-momentum $k_x = k_{\mathrm{min}} + k_{\mathrm{mech}}$.

For coupling strengths above $4\,E_R/h$ the dispersion has a single minimum. In this thesis, we always want to prepare the system in this phase. For $\Omega_R < 4\,E_R/h$, the dispersion has two minima. If only one minimum is occupied the system is in the plane wave phase. For values of the detuning between $\delta_0/2\pi = (-0.4\text{-}0.1)\,E_R/h$, both minima are occupied and the system is in the "stripe phase"[132,161]. Whereas the transition between plane wave to single minimum phase is of second order, the stripe to single minimum phase transition is of first order[173] and thus has to be circumvented.

- The second reason concerns the adiabaticity of the preparation. For coupling strengths of $\Omega_R/2\pi \leq 4\ E_R/h$, the minima on the $k_x < 0$ and $k_x > 0$ sides do not connect smoothly around $\delta_0 = 0$ and the preparation cannot be adiabatic. Fig. 5.10 illustrates this circumstance for atoms prepared at a final $\Omega_R/2\pi \leq 4\ E_R/h$. The left panel shows the predicted energy in the minima of the dispersion at negative and positive momentum, respectively. For the example of final $\Omega_R/2\pi = 2.5\,E_R/h$ there is a discontinuity in the energy when sweeping the detuning across zero. In the right panel the mechanical momentum arising for different values of the final detuning and final $\Omega_R/2\pi = 4\ E_R/h$ is depicted. It was calculated with the spin-weighted average (see. (5.19)) from ToF images. In the regime of $\delta_0 \ll 0$, the mechanical momentum acquired by the dressed atoms is minor. It considerably increases for a final two-photon detuning $\delta_0/2\pi > -0.12\,E_R/h$, which we attribute to the flat dispersion at $\Omega_R/2\pi = 4\ E_R/h$.

In order to validate our preparation procedure, we usually perform the following tests:

- We measure the introduced mechanical momentum as function of the sweep rates. Any mechanical momentum of atoms trapped in a harmonic dipole trap leads to an oscillation of the atomic cloud's centre of mass position. We optimize the detuning and power ramps by minimizing the amplitude of this oscillation.

- We test the coherence of the prepared dressed state. Therefore we reverse our preparation ramps after a variable waiting time in the dressed band and undress the atoms. We observe the full population back in the initial state $|{\downarrow}\rangle$, so the state remains coherent.

5.7 Conclusion

In this chapter, we summarized experimental considerations concerning the implementation of Raman coupling in a Bose-Einstein condensate of ^{40}K and ^{39}K. We described the experimental setup and found theoretically suitable parameters such

that the two-photon uncertainty and the atomic loss caused by the inelastic photon

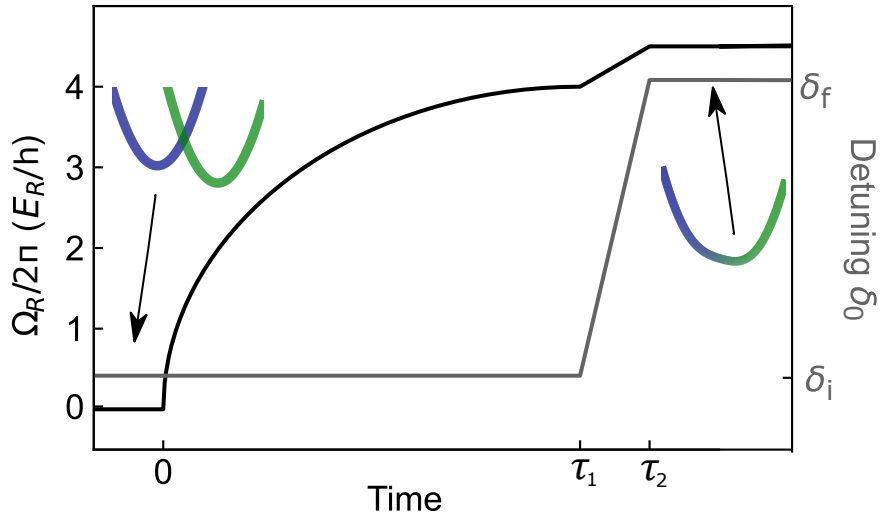

Figure 5.9: Illustration of the optimized preparation sequence to prepare atoms in the lower Raman-dressed band. δ_i (δ_f) denote the initial (final) two-photon detuning δ_0. These steps ensure the stripe phase in ^{39}K is not entered, the dispersion minima on the negative and positive k_x side connect smoothly while keeping the atom loss minimal.

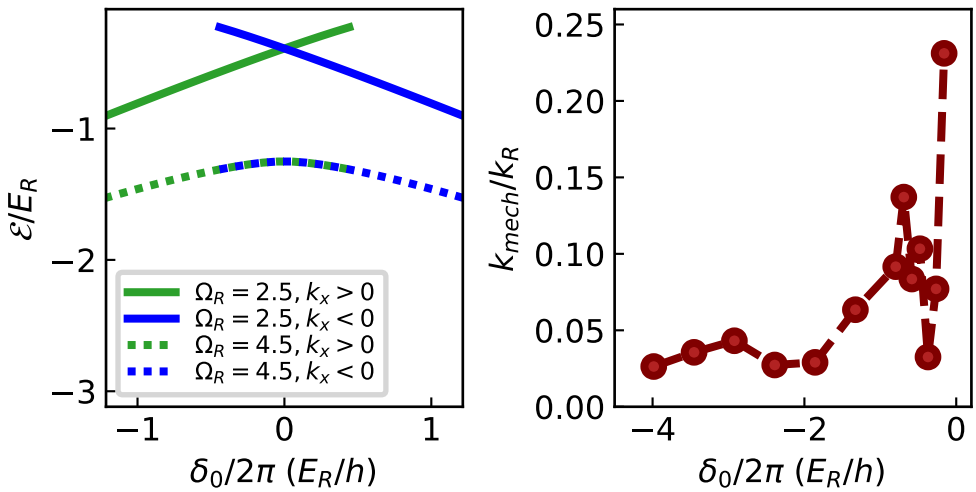

Figure 5.10: Non-adiabaticity of preparation. **Left:** The energy of the dispersion relation for k_{min} for a coupling strength below and above $4\,E_R/\hbar$ as function of the detuning. The minima in the sides $k_x < 0$ and $k_x > 0$ only connect smoothly for $\Omega_R/2\pi > 4\ E_R/h$. **Right:** Mechanical momentum of the dressed state at $\Omega_R/2\pi = 4\ E_R/h$ as function of the final detuning. The mechanical momentum was extracted via the spin weighted average, see eq. (5.19).

scattering is minimized. In particular, we found for ^{39}K a magnetic field setting at values around 400 G which limits the fluctuation in the two-photon detuning to approx. 750 Hz and also allows us to tune the interactions of the $|\downarrow\rangle$ state in a broad range of approx. $225\,a_0$. At this given magnetic field, we set the wavelength of the Raman light to the "tune-out" wavelength in the middle between D1 and D2 line which results in a lifetime of $\lesssim 40$ ms at the Raman coupling strengths $\Omega_R/2\pi \geq 4\,E_R/h$ we employ. With these setting we are able to prepare atoms in the Raman-dressed dispersion with tolerable mechanical momentum. In conclusion, a BEC of ^{39}K seems a suitable platform to explore the combination of tunable interactions and Raman coupling and hence to simulate the chiral BF theory.

As we have seen, the lifetime increases for heavier atomic species. Therefore a heavier atom which also offers a flexible interaction control as ^{39}K would be an exciting prospect. For example, ^{133}Cs offers many magnetic Feshbach resonances[174–178] and hence might be a promising candidate for studies where a higher Raman coupling strength is desired. However, due to its negative and very large background scattering length, experiments will only be possible at the overlap of several Feshbach resonances and finding an appropriate magnetic field region could be more challenging than for potassium.

6 Single particle effects in a Raman-coupled BEC

After the technical characterization of our Raman setup, we now turn to the study of Raman-coupled condensates. In this chapter we investigate its induced effects on the condensate on the single particle level.
We directly measure the energy band of the lowest dressed state, the synthetic vector potential experienced by the atoms and investigate the change in the free expansion dynamics of the condensate due to its modified effective mass.

In this chapter we investigate Raman-coupled BECs on the single particle level as a preparatory step before studying Raman-coupled BECs with interactions in chapter 7. As we detailed in chapter 3, Raman coupling modifies the dispersion relation of the coupled atoms. The effect of Raman coupling on the atoms has already been studied extensively in different groups[98–102,107,152–157,159–166]. We here follow some of these measurements and investigate the modified dispersion, the effective vector potential and the effect of the modified mass.

Most measurements in this chapter are performed with the isotope ^{41}K for which we achieve a better stability in the two-photon detuning (see chapter 5) and where we cannot confuse single-particle and interaction effects. However, the measurement of the synthetic vector potential *via* the quasi-momentum for which the interaction effects are below our experimental resolution, is carried out with the isotope ^{39}K. In this chapter, all Raman parameters and momenta are expressed in units of the Raman recoil energy E_R and momentum k_R respectively. In contrast to chapter 3, we do not set E_R,k_R and $\hbar$ to one. Other quantities are given in SI units.

All the experimental work presented in this chapter was obtained in close collaboration with my colleagues Craig Chisholm and Dr. Cesar Cabrera.

6.1 Spin injection spectroscopy of the lowest Raman-dressed band

As described in chapter 3, the modified dispersion relation is the key feature of the Raman-dressed BEC. We can directly measure the dispersion relation by spin injection spectroscopy. This technique was established by the group of Prof. Zwierlein in Ref. 164, where it was used to measure the lower Raman-dressed band of a Fermi gas in the low coupling regime $\Omega_R/2\pi < 4\ E_R/h$. Here we adapt this technique to measure the dispersion relation of the lower dressed band of the Raman-dressed ^{41}K Bose-Einstein condensate.

Spin injection spectroscopy is based on directly probing the energy of the transition between a bare state and the Raman-dressed band. We start with atoms in the uncoupled auxiliary state $|\text{aux}\rangle \equiv |1\rangle\,|F = 1, m_F = 1\rangle$ and inject atoms into the unoccupied Raman-dressed dispersion *via* a radio-frequency pulse with variable frequency. Afterwards, we quantify the fraction of atoms transferred to the $|\downarrow\rangle \equiv |2\rangle$ or $|\uparrow\rangle \equiv |3\rangle$ state by spin resolved absorption imaging after time of flight. From the frequency of the rf-pulse with the highest injection probability we can infer the energy of the Raman-dressed band. This concept is illustrated in Fig. 6.1. More precisely, the resonant transition frequency between the lowest dressed band and the $|\text{aux}\rangle$ state with energy E_{aux} is given by $f_{-,\text{aux}}(k_x, \delta_0, \Omega_R) =$

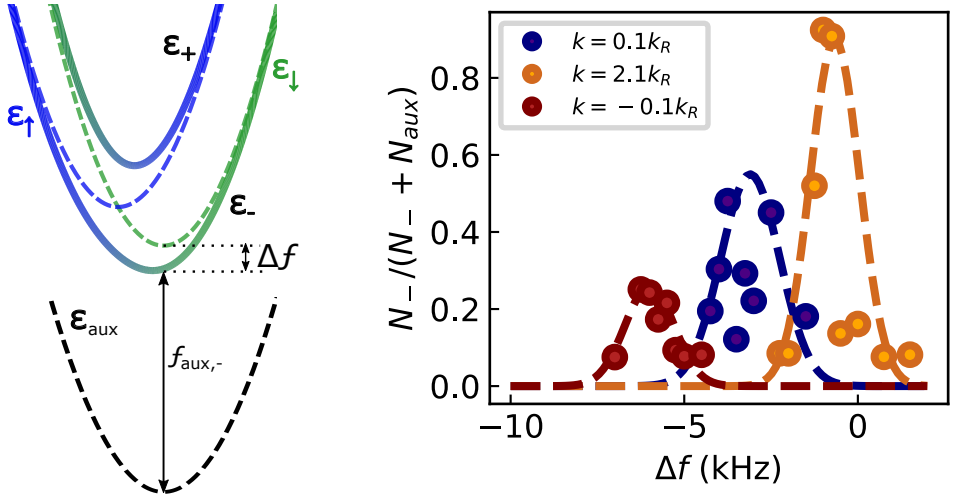

Figure 6.1: Spin injection spectroscopy as established in Ref. 164. **Left:** Schematics of the dispersion relations of the $|\text{aux}\rangle$ state (dashed line), $|\downarrow\rangle$, $|\uparrow\rangle$ states (dashed lines) and Raman-dressed states $|-\rangle, |+\rangle$. We experimentally measure the frequency $f_{\text{aux},-}$ and from the difference Δf to the frequency between the bare states $|\text{aux}\rangle$ and $|\downarrow\rangle$, we can reconstruct the energy of the Raman-dressed state $|-\rangle$. **Right:** Transfer probability from state $|\text{aux}\rangle$ to the dressed state $|-\rangle$ as function of frequency difference Δf to the bare transition frequency $f_{\text{aux},\downarrow}$ for a selection of quasi-momenta prepared by Bragg diffraction (see Fig. 6.2).

$(\mathcal{E}_-(k_x, \delta_0, \Omega_R) - \mathcal{E}_{\text{aux}}(k_x))/h$, with $\mathcal{E}_-(k_x, \delta_0, \Omega_R) = E_R(k_x^2 + 1) \pm \hbar\tilde{\Omega}_R/2$ as derived in section 3.2.1 for the non-interacting case. As one can see from Fig. 6.1, the dispersion of the auxiliary state can be expressed as $\mathcal{E}_{\text{aux}}(k_x) = \mathcal{E}_\downarrow(k_x) - hf_{\text{aux},\downarrow}$ where $f_{\text{aux},\downarrow}$ is the frequency of the transition between $|\text{aux}\rangle$ and $|\downarrow\rangle$ in the absence of Raman coupling and which can be calculated with eq. (5.4). The dispersion of the bare $|\downarrow\rangle$ state is a parabolic free particle dispersion and in the quasi-momentum frame is given by $\mathcal{E}_\downarrow = E_R(k_x - 1)^2 - \hbar\delta_0/2$. Therefore we find

$$hf_{-,\text{aux}}(k_x, \delta_0, \Omega_R) = \mathcal{E}_-(k_x, \delta_0, \Omega_R) - (\mathcal{E}_\downarrow - hf_{\text{aux},\downarrow}) \tag{6.1}$$

for the frequency difference between the $|\text{aux}\rangle$ to $|-\rangle$ and the $|\text{aux}\rangle$ to the bare $|\downarrow\rangle$ state

$$\Delta f(k_x, \delta_0, \Omega_R) = f_{-,\text{aux}}(k_x, \delta_0, \Omega_R) - f_{\text{aux},\downarrow} = -\frac{\tilde{\Omega}_R + \tilde{\delta}}{4\pi}. \tag{6.2}$$

The momentum dependence of Δf is illustrated in the right panel of Fig. 6.1, where we show the measured shift in the transfer frequency for three exemplary momenta. For quasi-momenta k_x in the range of $-0.1\ k_R$ to $2.1\ k_R$, the resonant frequency $f_{-,\text{aux}}$ is changing by $\Delta f = 8$ kHz. After the experimental determination of $\Delta f(k, \delta_0, \Omega_R)$, we can infer the energy of the dressed band with eq. (6.1).

In order to reconstruct the full band we need $\Delta f(k_x, \delta_0, \Omega_R)$ for all k_x of interest.

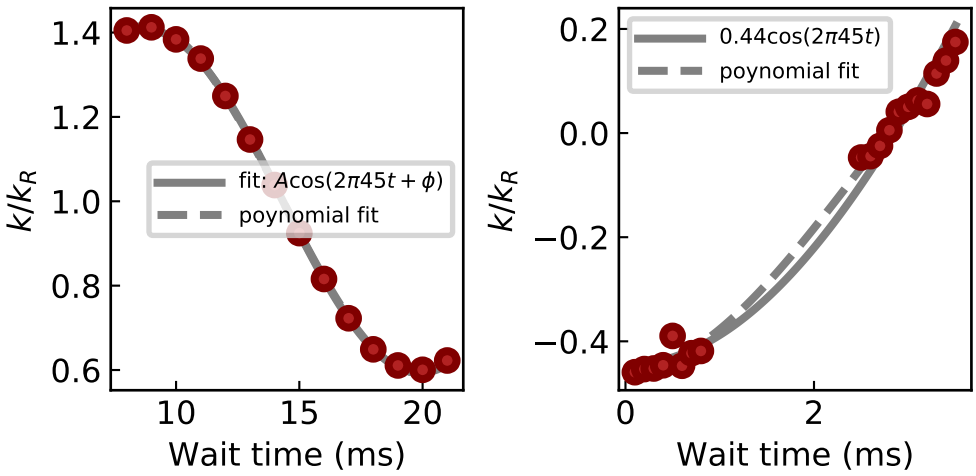

Figure 6.2: Left: Momentum of the condensate in state $|\downarrow\rangle$ after applying a magnetic gradient in x-direction as function of the waiting time in an harmonic dipole trap. **Right:** Momentum of the condensate in $|\downarrow\rangle$ after Raman-Nath diffraction on an optical lattice as function of the waiting time in a harmonic dipole trap. The solid lines are the theoretical predictions assuming an oscillation in a trap with $\omega_x/2\pi = 45$ Hz. In the case of the magnetic kick we perform a fit with $A\cos(2\pi f_x + \phi)$ and find $A = 0.6\ k_R$ and $\phi = 0.63$. The dashed lines are fits of a third order polynomial.

In the pioneering work of Ref. [164], the experiments were performed with a Fermi gas and hence all momenta could be probed with one single rf-pulse. In the case of a BEC only a narrow range of momentum states are occupied. Therefore, we have to prepare the condensate at different momenta and repeat the measurement of $\Delta f(k_x, \delta_0, \Omega_R)$ at each momentum to obtain the full energy-momentum relation.

We start with a ^{41}K BEC in the auxiliary state in the crossed dipole trap formed by our waveguide along $\hat{e}_x$ and the additional beam along $(\hat{e}_x + \hat{e}_y)/\sqrt{(2)}$ (see section 4.1) with trapping frequency of $\omega_x/2\pi = 45$ Hz along $\hat{e}_x$. Note that in the quasi-momentum frame, the atoms in $|\text{aux}\rangle$ are at $k_x = 1\,k_R$ in the minimum of the dispersion.

We prepare the condensate at different momenta by imparting a kick k_{kick} to the atoms and afterwards letting the condensate oscillate in the trap for a variable waiting time τ_{wait}, so that the momentum is changing by $k_x = k_{\text{kick}}\cos(2\pi \times f_x \tau_{\text{wait}})$. For momenta $k_x < 0.5\,k_R$ or $k_x > 1.5\,k_R$, we employ Raman-Nath diffraction from an optical lattice[179–181]. The lattice has a wavelength of $\lambda_L = 1064$ nm and thus the momentum imparted on the atoms is $\pm k_{\text{kick}} = \pm 2 \times 2\pi/\lambda_L = 2k_L = \pm 1.44\,k_R$. We choose to pulse the lattice with shallow depth of $V_0 \approx 4\,E_L$ for 45 µs, so the diffraction orders above $\pm k_R$ are suppressed and the three orders $0, \pm k_R$ have a

similar population.

For momenta between $0.5 > k_x > 1.5\ k_R$ we could not apply the same method as the three peaks form the 0 and $\pm k_R$ order got unresolvable in space after time of flight. Instead, we applied a magnetic gradient in x-direction for 1 ms to prepare the BEC at a momentum in this range.

We calibrate the momentum for a certain waiting time τ_{wait} by employing the momentum resolution of a Raman π-pulse. As described in section 5.4, the resonant frequency for a Raman π-pulse between $|\downarrow\rangle$ and $|\uparrow\rangle$ is $f_{R,0} = (E_\uparrow - E_\downarrow)/h + 4hk_R^2/(2m)$ with $2k_R$ the momentum transferred by the Raman beams. If the atoms in state $|\downarrow\rangle$ have a velocity $v_x = \hbar k_x/m$, the frequencies of the Raman beams as experienced by the atoms are modified by the Doppler effect: The frequencies get blue- and red-shifted for the beam travelling in the same and opposite direction:$f_{k_x} = (1 + (|v_x|/c))f$ and $f_{-k_x} = (1 - (|v_x|/c))f$, respectively. The effective change in the frequency difference between the two Raman beams is $\Delta f_D = \hbar k_x(f_1+f_2)/cm$ giving $2\pi \times \Delta f_D = \hbar 2k_R k_x/m$ in dimensional units. Therefore the Raman pulse is only resonant for a narrow momentum class k_x and we determine the momentum of the condensate by finding the frequency shift which maximizes the transfer of a π-pulse. By repeating this procedure after different waiting times in the dipole trap, we obtain the momentum calibration, which is shown in Fig. 6.2. In the left and right panel the momentum of the atomic cloud is displayed as function of the wait time in the trap after Bragg diffraction and after applying the magnetic gradient respectively. Both calibrations are compatible with the trap frequency of $\omega_x/2\pi = 45$ Hz (solid lines). However, to account for imperfections in the dipole trap we use empirical polynomial functions (dashed lines) to describe the data.

By combining the spin injection spectroscopy and the momentum calibration we are able to reconstruct the energy band of the lower dressed state. Our result for $\Omega_R/2\pi = 0.97(3)\ E_R/h$, $\delta_0/2\pi = 0.0(2)\ E_R/h$ and a momentum range $(-0.1 - 2.3)\ k_R$ is displayed in Fig. 6.3. Our data points agree well with the single particle theory (solid line). Remarkably, we can resolve the difference between Raman-dressed band and the free particle dispersion (dashed lines) at $k_x = 1\ k_R$, which corresponds to a energy difference of $\sim 0.07\ E_R$ or frequency difference of ~ 570 Hz, respectively.

From the same absorption images we extract the spin composition of the atoms transferred to the Raman-dressed band and calculate the polarization P_{exp}

$$P_{\text{exp}} = \frac{N_\uparrow - N_\downarrow}{N_\uparrow + N_\downarrow} \tag{6.3}$$

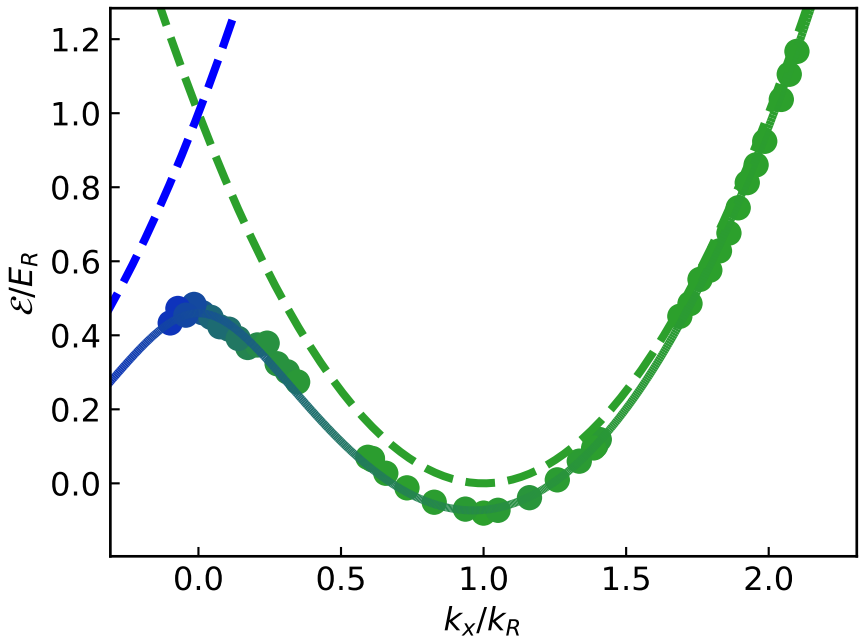

Figure 6.3: Measurement of the lower dressed state energy band with spin injection spectroscopy in a ^{41}K BEC for $\Omega_R/2\pi = 0.97(3)\ E_R/h$ and $\delta_0/2\pi = 0.0(2)\ E_R/h$. The colour of the data points indicates the measured polarization, as explicitly plotted in Fig. 6.4. The dashed lines represent the free particle dispersion relations of the $|\downarrow\rangle$ (green), $|\uparrow\rangle$ (blue) states and the solid line describes the prediction for the lower dressed state $|-\rangle$, see section 3.2.2.

with the atom number $N_\downarrow$, $N_\uparrow$ of the bare states in which the atoms in the dressed band are projected in. We show the obtained P_{exp} for different values of k_x in Fig. 5.8. It matches well with the prediction calculated with $P = \tilde{\delta}/\tilde{\Omega}_R$.

6.2 Experimental observation of the static vector potential

In the single minimum regime, Raman coupling can be effectively described as the presence of a vector potential acting on the atoms and a modified atomic mass (see chapter 3). In this section, we measure the synthetic one-dimensional vector potential induced by the Raman coupling along $\hat{e}_x$. As explained previously, the vector potential A_0 for this configuration is static and is given by the change of the minimum of the dispersion: $eA_0 = k_{\text{min}}$. We here follow a technique pioneered in the Spielman group[99,100] to directly measure the strength of the vector potential.

The measurement consists out of preparing the atoms in the lower dressed state and afterwards determining the vector potential experienced by the atoms *via* the

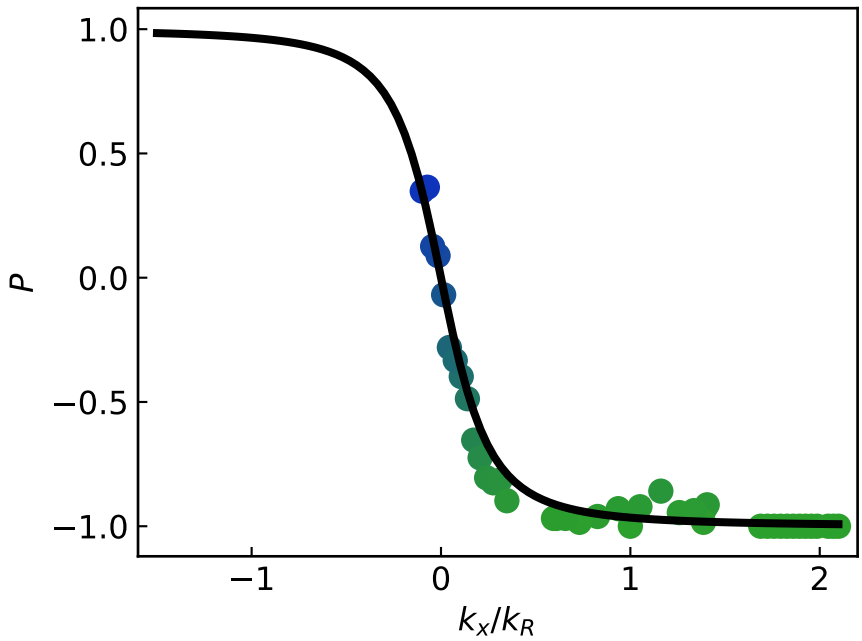

Figure 6.4: Measured polarization P of the atoms transferred with spin injection spectroscopy to the Raman-dressed band $|-\rangle$ with $\Omega_R/2\pi = 0.97(3)\ E_R/h$ and $\delta_0/2\pi = 0.0(2)\ E_R/h$ as function of the quasi-momentum k_x. The solid line shows the expectation $P = \tilde{\delta}/\tilde{\Omega}_R$.

momentum they have acquired in the modified dispersion. More precisely, the vector potential A_0 is given by $eA_0 = k_{\mathrm{min}} = k_{\mathrm{x}} - k_{\mathrm{mech}}$, so the measurement of the vector potential reduces to the determination of the quasi- and mechanical momentum. In the following we will describe the measurement methods and results in detail.

We load the condensate into the lower Raman-dressed band with $\Omega_R/2\pi = 5.0(3)$ E_R/h and $\delta_0/2\pi$ in the range $(-12.1 - 12.1)\ E_R/h$. This is achieved with the following steps: first, we ramp up the Raman power to $\Omega_R/2\pi = 1.00(6)\ E_R/h$ in 10 ms at $\delta_0/2\pi = -12.1(6)\ E_R/h$. Afterwards, we sweep the frequency in 10 ms to $\delta_0/2\pi = -0.6(6)\ E_R/h$. At this detuning, we further ramp up the Raman power to its final value $\Omega_R/2\pi = 5.0(3)\ E_R/h$ in 20 ms. As last step, we sweep to the final detuning in 10 ms. In case of a final detuning $\delta_0/2\pi < -0.6\ E_R/h$ the last step is omitted. All ramps are of linear form. The preparation follows roughly the concept of the procedure outlined in section 5.6, differences are due to historical reasons.

In order to measure the vector potential experienced by atoms in the lower dressed band, we have to obtain the total quasi-momentum and the mechanical momentum

of the atoms. We measure the quasi-momentum k_x with time of flight imaging and distinguish the contributions from k_{mech} and k_{min} by measuring the momentum oscillation in the presence of the Raman coupling in the dipole trap. Whereas the mechanical momentum is changing with waiting time in the trap as kinetic energy is transformed in potential energy and vice versa, the momentum in the minimum of the dispersion remains the same as it only depends on the Raman parameters. Therefore k_{min} corresponds to the average over full periods of the oscillation, which is captured by the offset when describing the oscillation with a trigonometric function. Fig. 6.5 shows the measured quasi-momentum oscillations for different values of the final detuning δ_0. We fit a sine function (solid lines) to the data to extract k_{min} (dashed lines).

In Fig. 6.6 the measured vector potential $eA_0 = k_{\text{min}}$ as function of the two-photon detuning is displayed. The data is in excellent agreement with the single particle theory (solid line), which is the numerical solution of eq. (3.11). This measurement was performed with the isotope ^{39}K, for which we expect an additional density dependent detuning caused by interaction effects on top of the single particle effects. This detuning would lead to a shift of the vector potential with respect to the single particle theory. However, we don't expect to resolve this discrepancy as the interaction induced detuning is on the order of a few hundreds Hz and in the

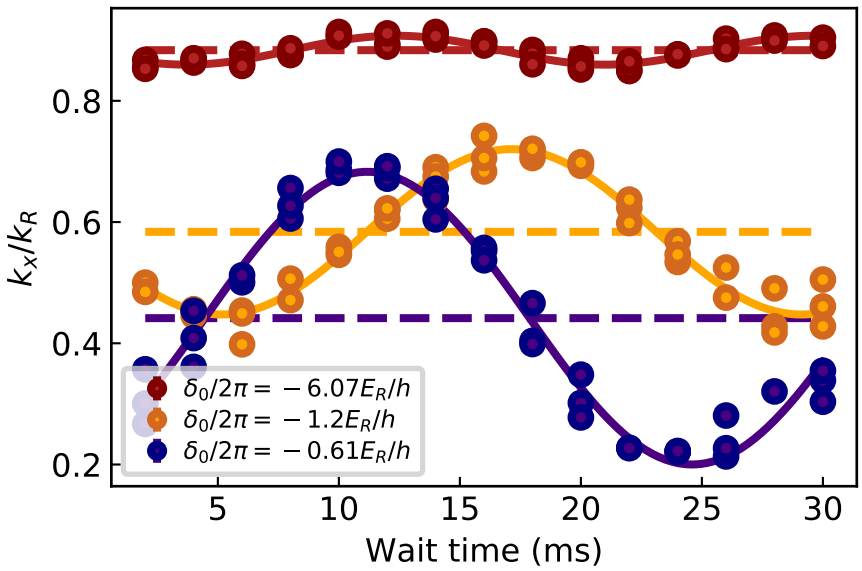

Figure 6.5: Measured oscillations for the quasi-momentum k_x of the dressed state $|-\rangle$ with $\Omega_R/2\pi = 5.0(3)\ E_R/h$ as function of waiting time in the optical dipole trap. We fit sine functions to the data (solid lines). The momentum k_{min} in the minimum of the Raman-dressed dispersion is the average of the oscillation, namely the offset (dashed lines) obtained out of the fit.

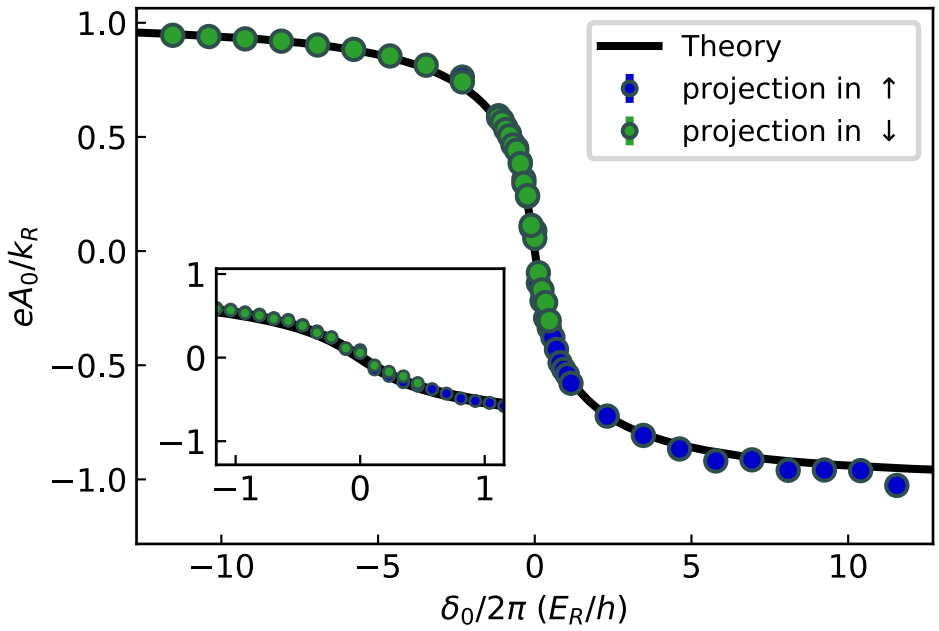

Figure 6.6: Gauge potential A_0 for ^{39}K at $\Omega_R/2\pi = 5.0(3)\ E_R/h$ as function of the final detuning δ_0. The line is the single particle theory calculated with eq. (3.12). Uncertainties are obtained by error propagation of the fit covariances and are below the marker size.

case of ^{39}K we are limited by the stability of the two-photon detuning which is in the order of 500 Hz (as detailed in chapter 5).

6.3 Effective mass: modified free expansion dynamics

In eq. (3.8) we have introduced a momentum-dependent effective mass $m^*(k_x)$ that accounts for the non-constant curvature of the modified dispersion relation. The effective mass has severe consequences in the free dynamics of the Raman-dressed particles. This was first investigated in the group of Prof. Engels, where a negative effective mass regime was realized and the resulting hydrodynamics including an anisotropic expansion and self-trapping effects were studied [98].

Here we also study the expansion dynamics of the Raman-dressed atoms for the experimental parameters relevant in the next chapter 7. In contrast to Ref. [98], which investigates the regime of $\Omega_R/2\pi = 2.5\ E_R/h$ and positive detuning, we study the effect in the single minimum regime with $\Omega_R/2\pi = 4.5(1)\ E_R/h$ and around $\tilde{\delta}_0/2\pi = 0.0(2)\ E_R/h$. In this regime the effective mass remains always positive (compare with Fig. 6.8). Nevertheless, it also leads to an asymmetric expansion dynamics and the density distribution develops a skewness which depends

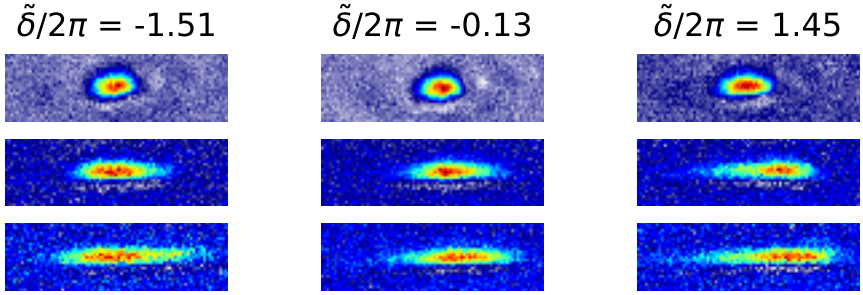

Figure 6.7: Integrated *in situ* density profiles for the Raman-dressed ^{41}K condensate with $\delta_0/2\pi = (-0.18(2), 0.12(2), 0.61(2))\ E_R/\hbar$ and $\Omega_R = 4.5(1)\ E_R/h$ after an expansion time t in an optical waveguide. The values of δ_0 correspond to $\tilde{\delta}/2\pi = (-1.51(14), -0.13(10), 1.45(08))\ E_R/h$ measured experimentally with spin ejection spectroscopy. **Top to bottom:** $t = 1$ ms, $t = 10$ ms, $t = 15$ ms.

on the generalized detuning $\tilde{\delta}_0$.

We probe the effective mass of the dressed atoms with the following procedure: first, we prepare the atom in the lowest dressed state with $\Omega_R/2\pi = 4.5(1)\ E_R/h$ and $\delta_0/2\pi = (-0.18(2), 0.12(2), 0.61(2))\ E_R/h$. However, as outlined in section 5.5, our system is described in terms of the generalized detuning $\tilde{\delta} = \delta_0 - 4k_x$, where k_x can stem from the finite momentum in the minimum of the dispersion k_{min} as well as from mechanical momentum k_{mech}. Because the mechanical momentum is unknown and originates i.e. from the preparation procedure, we perform additional experiments to infer $\tilde{\delta}$ after the preparation of the BEC into the lowest Raman-dressed state.

To this end, we inverse the spin injection method used in section 6.1 to measure directly the energy of the occupied dressed-band by ejecting atoms from the $|-\rangle$ state into the unoccupied bare state $|\text{aux}\rangle$ by radio-frequency spectroscopy. Out of the mismatch between the measured and the expected energy of the Raman-dressed state with Ω_R and $\delta_{0,\text{fin}}$, we infer the mechanical momentum. From this calibration for each used detuning δ_0, we obtain $\tilde{\delta}/2\pi = (-1.51(14), -0.13(10), 1.45(08))\ E_R/h$.

Similar to Ref. [98], we prepare the Raman-dressed condensate in a crossed optical dipole trap formed by the waveguide trap along $\hat{e}_x$ and a vertical beam along $\hat{e}_z$, and afterwards release the $\hat{e}_z$ beam and let the cloud freely expand in the waveguide potential along the Raman coupling direction. Because we are interested in the density distribution, we use the phase contrast scheme to image the condensate *in situ*. In Fig 6.7, *in situ* images are displayed for different values of $\tilde{\delta}$ and evolution times. Whereas the expansion for $\tilde{\delta} \approx 0$ is symmetric as for the free particle case, the expansion gets anisotropic as soon as $\tilde{\delta} \neq 0$. For different

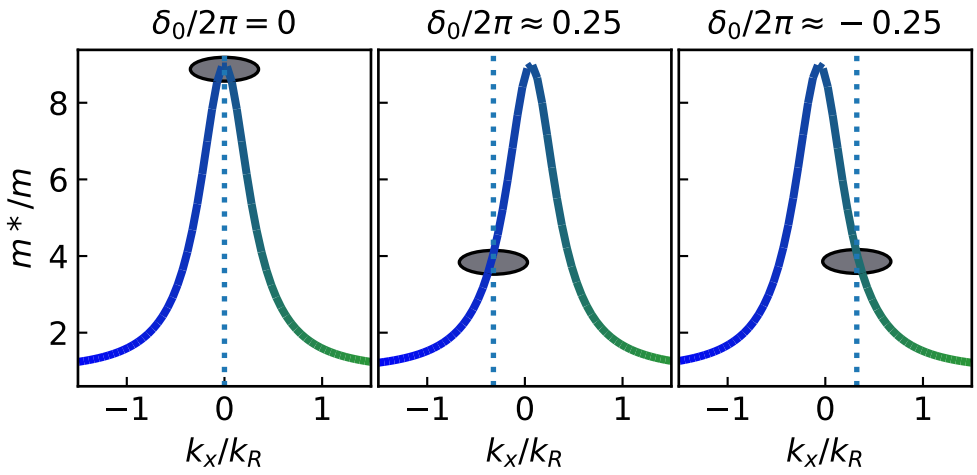

Figure 6.8: Effective mass $m^*(k_x)$ calculated with eq. (3.8) for $\Omega_R/2\pi = 4.5(1)\, E_R/h$ and different values of the detuning $\delta_0/2\pi$, given in units of E_R/h. The colour encodes the spin polarization P. The dashed lines indicates the position of k_{min}, i.e. the centre of mass momentum of the condensate in the case of no mechanical momentum.

signs of detuning, the distribution is skewed in opposite directions. This effect can intuitively be explained in the effective mass picture: the momentum distribution of the cloud is centred around $k_x = 0$. For $\tilde{\delta} = 0$, the effective mass is symmetric around $k_x = 0$ and hence atoms in the different halves of the cloud (i.e. in the left halve with $k_x < 0$ and in the right half with $k_x > 0$) have an effective mass which only depends on the modulus of k_x, leading to a symmetric expansion. For $\tilde{\delta} \neq 0$, the peak of the effective mass is shifted. Now, for $\tilde{\delta} < 0$, atoms with $k < 0$ are heavier than atoms with $k > 0$ and vice versa for $\tilde{\delta} > 0$. Atoms with a higher effective mass have a slower dynamics and thus expand less compared to atoms with lower effective mass. Therefore the different effective mass in the two halves of the atomic cloud causes a growing asymmetry in the density profile and the direction of skewness is defined by the sign of $\tilde{\delta}$. This concept is summarized in the illustration of Fig. 6.8.

In order to compare our experimental results to theoretical prediction we need to find a reliable method to quantify the skewness of the density distribution. We decided to use the skewness parameter $s = \frac{\mu_3}{\sigma^3}$, where σ and μ_3 are the second and third central moments of the density distribution. Details about the data analysis can be found in the next chapter 7. In Fig. 6.9 the extracted skewness s from the experimental data is shown. It captures well the opposite sign of the asymmetry for $\tilde{\delta} < 0$ and $\tilde{\delta} > 0$ and is zero within the error bars for $\tilde{\delta} = 0$. After ~ 8 ms the skewness parameter stops increasing, which we attribute to the condensate entering the ballistic expansion regime. Indeed, from the Castin-Dum scaling so-

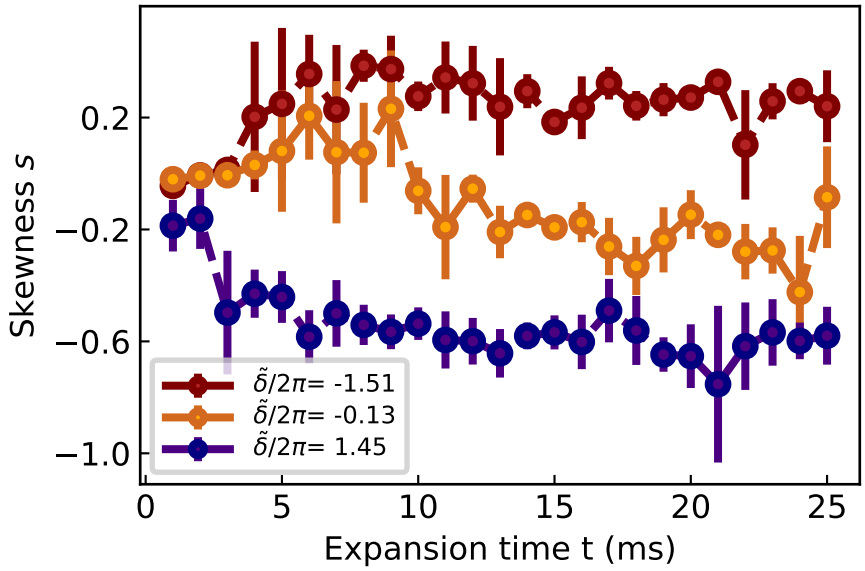

Figure 6.9: The skewness parameter s as function of the expansion time t for a BEC of ^{41}K under the influence of Raman dressing with $\Omega_R/2\pi = 4.5(1)\ E_R/h$ and positive and negative values of generalized detuning $\tilde{\delta}/2\pi$, given in units of E_R/h. The data points are the mean over 4 experimental realizations and the error bars the standard deviation.

lutions[122], we obtain that the condensate's width after $\sim$ 5 ms increases linearly for our experimental parameters, i.e. the expansion gets ballistic. So at this point the potential energy is converted to kinetic energy and the shape of the atomic cloud, including its asymmetry, will remain constant which is in good agreement with the experimental data.

6.4 Conclusion

We have studied single particle effects of Raman-coupled BECs similarly as reported in previous experiments[98–102,107,152–157,162–166] which enables us to distinguish those from interaction effects in chapter 7. While none of the measurements is new in itself, their added value lies on the new experimental techniques developed in the thesis. For instance, this is to our knowledge the first implementation of Raman coupling in potassium BECs, we extended the method of spin injection of the full dressed band of a Fermi gas to a Bose-Einstein condensate or established a new analysis method for the asymmetric density profiles when studying the effective mass.

Based on the work presented in this chapter, we can also conclude about our further procedure to measure the chiral BF gauge field from the encoded theory. We

have shown that we do not have the stability to measure the density-dependent part of a vector potential in a ^{39}K BEC *via* the quasi-momentum. An alternative approach was described in chapter 2 and involves measuring the modified expansion dynamics of the condensate. However, because the expansion is also changed by the effective mass of the particles as observed in this chapter, we will have to differentiate these two effects.

7 Experimental simulation of the encoded chiral BF theory

In this chapter we report on the experimental realisation of the chiral BF theory in its encoded form. Our implementation relies on the combination of Raman coupling and state dependent scattering lengths. We experimentally probe the resulting chiral interactions present in the system and observe the two main features of the encoded chiral BF theory, namely the formation of chiral solitons and the BF electric field.

We have seen in chapter 3 that we can realize the chiral BF gauge theory in a Bose-Einstein condensate by engineering chiral interactions *via* the combination of Raman coupling and different interactions in the coupled states. We have studied both ingredients in our experimental platform independently, namely the interaction control by coherent coupling in ^{39}K (see section 4.2) and Raman coupling on the single particle level (see chapter 6). In this chapter we combine these two key elements and present the main result of this thesis: the experimental realization of the chiral BF theory. To this end we proceed as follows: we first demonstrate the momentum-dependent nature of interactions in the system by studying the expansion dynamics of condensates with different momenta (see section 7.1). Afterwards we provide evidence for the realization of the chiral BF theory in its encoded form by observing its defining properties. First, we observe the formation of a chiral bright soliton whose existence relies on its momentum. We probe its chiral nature by reversing its propagation direction (see section 7.2). Second, we use the local symmetry constraint of the theory to reveal the BF gauge field through measurements of the modified expansion dynamics of the condensate (see section 7.3).

As in the previous experimental chapters, all Raman parameters and momenta are expressed in units of the Raman recoil energy E_R and momentum k_R respectively. In contrast to chapter 3, we do not set E_R,k_R and $\hbar$ to one. Other quantities are given in SI units.

The results presented in this chapter were obtained in close collaboration with my PhD colleague Craig Chisholm and the two Postdocs of my group Dr. Elettra Neri and Dr. Ramón Ramos. Our work led to the manuscript "Realising a one-dimensional topological gauge theory in an optically dressed Bose-Einstein condensate" which is currently in preparation for submission. I share the first authorship with Craig Chisholm. This chapter recalls some parts of our manuscript without major modification and develops further certain aspects such as experimental techniques, the quasi-momentum violation for the chiral soliton or the analysis of asymmetric density profiles.

7.1 Experimentally probing chiral interactions

In a first series of experiments, we investigate the combination of Raman coupling and interactions, and show the anticipated resulting momentum-dependent nature of interactions in this system. We investigate the dynamics of the Raman-dressed atoms when propagating in opposite directions in the waveguide potential along the x-axis.

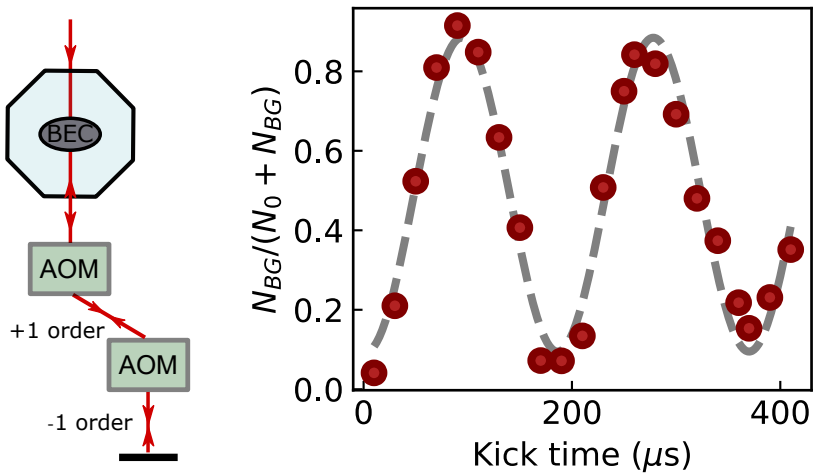

Figure 7.1: Imparting momentum to the atoms *via* Bragg diffraction. **Left:** schematics of the Bragg setup with two consecutive AOMs in double-pass configuration. **Right:** resonant Bragg diffraction in the state $|\downarrow\rangle = |F = 1, m_F = 0\rangle$ of ^{41}K (without Raman dressing) as function of applied pulse length for a Bragg beam laser power of ~ 24 mW corresponding to a lattice depth of $s \approx 5\ E_L$ where $E_L = \hbar^2 k_{BG}^2/(2m_{41})$ is the recoil energy of the Bragg light. N_{BG} denotes the atom number transferred to the momentum class $2\hbar k_{BG}$, N_0 the number of atoms at the initial momentum.

Methods and Bragg diffraction

We start with the BEC in the crossed dipole trap with trapping frequencies $(\omega_x, \omega_y, \omega_z)\ /2\pi = (75(2), 128(2), 51(4))$ Hz and prepare state $|-\rangle$ close to the minimum of the dispersion with $\Omega_R/2\pi = 5.3(3)\ E_R/h$ and $\delta_0/2\pi = -2.62(6)\ E_R/h$ at a magnetic field of $B = 374.30(1)$ G. At this field strength the scattering lengths are $a_{\uparrow\uparrow} = -4.9\, a_0$, $a_{\downarrow\downarrow} = 24.6\, a_0$ and $a_{\uparrow\downarrow} = -13.8\, a_0$ (see Fig. 4.4). Afterwards we remove the vertical confining beam, so the trapping frequencies change to $(\omega_x, \omega_y, \omega_z)/2\pi = (4(1), 98(2), 51(4))$ Hz, and we impart a well-defined momentum to the condensate.

We give momentum to the BEC in the waveguide by Bragg diffraction. The Bragg diffraction is realised by subjecting the atoms to two counter-propagating laser beams of wavelength $\lambda_{BG} = 1064$ nm, which form a standing wave. Similarly as for the Raman coupling this corresponds to a Λ-coupling *via* a two-photon process. But in contrast to the Raman coupling, the beams are far off-resonant, and they couple two different energy states of the same internal spin state, separated by momentum $2 \times k_{BG}$ where $k_{BG} = 2\pi/\lambda_{BG}$.

In order to resonantly drive the population transfer to a single momentum state we have to be able to adjust the relative frequency between the two counter-

propagating Bragg beams. The energy difference between two momentum states in the lower dressed band is for our settings typically in the order of $\Delta E/h = \Delta f_{BG} =$ (5-20) kHz. To realize such small frequency difference between the two beams we employ a "quadruple-pass" AOM configuration[182] as shown in the left panel of Fig. 7.1. After the Bragg beam with frequency f_{BG} crossed the chamber once, it passes two AOMs consecutively, is reflected and passes a second time through the two AOMs. We use the light diffracted into the plus order of the first AOM driven at frequency $f_0 + \Delta f_{BG}/2$ and the minus diffraction order of the second AOM driven with f_0. With this setup, the beam entering again the chamber has the desired frequency of $f_{BG} + 2(f_0 + \Delta f_{BG}/2) - 2f_0 = f_{BG} + \Delta f_{BG}$.

For the case of resonant transfer to the momentum state $+2\hbar k_{BG}$, the right panel of Fig. 7.1 shows the fraction of transferred atoms as function of the time duration for which the standing wave with lattice depth $s \approx 5\ E_L$ with $E_L = \hbar^2 k_{BG}^2/(2m)$ is applied to the condensate. A pulse duration of $\tau_\pi = 84\,\mu$s corresponds to a π-pulse. The discrepancy of the typically maximal detected fraction of 88 % from the expected full transfer at τ_π mainly stems for experimental limits in the control of the relative Bragg detuning, for example due to the momentum spread of the atomic cloud and fluctuations of the laser beam power. After imprinting $\Delta k = \pm 1.45\ k_R$ to the cloud by applying a Bragg pulse of time τ_π, we let the condensate propagate for variable time and image the atomic cloud *in situ*. Typical atom numbers at 1 ms of expansion time are $14(4) \times 10^3$.

Expansion dynamics for different momenta

Figure 7.2 shows the observed dynamics of the Raman-dressed ^{39}K condensate after imparting opposite momenta: $\Delta k = -1.45\ k_R$ in the left and $\Delta k = +1.45\ k_R$ in the right panel.

From the *in situ* images at different propagation times, we extract the centre of mass positions x_0, y_0 and widths σ_x, σ_y of the cloud by fitting the data with a 2D Gaussian $A\exp\left(-(x-x_0)^2/2\sigma_x^2\right)\ \exp\left(-(y-y_0)^2/2\sigma_y^2\right) + B$. The centre of mass positions are depicted in the left panel of Fig. 7.3. We measure a centre of mass velocity of (17.38 ± 0.03) mm/s for a BEC moving with $k_x > 0$, which is nearly twice as large as (-8.83 ± 0.02) mm/s observed for $k_x < 0$ (dashed lines). These values are in fair agreement with the single-particle theoretical prediction $v = \partial_{k_x}\mathcal{E}$, which give 16.78 mm/s and -8.96 mm/s, not taking any initial mechanical momentum before the Bragg kick into account (solid lines). The difference in the modulus of the two velocities reflects the non-parabolic form of the dispersion relation $\mathcal{E}(k_x)$ at the Rabi frequency employed here.

More interestingly, the width σ_x of the atomic cloud along the propagation direction is also markedly different in the two cases. As shown in the right panel

of Fig. 7.3, for $k_x > 0$ the BEC expands to more than three times its initial size in 12 ms, whereas for $k_x < 0$ it preserves its shape and σ_x remains constant. This difference reveals the momentum dependence of interactions in our Raman-dressed system. The effective scattering length a_1 corresponding to the effective coupling strength g_1 of zero order in our Taylor expansion (see eq. (3.28) and eq. (3.30)), is $a_1 \approx 21\, a_0$ for $k_x > 0$ and $a_1 \approx -2.7\, a_0$ for $k_x < 0$. In particular, the cloud kicked to negative momenta shows no collapse despite the negative effective scattering length. We attribute this collective behaviour to the formation of a bright soliton. Due to the intrinsic chirality of interactions in our system, this propagating mode of matter is only allowed for negative momenta. This novel matter wave excitation is studied in more detail in the next section.

7.2 Chiral soliton

The one-dimensional chiral BF theory predicts novel soliton solutions which are of chiral nature. In this section, we characterise the Raman-dressed soliton by investigating its behaviour after abruptly reversing its propagation direction.

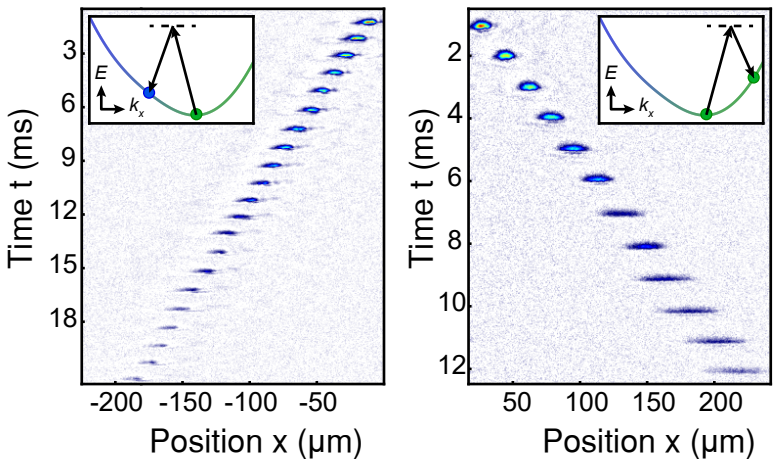

Figure 7.2: Observation of momentum-dependent interactions. Integrated density profiles of a Raman-dressed ^{39}K BEC with $\Omega_R/2\pi = 5.3(3)\, E_R/h$, $\delta_0/2\pi = -2.62(6)\, E_R/h$, $a_{\uparrow\uparrow} = -4.9\, a_0$, $a_{\downarrow\downarrow} = 24.6\, a_0$ and $a_{\uparrow\downarrow} = -13.8\, a_0$, subjected to a magnetic field of $B = 374.30(1)$ G and measured after an evolution time t in the optical waveguide (vertical axis). A mechanical momentum of $\Delta k = -1.45\, k_R$ (left panel) or $+1.45\, k_R$ (right panel) is imparted along the Raman-coupled x axis using two additional Bragg beams. The dressed state in the dispersion relation is shown before and after the Bragg pulse in the insets.

Methods and barrier potential

We follow the same procedure as in the previous section to create a Raman-dressed soliton and add a potential barrier perpendicular to the propagation direction. In the collision with the barrier, the soliton gets reflected and its propagation direction reversed.

We create a potential barrier for the atoms using a blue-detuned laser beam at a wavelength of $\lambda = 765.03$ nm and propagating along the z-direction. We use the addressing setup (see chapter 4) and a cylindrical lens to obtain a strongly elliptic beam with a $1/e^2$ radius of $w_x = 14\,\mu$m along the propagation direction of the atoms and with a waist of $w_y = 350\,\mu$m in the perpendicular direction. The barrier is focused on the left side of the BEC's initial position, such that the atomic cloud with $k_x < 0$ starts interacting with it after a few milliseconds of propagation. For barrier heights exceeding the kinetic energy of the atoms, the collision reflects the atomic cloud, inverting its propagation direction[183–185]. In order to distinguish between effects caused by the barrier and the novel nature of the Raman-dressed soliton, we first study the collision of a "conventional" single-component bright soliton on the barrier.

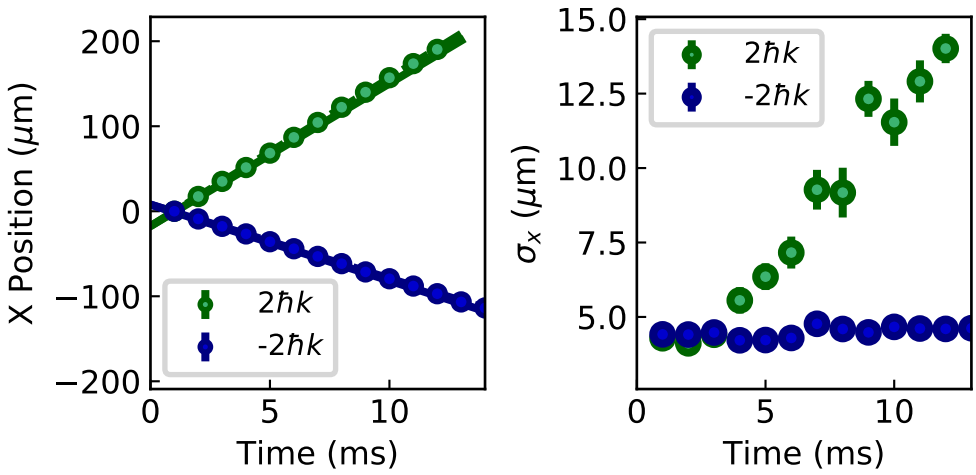

Figure 7.3: Left: position of the atomic cloud vs. propagation time for $k_x > 0$ (green circles) and $k_x < 0$ (blue circles). The different speeds reflect the non-parabolic shape of the dispersion relation, in agreement with single-particle theory (lines). **Right:** measured cloud widths along the waveguide direction. While the cloud expands when propagating towards the right (effective scattering length $a_1 = 21\,a_0$), its size remains unchanged and a bright soliton forms when moving towards the left ($a_1 = -2.7\,a_0$). Values and error bars are the mean and standard deviation of three to five measurements and are extracted from 2D Gaussian fits to the measured density profiles.

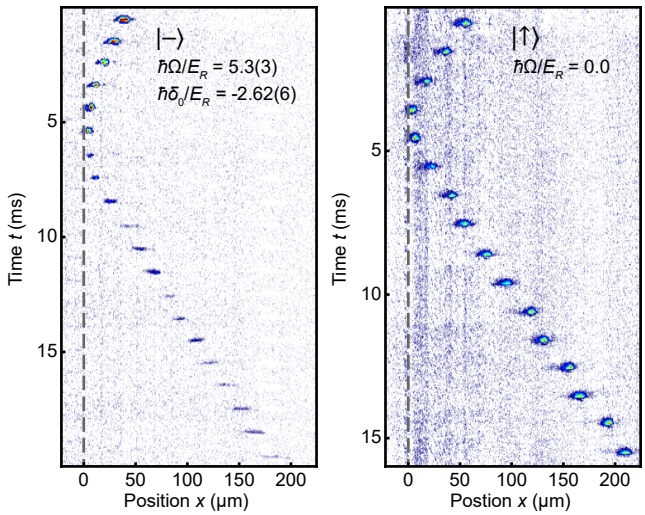

Figure 7.4: Left: *In situ* dynamics in the presence of an optical barrier (dashed line) for a Raman-dressed soliton with the parameters of Fig. 7.2. **Right:** *In situ* dynamics for a conventional bright soliton with scattering length $-2\,a_0$ in state $|\uparrow\rangle$. Upon reflection on the barrier, the Raman-dressed soliton dissociates and starts expanding, while the conventional soliton remains unchanged.

To prepare such conventional soliton, we start with the BEC in state $|\uparrow\rangle$ in the same trapping potential, at a magnetic field of $B = 397.00(2)$ G and atom number of $\sim 7(2) \times 10^3$. As we remove the vertical trapping potential along the z-direction, we linearly decrease the applied magnetic field to $B = 385.60(2)$ G in 5 ms to enter the attractive interaction regime with $a_{\uparrow\uparrow} = -2.2\,a_0$. We set the barrier height larger than the single particle kinetic energy, which is verified by the observed reflection of the soliton from the barrier. As depicted in the right panel of Fig. 7.4, the conventional soliton remains self-bound after reflection. Hence, the barrier only inverts the propagation direction but does not lead to dissociation.

Expansion dynamics after collision with barrier and energy vs. momentum conservation for solitons during reflection

We compare the behaviours of the conventional soliton and the Raman-dressed soliton after colliding with the barrier and getting reflected. In the left panel of Fig. 7.4, the *in situ* dynamics of the Raman-dressed soliton is depicted. In contrast to the conventional soliton, the reflection on the barrier dissociates a Raman-dressed soliton making it expand. We conclude that our Raman-dressed solitons are chiral, that is, they exist only for one propagation direction.

We also investigate the conservation of energy and momentum for the conventional and chiral soliton during the collision with the barrier. The chiral soliton has

a non-parabolic dispersion relation, i.e. atoms with quasi-momenta k_x and $-k_x$ have a different effective mass. Therefore they would not have the same energy and we expect that energy and modulus of the quasi-momentum cannot both be conserved. We test this hypothesis by extracting the velocities of the solitons before and after the barrier. Fig. 7.5, shows the measured centre of mass positions as function of the expansion time. We obtain a velocity of $v = -8.96(21)$ mm/s and $v = -18.33(39)$ mm/s for the chiral and conventional soliton before colliding with the barrier and $v = +13.96(12)$ mm/s and $v = +19.37(22)$ mm/s after reflection. These values agree reasonable well with the predictions from single particle theory of $v = 13.59$ mm/s and $v = 19.24$ mm/s assuming energy conservation during the reflection process. On the contrary, the predicted velocity for the chiral soliton after the barrier assuming quasi-momentum conservation is $v = 0.54$ mm/s. Hence, the experimental data confirms energy and momentum conservation for the conventional soliton and the conservation of energy and violation of quasi-momentum for the chiral soliton. Of course, the overall momentum of the atom plus light field remains conserved.

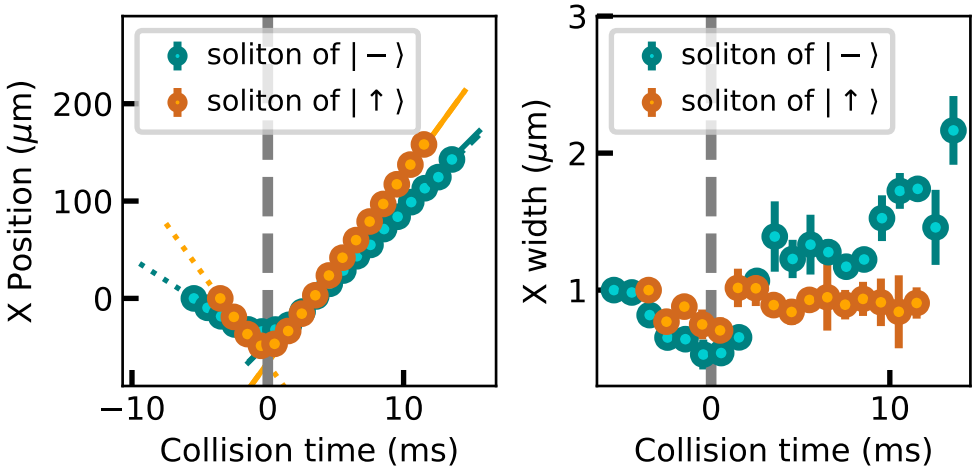

Figure 7.5: Chiral nature of the Raman-dressed soliton. **Left:** centre of mass position for a conventional and chiral soliton, which at $t = 0$ collides with a barrier (gray dashed line). The dotted and dashed lines indicate the linear fit to the data before and after collision, respectively. The solid lines are the predictions for the velocities after collision from single particle theory assuming energy conservation. **Right:** width of the atomic cloud σ_x renormalized by its initial value $\sigma_{x,0}$ as a function of time for conventional and chiral soliton.

Relation to the effective Hamiltonian of the chiral BF theory

Chiral solitons as observed in the previous section, were introduced in section 3.3 as one of the key features of the chiral BF theory. Here, we verify the pa-

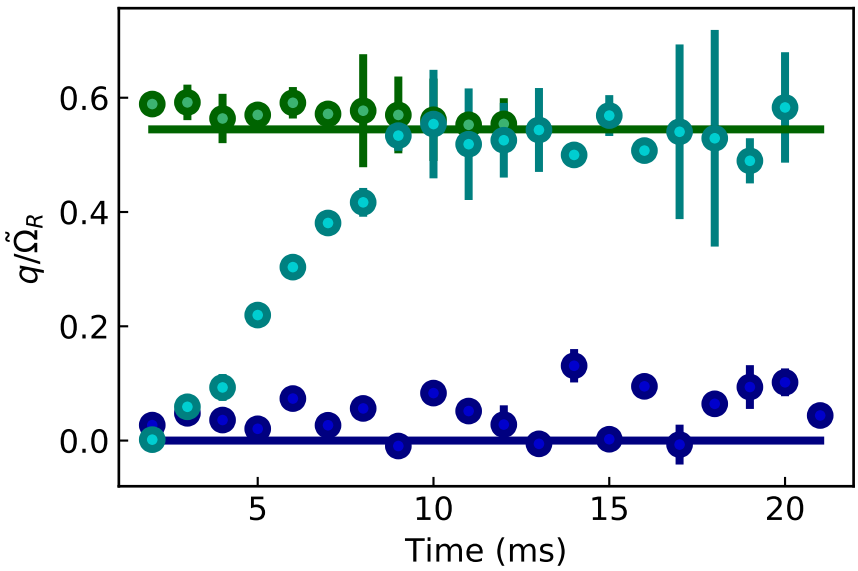

Figure 7.6: Average expansion parameter $q_{\text{ave}}/\tilde{\Omega}_R$ within the atomic cloud. q is estimated from the measured centre of mass momentum of the cloud k_{COM} and the momentum $k_0 = k_{\text{min}}(\Omega_R, \delta_0) + 2k_{BG}$ at which the effective theory is derived: $q = k_{\text{COM}} - k_0$. Blue circles represent the data of Fig. 7.3 ($k_x < 0$), green circles the data of Fig. 7.3 ($k_x > 0$) and cyan circles show $q/\tilde{\Omega}_R$ for the data of the chiral soliton as in Fig. 7.5. The lines indicate the theory predictions. The error bars stem from the uncertainties of the Gaussian fits as relevant for k_{COM} and from the momentum spread Δk of the atomic cloud. In addition, the error bars take the uncertainties in Ω_R and δ_0 into account.

rameter regime in which equation (3.36) provides an appropriate effective description of our Raman-dressed system. To this end, we show in Fig. 7.6 the value of the expansion parameter $q_{\text{ave}}/\tilde{\Omega}_R$ of an average atom around the selected momentum $k_0 = k_{\text{min}}(\Omega_R, \delta_0) - 2k_{BG}$ for all the Raman-dressed data included in Fig. 7.3 and Fig. 7.5. We obtain the average value of $q = k_x - k_0$ by $q_{\text{ave}} = k_{\text{COM}} - k_0$ with the experimentally measured centre of mass momentum k_{COM}. The momentum spread Δk of the atomic cloud is taken into account in the errorbars. For the chiral soliton data without barrier as in Fig. 7.3 for the Bragg kick towards negative momenta (blue points), the centre of mass momentum is $k_{\text{COM},-} \approx k_0$, so the expansion parameter remains small ($q_{\text{ave}}/\tilde{\Omega}_R \leq 0.2$) for all times. In contrast, for the data with an opposite Bragg kick to positive momenta $k_{\text{COM},+} \approx k_{\text{min}}(\Omega_R, \delta_0) + 2k_{BG} = k_0 + 4k_{BG}$ (green points), the centre of mass momentum is far from the expansion point and $q_{\text{ave}}/\tilde{\Omega}_R$ takes values around 0.6. For the bouncing measurements of the chiral soliton as presented in Fig. 7.5 (cyan points), the momentum is inverted from $k_{\text{COM},-}$ to $k_{\text{COM},+}$ between 5 to 9 ms and hence the expansion parameter evolves between the two cases. Note that - as

detailed in the previous section - the centre of mass momentum of the chiral soliton data after colliding with the barrier is approx. 0.4 k_R smaller than for the BEC immediately kicked towards positive momenta (green points) because the momentum is not conserved in the reflection process. However, $0.4\,k_R/\tilde{\Omega}_R \approx 0.09$ and accordingly this difference is hardly visible in Fig. 7.5. The lines are the theoretically expected values for our experimental parameters, not taking any mechanical momentum or the momentum spread into account.

Without further analysis, we consider all data points of positive momenta, including all points after reflection from the barrier in the chiral soliton case where $q_{\text{ave}}/\tilde{\Omega}_R \geq 0.3$, as outside the validity of the effective BF theory. Here, higher order corrections have to be taken into account in the Taylor expansions in eq. (3.19) and eq. (3.28) describing the single particle energy $\mathcal{E}_- = \mathcal{E}_-^{(0)} + \mathcal{E}_-^{(1)} + \mathcal{E}_-^{(2)} + \mathcal{E}_-^{(3)} + \mathcal{O}(q^4)$ and effective coupling strength $g_{\text{eff}} = g_{\text{eff}}^{(0)} + g_{\text{eff}}^{(1)} + \mathcal{O}(q^2)$ and leading to the effective chiral BF Hamiltonian of eq. (3.36).

In the following, we focus on the data for which $q_{\text{ave}}/\tilde{\Omega}_R \leq 0.3$. We estimate in momentum space an upper limit for the next higher order terms of the kinetic and interaction part. To this end, we estimate the corrections in the Taylor expansions for these contributions for a particle with momentum $q = q_0 + 2\pi/\sigma$ where q_0 is the group velocity and σ the momentum spread of the atomic cloud. We weight the importance of these corrections by considering the ratio $\Delta\mathcal{E}_-^{(4)} = \mathcal{E}_-^{(4)}/(\mathcal{E}_-^{(0)} + \mathcal{E}_-^{(1)} + \mathcal{E}_-^{(2)} + \mathcal{E}_-^{(3)})$ and $\Delta g_{\text{eff}}^{(2)} = g_{\text{eff}}^{(2)}/(g_{\text{eff}}^{(0)} + g_{\text{eff}}^{(1)})$, respectively. These ratios are shown in Fig. 7.7 for the data sets of the chiral soliton without (blue

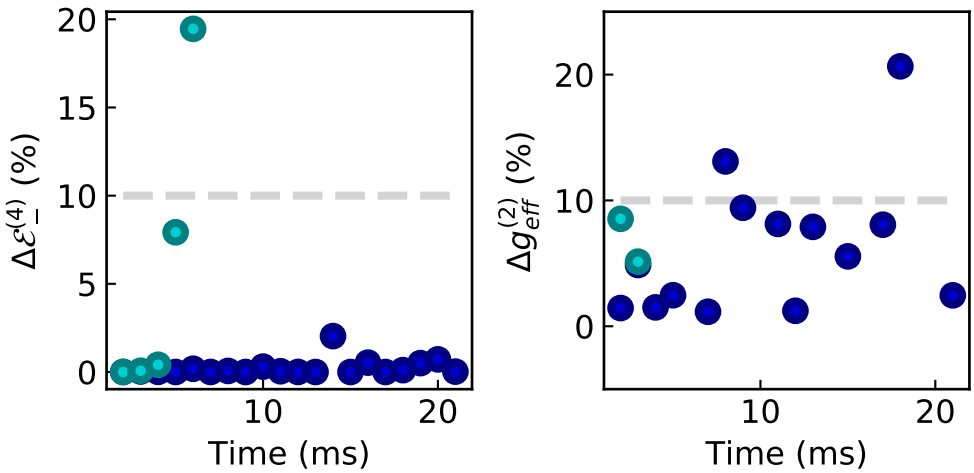

Figure 7.7: Importance of correction terms for data with $q/\tilde{\Omega}_R \leq 0.3$. **Left:** estimation of the kinetic corrections $\Delta\mathcal{E}_-^{(4)}$. **Right:** estimation of the corrections $\Delta g_{\text{eff}}^{(2)}$ in the interaction part.

markers) and with barrier (cyan markers). For the latter one, we only include times below 7 ms for which $q_{\text{ave}}/\tilde{\Omega}_R \leq 0.3$. Both - kinetic and interaction corrections - remain around 10% for all times in the case of the chiral soliton without barrier (Fig. 7.3), but exceed 10 % already after 3 ms for the data of Fig.7.5.

Another aspect to consider for the validity of the effective encoded chiral BF Hamiltonian, is the assumption of $\tilde{\delta} = 0$ in the derivation of eq. (3.36). This condition is required, because otherwise the static gauge field A_0 depends on q and we cannot introduce the current operator as in eq. (3.33). However, in our measurements we have a small but finite $\tilde{\delta}$, e.g. for the data of Fig. 7.7 we have $\tilde{\delta} \approx 0.28\ E_R/\hbar$. We calculate the relative weight of the first term in A_0 which depends on q, which is ~ 1 % for these data sets and thus negligible.

We conclude that all Raman-dressed solitons observed in Fig. 7.3 and in Fig. 7.5 until 4 ms are fairly well described by the effective chiral BF theory.

7.3 Revealing the chiral BF gauge field

In a second series of experiments, we turn to the chiral BF gauge field. Although we have realized an encoded version of the theory, where the gauge field has been eliminated in terms of matter-only degrees of freedom, both remain related through the local symmetry constraint of the theory. Thus, we can use this relation to infer the BF gauge field from measurements of the matter field. Specifically, we have seen in chapter 2 that the expectation values of the electric field and matter field operators are linked by $\langle \hat{E} \rangle = \lambda \langle \partial_t \hat{\rho} \rangle$. In the weakly interacting regime that we realize, our system is well described by the classical version of the theory and we can simply write $E = \lambda \partial_t \rho$. Thus, by inducing a change in the condensate density, we should observe a modification of the BF gauge potential $A = \lambda \rho + \partial_x \Lambda$ and thus the emergence of a BF electric field. Note that this can also be understood if the encoded Hamiltonian is interpreted as that of matter minimally coupled to a density-dependent vector potential that is a linear function of the density $\mathcal{A} = \lambda \rho / 2$ (see discussion after eq. (2.27), and note that here we use $\mathcal{A}$ to distinguish it from the BF gauge potential A). Then, time variations of the density of the system give rise to changes of $\mathcal{A}$ and thus also to the emergence of a density-dependent electric field.

We choose to introduce the change in density by letting the Raman-dressed ^{39}K BEC expand in the quasi 1D waveguide potential. We study its expansion dynamics as we have done previously in section 6.3 for investigating effects of the momentum-dependent effective mass with a ^{41}K BEC. However, here we expect to observe additional many-body effects due the back-action between matter and gauge field. In contrast to the previous experiments of this chapter, we focus now on the regime

of repulsive effective interactions, so $g_1 > 0$.

Observation of asymmetric expansion dynamics

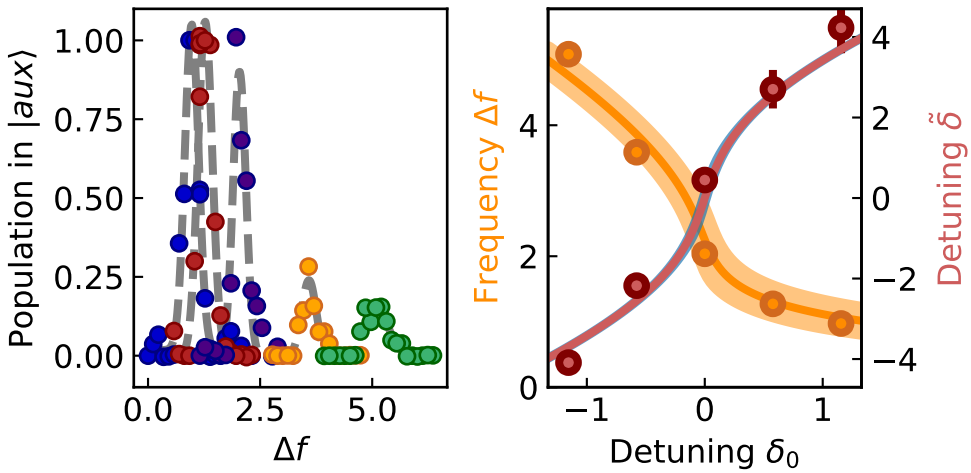

Figure 7.8: Calibration of mechanical momentum by spin ejection. **Left:** rf-spectroscopy on the $|-\rangle$ to $|\text{aux}\rangle$ transition for various values of detuning with $\Omega_R/2\pi = 4.5(3)\, E_R/h$. **Right:** measured frequency difference Δf for $\Omega_R/2\pi = 4.5(3)\, E_R/h$ for various values of detuning (yellow points) and the corresponding values of $\tilde{\delta}/2\pi$ in E_R/h (red points). The solid lines are the theoretical expected values without any mechanical momentum. The shadings illustrate the uncertainties in the theoretical values caused by the uncertainty in δ_0 and Ω_R.

To this end, we start with a BEC in state $|\downarrow\rangle$ and further compress the crossed dipole trap compared to previous experiments to $(\omega_x, \omega_y, \omega_z)/2\pi = (70(1), 147(2), 99(1))$ Hz, which increases the density and hence also enhances the magnitude of density-dependent effects. To ensure $g_1 > 0$, we work at a magnetic field of $B = 397.00(2)$ G, where $a_{\uparrow\uparrow} = 1.3\, a_0$, $a_{\downarrow\downarrow} = 252.7\, a_0$, and $a_{\uparrow\downarrow} = -6.3\, a_0$. We prepare the lower Raman-dressed state $|-\rangle$ with $\Omega_R/2\pi = 4.5(3)\ E_R/h$ and different δ_0 close to the minimum of the dispersion relation. As previously (see section 6.3), we calibrate the actual generalized detuning $\tilde{\delta}$ for each δ_0 with spin ejection spectroscopy. The calibration is shown in Fig. 7.8. On the left side, the measured transfer probabilities for the different values of δ_0 are depicted from which we infer the mismatch in frequency Δf and the actual value of $\tilde{\delta}$ (right panel). For $\delta_0/2\pi = [-0.58(6), 0.00(6), +0.58(6)]\ E_R/h$, we obtain $\tilde{\delta}/2\pi = [-2.18(18), 0.45(33), 2.70(53)]\ E_R/h$, which corresponds to mechanical momenta of $k_{\text{mech.}} = [-0.09(21), -0.11(12), -0.04(21)]\ k_R$, which are within their error bars compatible with zero.

We let such characterized dressed state $|-\rangle$ expand in a trapping potential with

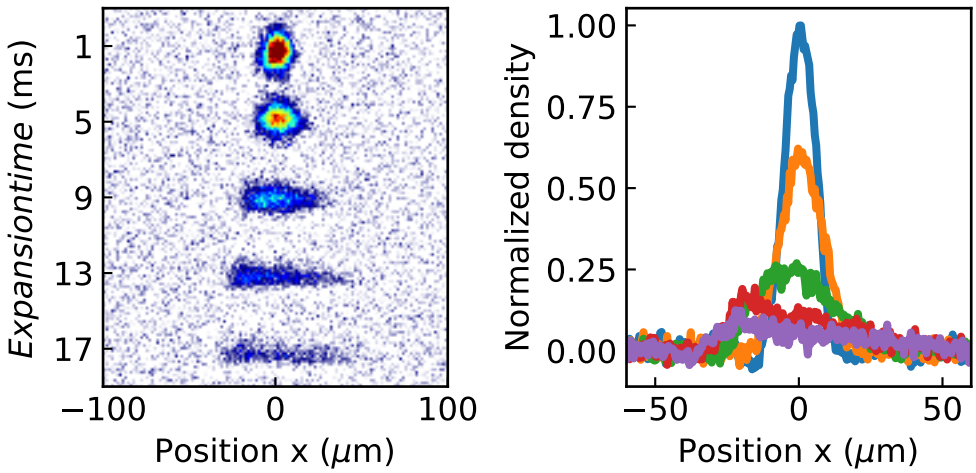

Figure 7.9: *In situ* expansion dynamics for a Raman-dressed BEC in state $|-\rangle$ with $\Omega_R/2\pi = 4.5(3)\ E_R/h$, $\delta_0/2\pi = -0.58(6)\ E_R/h$ and $B = 397.00(2)$ G, corresponding to scattering lengths $a_{\uparrow\uparrow} = 1.3\,a_0$, $a_{\downarrow\downarrow} = 252.7\,a_0$ and $a_{\uparrow\downarrow} = -6.3\,a_0$. The combination of Raman coupling and unequal interactions leads to asymmetry in the density along the x direction. **Left:** integrated density profiles in the xy plane in the optical waveguide along $\hat{e}_x$ **Right:** density profiles obtained after integration along $\hat{e}_y$.

$(\omega_x, \omega_y, \omega_z)/2\pi = (4(1), 129(2), 99(1))$ Hz along the x-axis. After 1 ms of expansion time, we typically have $21(5) \times 10^3$ atoms. The left panel of Fig. 7.9 shows the *in situ* images of the expanding Raman-dressed ^{39}K BEC for $\tilde{\delta}/2\pi = -2.18(9)\,E_R/h$ (and $\Omega_R/2\pi = 4.5(3)\,E_R/h$) in steps of 4 ms. We integrate the images along the y-axis and obtain density profiles as displayed in the right panel of Fig. 7.9.

The Raman-dressed ^{39}K BEC develops an asymmetric density profile over time. At first sight, this behaviour seems similar to the asymmetric dynamics we have already observed in the study of the Raman-dressed ^{41}K condensate (see section 6.3). We aim to systematically study the asymmetric shape of these density profiles and thus need a reliable method to quantify the asymmetry. The data analysis is explained in detail in the next section.

7.3.1 Quantification of asymmetric density profiles

The analysis of the asymmetric density profiles is not straightforward. We tried out different analysis techniques which can be divided in methods based on fitting functions or on purely numerical calculations. We concluded that a quantification *via* a purely numerical approach is less prone to misinterpretation of the data and the most robust method. In particular, we decided to use the skewness parameter

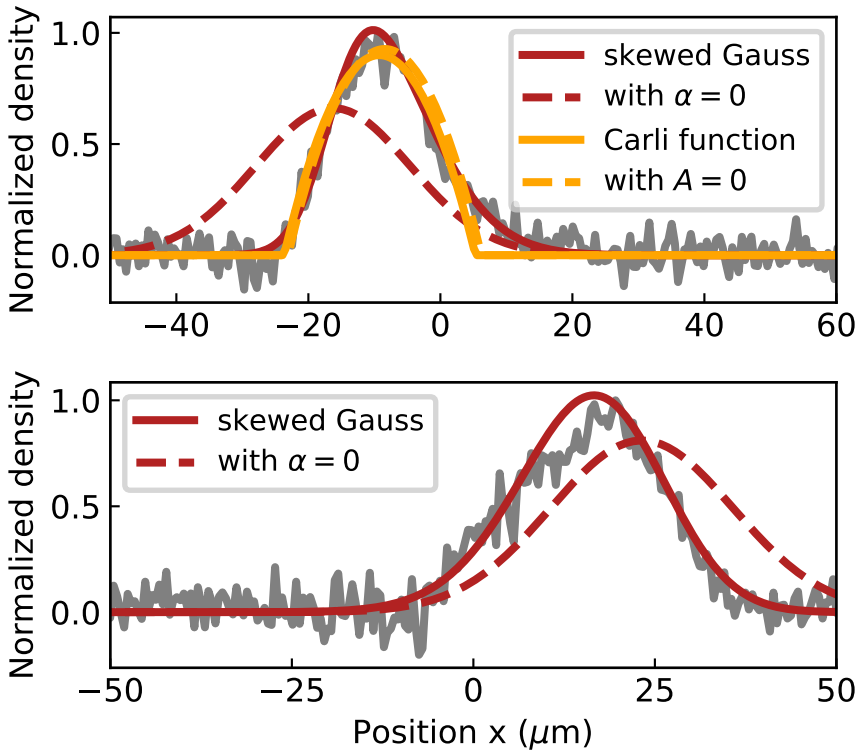

Figure 7.10: Analysis based on fitting functions. Density profile of state $|-\rangle$ with $\Omega_R/2\pi = 4.5(3)\ E_R/h$ and $\delta_0/2\pi = 0.00(6)\ E_R/h$ (**top**) and $\delta_0/2\pi = +0.58(6)\ E_R/h$ (**bottom**) after 14 ms and 18 ms of expansion in the waveguide potential. The solid lines indicate the fits with a skewed Gaussian (eq. (7.1)) and the fitting function of eq. 7.2 defined in Ref. [186]. The dashed lines are the respective fitting functions with the asymmetry parameter set to zero. Both fitting functions fail to describe the data properly.

which is defined as $s = \mu_3/\sigma^3$, where σ and μ_3 are the second and third central moments of the density distribution. For completeness we give a short summary of the different analysis techniques we tried out before we detail the data analysis *via* the skewness parameter.

One possibility to quantify the asymmetric shape is fitting a function with a parameter capturing the asymmetry to the density $\rho = |\Phi|^2$. We tried to fit a skewed Gaussian of the form

$$\left(1 + \mathrm{erf}\left(\frac{\alpha(x - x_0)}{\sqrt{2}\sigma_x}\right)\right) \exp\left(\frac{(x - x_0)^2}{2\sigma_x^2}\right) \tag{7.1}$$

and used the parameter α as measure for the amount of asymmetry. As alternative fitting function we considered the function

$$B \cdot \max\left(0, 1 - \frac{(z - D)^2}{C^2}\right) \frac{1}{1 + A(z - D)} + F \tag{7.2}$$

defined by A. Carli et al. to characterize the asymmetric density profile of an expanding BEC in the Thomas-Fermi approximation[186]. There, the asymmetry evolved from an interaction gradient in space caused by a Feshbach resonance and a magnetic field gradient. In Fig. 7.10 we see exemplary density profiles during expansion for $\Omega_R/2\pi = 4.5(3)\ E_R/h$ and two different values of detuning, namely $\delta_0/2\pi = 0.00(6)\, E_R/h$ (top) and $\delta_0/2\pi = +0.58(6)\ E_R/h$ (bottom). For the top profile we show both fitting functions of eq. (7.1) and eq. (7.2) (solid lines). They give an asymmetry of $\alpha \sim 0.1$ and $A = 0.0006\ 1/\mu\mathrm{m}$, respectively. The dashed lines indicate the same functions with the asymmetry parameter set to zero. Clearly, the parabolic function of eq. (7.2) does not capture the shape of our data properly. Although the fit with the skewed Gaussian seems reasonable for the top profile, it is in general not robust and e.g. fails for the density profile in the bottom panel. Therefore we conclude that our analysis method should not rely on a fitting function as this implies an assumption of the exact shape of the data.

A different approach to characterize the asymmetry is to extract numerically the difference between the two halves of the profile, as outlined by the group of Prof. Fallani in [167]. In this method, the function

$$h(x) = |\Phi(x)|^2 - |\Phi(-x)|^2 \tag{7.3}$$

with the inverted density profile $|\Phi(-x)|^2$ is calculated and the asymmetry A_h of the density profile defined as $A_h = \int h(x)dx$. This concept is illustrated in the right panel of Fig. 7.11. It is necessary to align the middle of the x-axis with the centre of the density profile, otherwise a finite asymmetry arises due to the displacement. Hence, a critical and sensitive step is the extraction of the centre, which is quite involved for an asymmetric profile as it might not correspond to

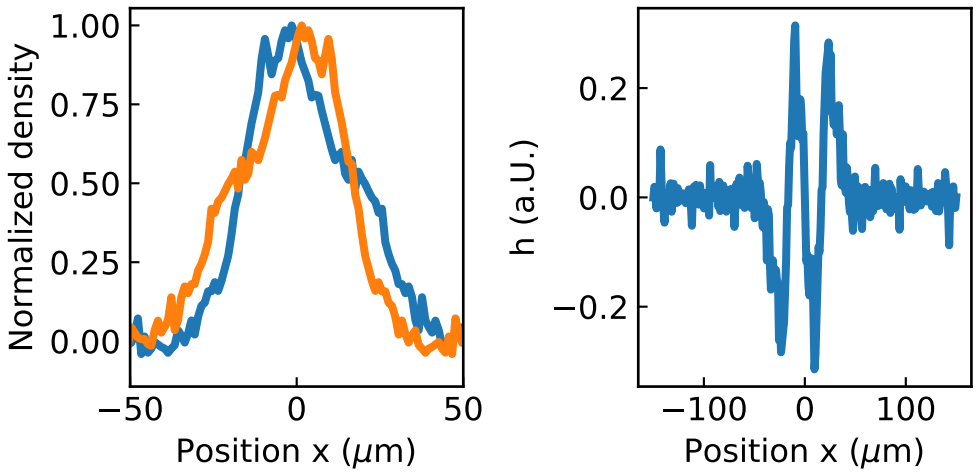

Figure 7.11: Illustration of calculating the asymmetry A_h for $\Omega_R/2\pi = 4.5(3)\ E_R/h$ and $\delta_0/2\pi = -1.15(6)\ E_R/h$. **Left:** normalized density profile and its inversion. **Right:** asymmetry function $h(x)$ of eq. (7.3).

the centre of mass position nor to x_0 from the skewed Gaussian fit, which rather describes the peak position. In Fig. 7.11 we obtained the centre from a symmetric Gaussian fit to the data. However, this is only an approximation and therefore the asymmetry A_h is not trustworthy.

We decided to use a numerical method which does not require any previous knowledge about specific points of the density profile. In a first step, we low-pass filter the data. Our filtering procedure is performed in Fourier space: first, we remove the offset and afterwards apply a low-pass filter with a cut-off frequency defined by the smallest value of $|k|$ which corresponds to a minimum in the power spectral density and has a value less than 1 % of the maximum. We have verified the robustness of our filtering procedure by taking GPE numerical simulations with added artificial noise analogous to which was found in our experimental images, and analysing the resulting profiles with this filtering procedure. After the filtering, we calculate the moments of the distribution. In general the m-th moment is defined as $\mu_m = \int (x-\mu_1)^m \rho(x) dx$, where the first moment $\mu_1 = \int x\rho(x)dx$ is the centre of mass position of the atomic cloud. With the moments, we characterise the asymmetry of the distribution using the standardized third moment also known as skewness parameter $s = \mu_3/\sigma^3$ with the standard deviation $\sigma = \sqrt{\mu_2}$. The skewness s is a dimensionless number and resilient to atom number fluctuations.

Asymmetric expansion as signature of the effective Hamiltonian

We observe and quantify the asymmetry of the density profiles with the skewness paramater s for different values of the detuning, which we show in Fig. 7.12

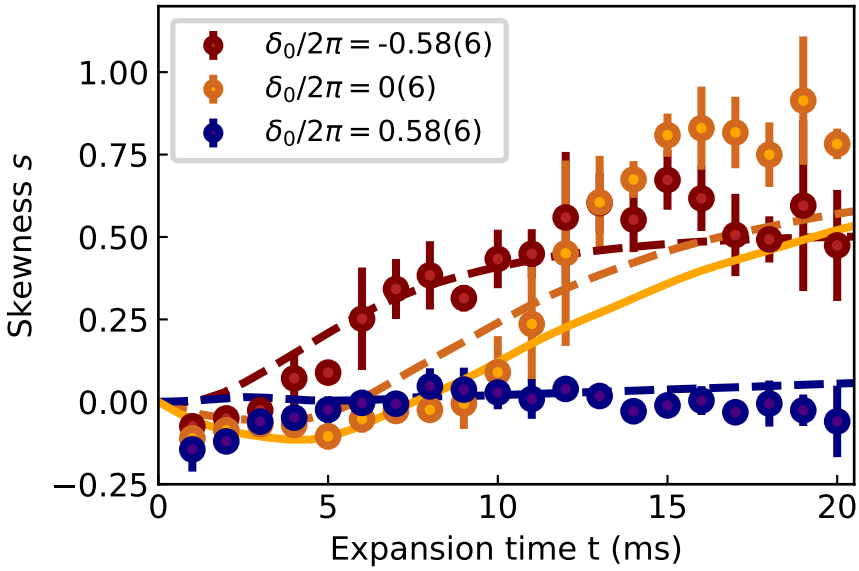

Figure 7.12: Back-action between matter and gauge fields. Skewness of the density profiles $s = \mu_3/\sigma^3$ for $\delta_0/2\pi = \pm 0.58(6)\, E_R/h$ and $0.00(6)\, E_R/h$. The relationship between s and δ_0 arises from the interplay between interaction and kinetic effects caused by the non-parabolic form of the dispersion relation. The dashed lines are numerical solutions of the two-component Gross-Pitaevskii equation. The solid orange line corresponds to the effective encoded chiral BF theory for $\delta_0 = 0$. Values and error bars are the mean and standard deviation of four to five measurements.

for $\delta_0/2\pi = [-0.58(6), 0.00(6), +0.58(6)]\, E_R/h$ or $\tilde{\delta}/2\pi = [-2.18(18), 0.45(33), 2.70(53)]\, E_R/h$, respectively. Interestingly, the evolution of s during the expansion has a non-trivial dependence on detuning. It stems from an interplay of single-particle and many-body effects. On the one hand, we expect skewness arising from the momentum dependence of the dressed atoms effective mass and the momentum spread of the atomic cloud, as we have studied in section 6.3 for ^{41}K and which was originally demonstrated for $\Omega_R/2\pi < 4\, E_R/h$ in Ref. [98]. Concretely, we expect the skewness from these kinetic effects to be $s_{\text{kin}} < 0$ (> 0) for $\delta_0 > 0$ (< 0) at the Rabi frequencies we use. On the other hand, the momentum dependence of interactions makes the atoms expand slower when moving to the left than to the right, leading to a contribution $s_{\text{int}} > 0$ to the skewness independent of the sign of the detuning as predicted in Ref. [52]. Our results confirm this qualitative picture, with both contributions cancelling out for $\delta_0/2\pi = -0.58(6)\, E_R/h$ and adding up when $\delta_0/2\pi = +0.58(6)\, E_R/h$. Moreover, this behaviour is well captured by Gross-Pitaevskii simulations for the Raman-coupled two-component system (dashed lines) and also by our effective chiral BF theory, namely by the extended Gross-Pitaevskii equation stemming from the Hamiltonian of eq. (3.36) (solid line for $\delta_0/2\pi = 0.00(6)\, E_R/h$). By contrast, the interplay of kinetic and

interaction effects is absent in the adiabatic approximation, i.e. where the dispersion is assumed to be parabolic (see chapter 3).

For $\delta_0 = 0$, where the lowest order kinetic corrections to our effective Hamiltonian equation (3.36) cancel out, our experimental observations are also qualitatively reproduced by the predictions of the chiral BF theory. There, the discrepancy between the effective (solid line) and complete (dashed line) theories stems from higher order corrections, which remain sizeable for our experimental Rabi frequency of $\Omega_R/2\pi = 4.5\ E_R/h$ and further drop when increasing the value of Ω_R. This is illustrated in Fig. 7.13 for $\Omega_R/2\pi = 7\, E_R/h$, where the expected density profiles during expansion are essentially indistinguishable in the two cases. This demonstrates the validity of our effective chiral BF theory description well beyond the adiabatic approximation, which in our system is only reached for $\Omega_R/2\pi \sim 85\, E_R/h$.

Interestingly, the chiral BF theory formalism provides a very intuitive explanation of the experimentally observed asymmetric expansion. Upon release in the optical waveguide the atomic density decreases over time, modifying the chiral BF vector potential $A = -\lambda\rho$. This in turn results in a density-dependent electric field $E = -\partial_t A = \lambda\partial_t\rho$. As depicted in the lower panels of Fig. 7.13, in an inhomogeneous system the associated electric force is spatially dependent (black arrows) and distorts the atomic density distribution during the expansion, skewing it. Therefore, the asymmetric expansion dynamics observed in the experiment reveals the back-action of matter onto the gauge field and implies that A is a density-dependent vector potentials, which constitutes - apart from chiral solitons - the other characteristic of the chiral BF gauge theory.

7.4 Conclusion

In this chapter, we reported on the experimental realization of the encoded Hamiltonian of the 1D chiral BF theory and observed two of its predicted properties: chiral solitons and the distortion of the density profiles during expansion due to the BF electric force which can be extracted from the matter density using the local symmetry constraint of the theory.

This specific theory was never employed for simulation in an experiment before. However, the encoded Hamiltonian describes matter coupled to a vector potential, which depends linearly on density, and density-dependent vector potentials have been engineered previously with ultracold atoms[40–43] (see chapter 1). In contrast to previous experiments, we realized the full gauge theory including the crucial local symmetry constraint by enforcing the specific linear density dependence of the vector potential. To which extent the local symmetry constraint is enforced in our experiment, is shown e.g. in Fig. 7.6, where we validated the mapping to the

effective single-component Hamiltonian by calculating the expansion parameter or in Fig. 7.12 which compares the measured skewness of the density profiles with the prediction form the effective chiral BF theory. Another difference to previous experiments lies in the bulk system we employed for our measurements, whereas all other experiments to engineer density-dependent vector potentials were performed in a lattice system.

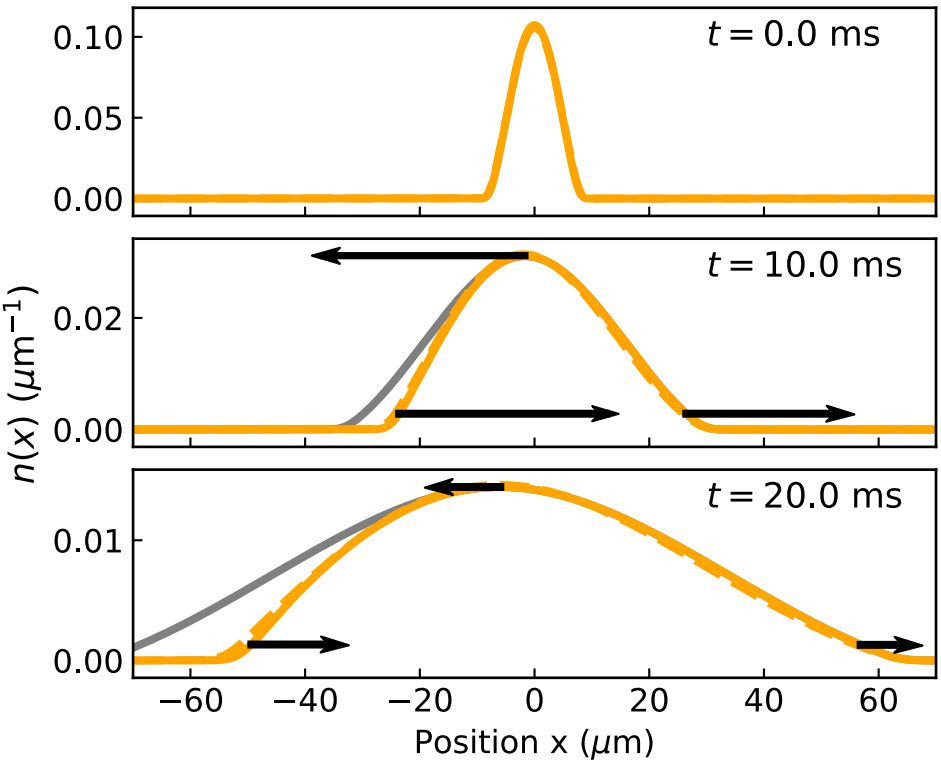

Figure 7.13: Density profiles for $\Omega_R/2\pi = 7\,E_R/h$ and $\delta_0 = 0$ from the effective chiral BF theory (solid orange line) and two-component simulations (dashed orange line). The agreement shows the validity of the chiral BF theory mapping in this regime. The decrease in density induces a density-dependent electric field $E = -\partial_t A = \lambda \partial_t \rho$ from the BF gauge potential A. The corresponding electric field varies along the density profile (black arrows), giving the cloud an asymmetric shape as observed in the experiment. The grey lines depict symmetric density profiles for comparison.

8 Conclusion and Outlook

In this thesis, we have investigated the simulation of a topological gauge theory in an analogue quantum simulator. More specifically, we have studied the realization of the chiral BF theory in a Bose-Einstein condensate of ^{39}K. The chiral BF theory constitutes a toy model for a topological gauge theory in 1D that results from the dimensional reduction of U(1) Abelian Chern-Simons theory from two to one dimension.

In chapters 1,2,3 and 5 of this thesis, we have studied on the theoretical level how to realize the chiral BF theory in a Bose-Einstein condensate.

- We started in chapter 1 by introducing the general idea of gauge theories and by summarizing the state of the art of simulating gauge theories with quantum systems in a quantum simulator approach. We identified the following goal for this thesis: the realization of a full topological gauge theory, i.e. where not only the matter field is coupled to a gauge field but in addition the gauge symmetry is enforced.

- We continued in chapter 2 with the comparison of the main properties of dynamical *versus* topological gauge theories by means of the prototypical examples of QED and Chern-Simons theory. We introduced the chiral BF gauge theory as one possible dimensional reduction of the Chern-Simons gauge theory and derived an encoded Hamiltonian in which the gauge field is eliminated using the local symmetry constraint. This results in a system with matter only degrees of freedom but subjected to unusual momentum-dependent interactions which are chiral.

- In chapter 3, we presented a realization of the encoded form of the chiral BF theory in a Bose-Einstein condensate. Building upon the seminal proposal of Edmonds et al. in Ref. [52], we have discussed a realistic experimental implementation in a BEC where two internal states with very unequal intrastate interactions are subjected to two-photon Raman transitions. Specifically, we have derived the effective low-energy description of the interaction Hamiltonian of the condensate from a microscopic point of view, instead of analyzing the system from the perspective of the density-dependent synthetic potential generated by the Raman coupling. This approach highlights the origin of the chiral interactions inherent to the encoding we have used, and also allows

us to relax the conditions required in the original proposal for the mapping to be valid: the need to fulfil both the adiabatic approximation for the Raman coupling, and the mean-field approximation for the BEC interactions. Indeed, we have shown that the equivalence to the chiral BF model remains valid for realistic experimental values of the Raman coupling strength, well beyond the adiabatic approximation.

In chapter 4 as well as in chapters 6,7 of this thesis, we turned to the experimental realization of the encoded chiral BF theory based on the combination of Raman coupling and unbalanced intrastate interactions in two internal states of a ^{39}K BEC. To this end, we started to study both key ingredients independently. On the one hand unequal intrastate interactions in a coherently coupled ^{39}BEC with radio-frequency in chapter 4. On the other hand the implementation of Raman coupling in chapter 5 and single particle effects in a ^{41}K BEC or ^{39}K BEC caused by the Raman coupling in chapter 6, respectively.

In more detail,

- In chapter 4 we showed that rf-coupling can be employed as interaction control tool as the effective interaction strength of the coupled states can be conveniently tuned by the coupling field parameters. We demonstrated a broad tunability and also applied the control in the attractive scattering length regime where we observed bright solitons and bright soliton trains formed out of the rf-dressed atoms, respectively.

- In chapter 5 we described and characterized the Raman coupling implemented in our experimental platform and in chapter 6, studied the single particle effects of Raman coupling by first directly measuring the modified dispersion relation of the lower dressed state with spin injection spectroscopy, second by measuring the static synthetic gauge potential from the momentum oscillation in the dipole trap and third by studying the changes in the free expansion dynamics by the momentum-dependent effective mass.

- Finally, we combined the Raman coupling and unbalanced intrastate interactions in chapter 7. With this system, we realised a ^{39}K Bose-Einstein condensate with effective chiral interactions and exploited them to engineer a one-dimensional topological gauge theory. Concretely, we have demonstrated the chiral interactions present in the condensate by studying its expansion dynamics for opposite momenta. Afterwards, we observed two of the main features of the encoded chiral BF theory: the formation of a chiral soliton and the observation of the effects of the chiral BF electric field. We investigated the chiral nature of the soliton by reversing its propagation direction during reflection on a barrier and observed immediate dissociation. We verified the validity of the encoded chiral BF Hamiltonian for our experimental

parameters and found that the observed chiral soliton is fairly well described by the chiral BF theory in its encoded form. In our final measurements, we studied the BF electric field, which we could infer from the expansion dynamics of the matter field as matter and chiral BF gauge field are related by the symmetry constraint of the theory. We showed that the electric force during the expansion modifies the symmetric shape of the condensate density. We also carefully distinguished it from single particle effects causing asymmetry by studying the electric force for different values of the two-photon detuning.

The realization of the encoded version of the chiral BF theory presented in this thesis opens the door to several further intriguing research directions. First of all, we could continue in the same line and further experimentally study the novel properties of our chiral system. For example, the chiral soliton solution predicted within the chiral BF theory also exists for BECs with repulsive interactions. In this case, dark instead of bright solitons should arise, which manifest themselves as density dips in the condensate (see chapter 2.4). Moreover, our system constitutes a well-suited playground to explore the effect the lack of Galilean invariance has on superfluidity. We expect the superfluid properties, which we could characterize by measuring the excitation spectrum, collective modes and critical velocity[187,188], to strongly depend on propagation direction[189].

Our reported experiments on realizing the encoded chiral BF theory also motivate the theoretical study of the physical relation between Chern-Simons and chiral BF theory. The dimensional reduction of the Chern-Simons theory is not unique, i.e. can be performed in different ways. Hence, one may wonder to which extent the chiral BF theory gives the proper effective description for edge states of fractional quantum Hall systems. This is a quite fundamental question that should be investigated from the theoretical perspective.

In this thesis we have focused on a linear geometry with open boundary conditions. An exciting prospect would be the experimental realization of the chiral BF theory with closed boundary conditions[52]. The new topology of the space would imply a different solution in which the magnetic degrees of freedom could not be completely eliminated. It could be achieved with a Bose-Einstein condensate trapped in an annular (ring-like) geometry[190–192] and subjected to an extended Raman coupling scheme which imparts angular momentum[193] instead of linear momentum as exploited in our present work. This would give rise to a chiral BF flux piercing the ring and would lead to a geometric phase for particles outside the flux area in full analogy to an Aharanov-Bohm phase.

As we have stressed the importance of the Chern-Simons theory for the understanding of fractional quantum Hall states, a natural further step would be an extension to the simulation of topological gauge theories in 2D and the direct modelling of

Chern-Simons theory. In Ref. [194] the group of Prof. Öhberg recently proposed a scheme for the generalization to 2D. It employs Raman-coupled BECs with unequal interactions in which the Raman beams impart angular momentum. In this way, interactions depend on the angular momentum and a magnetic field fulfilling the flux attachment condition of Chern-Simons theory is engineered. Hence, an experimental realization of the proposal would enable the investigation of true anyonic excitations, the flux attachment and topological order akin to the fractional quantum Hall effect.

Throughout this thesis, we have considered Raman-coupled BECs in the strong coupling limit, where the modified dispersion relation has a single minimum (see chapter 5) and the (interaction induced) Raman detuning leads to an effective (density dependent) vector potential. When we reduce the Raman coupling strength $\Omega_R/2\pi$ below 4 E_R/h, we enter the so-called spin-orbit coupling regime[102]. Here, the dispersion relation features two minima and the system exhibits two different phases. On the one hand, if the BEC components strongly repel each other, phase separation occurs and the system is in the plane wave phase. All atoms occupy a single minimum and have at $\delta_0 = 0$ either momentum $k_x = -k_R$ or $k_x = +k_R$. On the other hand, if the repulsive intrastate scattering lengths are sufficient large, the system is in the stripe phase, where it is miscible, i.e. the two minima are occupied simultaneously. In other words, the atoms are in a superposition of the two plane wave states with $= k \pm k_R$. In this stripe phase, two symmetries are broken simultaneously: the U(1) symmetry associated to the condensate's phase and the translational symmetry. This gives rise to supersolid properties, namely frictionless flows as in superfluids in combination with crystalline structure as in solids. A characteristic of this fascinating phase is the periodic modulation of the density profile of the condensate with a wavelength determined by the difference in momentum of the two occupied plane wave states. The stripe phase was recently observed in ultracold rubidium and sodium gases[159–161] and supersolidity was intensively investigated in dipolar quantum gases[195–197], where it stems from a very different mechanism. However, the experiments exploring the stripe phase suffered from a low fringe contrast and a narrow parameter regime in which the phase is stable. In contrast, employing a BEC of ^{39}K with the possibility to tune the interstate interactions allows the realization of a stripe phase where those are attractive. As my colleague Craig Chisholm recently calculated[172], this will enable high contrast fringes and a stability over a parameter range an order of magnitude greater/broader than previously realized. The group plans to use the enhanced stability to study for the first time e.g. the regime in the phase diagram where the plane wave, the single minimum and the stripe phase merge at a tricritical point[132]. Moreover, attractive interspin interactions within the spin-orbit coupling limit are an ideal setting to investigate the liquid phase stabilized by beyond mean field effects[86,121,198] and its combination with supersolid-like properties.

Publication list

Large parts of this thesis are based on the following publications:

Chapter 2, 3: C. S. Chisholm, A. Frölian, E. Neri, R. Ramos, L. Tarruell and A. Celi. Encoding a one-dimensional topological gauge theory in a Raman-coupled Bose-Einstein condensate. In preparation.

Chapter 4: J. Sanz, A. Frölian, C.S. Chisholm, C. R. Cabrera and L. Tarruell. Interaction control and bright solitons in coherently-coupled Bose-Einstein condensates. *Physical Review Letters* **128**, 013201 (2022).

Chapter 7: A. Frölian[†], C. S. Chisholm[†], R. Ramos, E. Neri, C. R. Cabrera, A. Celi and L. Tarruell. Realising a one-dimensional topological gauge theory in an optically dressed Bose-Einstein condensate. In preparation.

[†]These authors contributed equally.

Bibliography

[1] Steane, A. Quantum computing. *Reports Prog. Phys.* **61**, 117–173 (1998).

[2] Preskill, J. Quantum computing in the NISQ era and beyond. *Quantum* **2**, 79 (2018).

[3] Feynman, R. P. Simulating physics with computers. *Int. J. Theor. Phys.* **21**, 467–488 (1982).

[4] Blatt, R. & Roos, C. F. Quantum simulations with trapped ions. *Nat. Phys.* **8**, 277–284 (2012).

[5] Houck, A. A., Türeci, H. E. & Koch, J. On-chip quantum simulation with superconducting circuits. *Nat. Phys.* **8**, 292–299 (2012).

[6] Bloch, I., Dalibard, J. & Zwerger, W. Many-body physics with ultracold gases. *Rev. Mod. Phys.* **80**, 885–964 (2008).

[7] Bloch, I., Dalibard, J. & Nascimbène, S. Quantum simulations with ultracold quantum gases. *Nat. Phys.* **8**, 267–276 (2012).

[8] Bourdel, T. et al. Experimental study of the BEC-BCS crossover region in lithium 6. *Phys. Rev. Lett.* **93**, 050401 (2004).

[9] Greiner, M., Mandel, O., Esslinger, T., Hänsch, T. W. & Bloch, I. Quantum phase transition from a superfluid to a Mott insulator in a gas of ultracold atoms. *Nature* **415**, 39–44 (2002).

[10] Mazurenko, A. et al. A cold-atom Fermi-Hubbard antiferromagnet. *Nature* **545**, 462–466 (2017).

[11] Paredes, B. et al. Tonks-Girardeau gas of ultracold atoms in an optical lattice. *Nature* **429**, 277–281 (2004).

[12] Hadzibabic, Z., Krüger, P., Cheneau, M., Battelier, B. & Dalibard, J. Berezinskii-Kosterlitz-Thouless crossover in a trapped atomic gas. *Nature* **441**, 1118–1121 (2006).

[13] Eisert, J., Friesdorf, M. & Gogolin, C. Quantum many-body systems out of equilibrium. *Nat. Phys.* **11**, 124–130 (2015).

[14] Langen, T., Geiger, R. & Schmiedmayer, J. Ultracold atoms out of equilibrium. *Annu. Rev. Condens. Matter Phys.* **6**, 201–217 (2015).

[15] Wiese, U. J. Ultracold quantum gases and lattice systems: Quantum simulation of lattice gauge theories. *Ann. Phys.* **525**, 777–796 (2013).

[16] Zohar, E., Cirac, J. I. & Reznik, B. Quantum simulations of lattice gauge

theories using ultracold atoms in optical lattices. *Reports Prog. Phys.* **79**, 014401 (2015).

[17] Dalmonte, M. & Montangero, S. Lattice gauge theory simulations in the quantum information era. *Contemp. Phys.* **57**, 388–412 (2016).

[18] Bañuls, M. C. et al. Simulating lattice gauge theories within quantum technologies. *Eur. Phys. J. D* **74**, 165 (2020).

[19] Aidelsburger, M. et al. Cold atoms meet lattice gauge theory. *Philos. Trans. R. Soc. A* (2021).

[20] Mills, R. Gauge fields. *Cit. Am. J. Phys.* **57**, 493 (1989).

[21] Carmeli, M. *Classical fields: general relativity and gauge theory* (World Scientific Publishing Company, 2001).

[22] Kitaev, A. Anyons in an exactly solved model and beyond. *Ann. Phys. (N. Y).* **321**, 2–111 (2006).

[23] Lacroix, C., Mendels, P. & Mila, F. *Introduction to Frustrated Magnetism*, vol. 164 of *Springer Series in Solid-State Sciences* (Springer, 2011). 0306542.

[24] Sachdev, S. Emergent gauge fields and the high-temperature superconductors. *Philos. Trans. R. Soc. A Math. Phys. Eng. Sci.* **374** (2016).

[25] Martinez, E. A. et al. Real-time dynamics of lattice gauge theories with a few-qubit quantum computer. *Nature* **534**, 516–519 (2016).

[26] Kokail, C. et al. Self-verifying variational quantum simulation of lattice models. *Nature* **569**, 355–360 (2019).

[27] Muschik, C. et al. U(1) Wilson lattice gauge theories in digital quantum simulators. *New J. Phys.* **19**, 103020 (2017).

[28] Klco, N. et al. Quantum-classical computation of Schwinger model dynamics using quantum computers. *Phys. Rev. A* **98**, 032331 (2018).

[29] Yang, B. et al. Observation of gauge invariance in a 71-site Bose–Hubbard quantum simulator. *Nature* **587**, 392–396 (2020).

[30] Zhou, Z.-Y. et al. Thermalization dynamics of a gauge theory on a quantum simulator. *arXiv Prepr. 2107.13563* (2021).

[31] Bernien, H. et al. Probing many-body dynamics on a 51-atom quantum simulator. *Nature* **551**, 579–584 (2017).

[32] Surace, F. M. et al. Lattice Gauge Theories and String Dynamics in Rydberg Atom Quantum Simulators. *Phys. Rev. X* **10** (2020).

[33] Dai, H. N. et al. Four-body ring-exchange interactions and anyonic statistics within a minimal toric-code Hamiltonian. *Nat. Phys.* **13**, 1195–1200 (2017).

[34] Schweizer, C. et al. Floquet approach to Z2 lattice gauge theories with ultracold atoms in optical lattices. *Nat. Phys.* **15**, 1168–1173 (2019).

[35] Mil, A. et al. A scalable realization of local U(1) gauge invariance in cold atomic mixtures. *Science* **367**, 1128–1130 (2020).

[36] Fradkin, E. *Field theories of condensed matter physics* (Cambridge University Press, 2010), 2 edn.

[37] Wen, X. G. *Quantum Field Theory of Many-Body Systems: From the Origin of Sound to an Origin of Light and Electrons* (Oxford University Press, 2010).

[38] Altland, A. & Simons, B. *Condensed Matter Field Theory*. 5 (Cambridge University Press, 2006).

[39] Ezawa, Z. F. *Quantum Hall effects: Field theoretical approach and related topics* (World Scientific Publishing Co., 2008), 2 edn.

[40] Clark, L. W. et al. Observation of Density-Dependent Gauge Fields in a Bose-Einstein Condensate Based on Micromotion Control in a Shaken Two-Dimensional Lattice. *Phys. Rev. Lett.* **121**, 30402 (2018).

[41] Görg, F. et al. Realization of density-dependent Peierls phases to engineer quantized gauge fields coupled to ultracold matter. *Nat. Phys.* **15**, 1161–1167 (2019).

[42] Roushan, P. et al. Chiral ground-state currents of interacting photons in a synthetic magnetic field. *Nat. Phys.* **13**, 146–151 (2017).

[43] Lienhard, V. et al. Realization of a Density-Dependent Peierls Phase in a Synthetic, Spin-Orbit Coupled Rydberg System. *Phys. Rev. X* **10**, 21031 (2020).

[44] Rabello, S. J. A gauge theory of one-dimensional anyons. *Phys. Lett. B* **363**, 180–183 (1995).

[45] Benetton Rabello, S. J. 1D generalized statistics gas: A gauge theory approach. *Phys. Rev. Lett.* **76**, 4007–4009 (1996).

[46] Aglietti, U., Griguolo, L., Jackiw, R., Pi, S.-Y. & Seminara, D. Anyons and Chiral Solitons on a Line. *Phys. Rev. Lett.* **77**, 4406–4409 (1996).

[47] Jackiw, R. A Nonrelativistic Chiral Soliton in One Dimension. *J. Nonlinear Math. Phys.* **4**, 261–270 (1997).

[48] Griguolo, L. & Seminara, D. Chiral solitons from dimensional reduction of Chern-Simons gauged non-linear Schrödinger equation: classical and quantum aspects. *Nucl. Phys. B* **516**, 467–498 (1998).

[49] Fröhlich, J. & Marchetti, P. A. Quantum field theories of vortices and anyons. *Commun. Math. Phys.* **121**, 177–223 (1989).

[50] Kantor, R. & Susskind, L. A lattice model of fractional statistics. *Int. J. Mod. Phys. B* **05**, 2701–2733 (1991).

[51] Sun, K., Kumar, K. & Fradkin, E. Discretized Abelian Chern-Simons gauge theory on arbitrary graphs. *Phys. Rev. B - Condens. Matter Mater. Phys.* **92**, 115148 (2015).

[52] Edmonds, M. J., Valiente, M., Juzeliunas, G., Santos, L. & Öhberg, P. Simulating an interacting gauge theory with Ultracold Bose gases. *Phys. Rev. Lett.* **110**, 85301 (2013).

[53] Faddeev, L. & Jackiw, R. Hamiltonian reduction of unconstrained and constrained systems. *Phys. Rev. Lett.* **60**, 1692–1694 (1988).

[54] Jackiw, R. *(Constrained) quantization without tears* (1993).

[55] Jackson, J. D. *Classical Electrodynamics* (Wiley, 1998), 3 edn.

[56] Jackiw, R. & Pi, S. Y. Soliton solutions to the gauged nonlinear Schrödinger equation on the plane. *Phys. Rev. Lett.* **64**, 2969–2972 (1990).

[57] Jackiw, R. & Pi, S. Y. Classical and quantal nonrelativistic Chern-Simons theory. *Phys. Rev. D* **42**, 3500–3513 (1990).

[58] Wilczek, F. Quantum mechanics of fractional-spin particles. *Phys. Rev. Lett.* **49**, 957–959 (1982).

[59] Dirac, P. A. Generalized Hamiltonian dynamics. *Can. J. Math.* **70**, 129–148 (1950).

[60] Henneaux, M. & Teitelboim, C. *Quantization of Gauge Systems* (Princeton University Press, 2020).

[61] Kaplan, D. B. & Stryker, J. R. Gauss's law, duality, and the Hamiltonian formulation of U(1) lattice gauge theory. *Phys. Rev. D* **102**, 094515 (2020).

[62] Bender, J. & Zohar, E. Gauge redundancy-free formulation of compact QED with dynamical matter for quantum and classical computations. *Phys. Rev. D* **102**, 114517 (2020).

[63] Haase, J. F. et al. A resource efficient approach for quantum and classical simulations of gauge theories in particle physics. *Quantum* **5**, 1–20 (2021).

[64] Paulson, D. et al. Simulating 2D Effects in Lattice Gauge Theories on a Quantum Computer. *PRX Quantum* **2**, 030334 (2021).

[65] Celi, A. et al. Emerging Two-Dimensional Gauge Theories in Rydberg Configurable Arrays. *Phys. Rev. X* **10**, 021057 (2020).

[66] Banerjee, D., Caspar, S., Jiang, F. J., Peng, J. H. & Wiese, U. J. Nematic Confined Phases in the U(1) Quantum Link Model on a Triangular Lattice: An Opportunity for Near-Term Quantum Computations of String Dynamics on a Chip. *arXiv Prepr. 2107.01283* (2021).

[67] Kundu, A. Exact solution of double δ function Bose gas through an interacting anyon gas. *Phys. Rev. Lett.* **83**, 1275–1278 (1999).

[68] Dingwall, R. J., Edmonds, M. J., Helm, J. L., Malomed, B. A. & Öhberg, P. Non-integrable dynamics of matter-wave solitons in a density-dependent gauge theory. *New J. Phys.* **20**, 043004 (2018).

[69] Dingwall, R. J. & Öhberg, P. Stability of matter-wave solitons in a density-dependent gauge theory. *Phys. Rev. A* **99**, 023609 (2019).

[70] Bhat, I. A., Sivaprakasam, S. & Malomed, B. A. Modulational instability and soliton generation in chiral Bose-Einstein condensates with zero-energy nonlinearity. *Phys. Rev. E* **103**, 032206 (2021).

[71] Edmonds, M. J., Valiente, M. & Öhberg, P. Elementary excitations of chiral Bose-Einstein condensates. *EPL* **110**, 36004 (2015).

[72] Zheng, J. H., Xiong, B., Juzeliunas, G. & Wang, D. W. Topological condensate in an interaction-induced gauge potential. *Phys. Rev. A - At. Mol. Opt. Phys.* **92**, 013604 (2015).

[73] Chen, L. & Zhu, Q. *Chaotic dynamics of Bose-Einstein condensate in a density-dependent gauge field* (2021).

[74] Butera, S., Valiente, M. & Öhberg, P. Quantized vortices in interacting gauge theories. *J. Phys. B At. Mol. Opt. Phys.* **49**, 015304 (2015).

[75] Edmonds, M. & Nitta, M. Vortex patterns of atomic Bose-Einstein condensates in a density-dependent gauge potential. *Phys. Rev. A* **102**, 011303 (2020).

[76] Dauxois, T. and Peyrad, M. *Physics of solitons* (Cambridge University Press, 2006).

[77] Burger, S. et al. Dark solitons in Bose-Einstein condensates. *Phys. Rev. Lett.* **83**, 5198–5201 (1999).

[78] Denschlag, J. et al. Generating Solitons by Phase Engineering of a Bose-Einstein Condensate. *Science* **287**, 97–101 (2000).

[79] Khaykovich, L. et al. Formation of a matter-wave bright soliton. *Science* **296**, 1290–1293 (2002).

[80] Pethick, C.J., Smith, H. *Bose-Einstein condensation in dilute gases* (Cambridge University Press, 2008).

[81] Gerton, J. M., Strekalov, D., Prodan, I. & Hulet, R. G. Direct observation of growth and collapse of a Bose-Einstein condensate with attractive interactions. *Nature* **408**, 692–695 (2000).

[82] Donley, E. A. et al. Dynamics of collapsing and exploding Bose-Einstein condensates. *Nature* **412**, 295–299 (2001).

[83] Roberts, J. L. et al. Controlled collapse of a Bose-Einstein condensate. *Phys. Rev. Lett.* **86**, 4211–4214 (2001).

[84] Sackett, C. A., Stoof, H. T. & Hulet, R. G. Growth and collapse of a Bose-Einstein condensate with attractive interactions. *Phys. Rev. Lett.* **80**, 2031–2034 (1998).

[85] Carr, L. D. & Castin, Y. Dynamics of a matter-wave bright soliton in an expulsive potential. *Phys. Rev. A* **66**, 063602 (2002).

[86] Cheiney, P. et al. Bright Soliton to Quantum Droplet Transition in a Mixture of Bose-Einstein Condensates. *Phys. Rev. Lett.* **120**, 135301 (2018).

[87] Dalibard, J., Gerbier, F., Juzeliunas, G. & Öhberg, P. Colloquium: Artificial gauge potentials for neutral atoms. *Rev. Mod. Phys.* **83**, 1523–1543 (2011).

[88] Goldman, N., Juzeliunas, G., Öhberg, P. & Spielman, I. B. Light-induced gauge fields for ultracold atoms. *Reports Prog. Phys.* **77**, 126401 (2014).

[89] Dum, R. & Olshanii, M. Gauge structures in atom-laser interaction: Bloch oscillations in a dark lattice. *Phys. Rev. Lett.* **76**, 1788–1791 (1996).

[90] Visser, P. M. & Nienhuis, G. Geometric potentials for subrecoil dynamics. *Phys. Rev. A - At. Mol. Opt. Phys.* **57**, 4581–4591 (1998).

[91] Juzeliunas, G. & Öhberg, P. Slow light in degenerate fermi gases. *Phys. Rev. Lett.* **93** (2004).

[92] Juzeliunas, G., Ruseckas, J., Öhberg, P. & Fleischhauer, M. Light-induced effective magnetic fields for ultracold atoms in planar geometries. *Phys. Rev. A - At. Mol. Opt. Phys.* **73**, 025602 (2006).

[93] Zhu, S. L., Fu, H., Wu, C. J., Zhang, S. C. & Duan, L. M. Spin hall effects for cold atoms in a light-induced gauge potential. *Phys. Rev. Lett.* **97**, 240401 (2006).

[94] Spielman, I. B. Raman processes and effective gauge potentials. *Phys. Rev. A - At. Mol. Opt. Phys.* **79**, 063613 (2009).

[95] Günter, K. J., Cheneau, M., Yefsah, T., Rath, S. P. & Dalibard, J. Practical scheme for a light-induced gauge field in an atomic Bose gas. *Phys. Rev. A - At. Mol. Opt. Phys.* **79**, 011604 (2009).

[96] Dalibard, J. Introduction to the physics of artificial gauge fields. *Proc. Int. Sch. Phys. "Enrico Fermi"* **191**, 1–61 (2016).

[97] Berry, M. Quantal phase factors accompanying adiabatic changes. *Proc. R. Soc. London. A. Math. Phys. Sci.* **392**, 45–57 (1984).

[98] Khamehchi, M. A. et al. Negative-Mass Hydrodynamics in a Spin-Orbit-Coupled Bose-Einstein Condensate. *Phys. Rev. Lett.* **118**, 155301 (2017).

[99] Lin, Y. J. et al. Bose-Einstein condensate in a uniform light-induced vector potential. *Phys. Rev. Lett.* **102**, 130401 (2009).

[100] Lin, Y. J., Compton, R. L., Jiménez-García, K., Porto, J. V. & Spielman, I. B. Synthetic magnetic fields for ultracold neutral atoms. *Nature* **462**, 628–632 (2009).

[101] Lin, Y.-J. et al. A synthetic electric force acting on neutral atoms. *Nat. Phys. 2011 77* **7**, 531–534 (2011).

[102] Lin, Y. J., Jiménez-García, K. & Spielman, I. B. Spin-orbit-coupled Bose-Einstein condensates. *Nature* **471**, 83–86 (2011).

[103] Search, C. P. & Berman, P. R. Manipulating the speed of sound in a two-component Bose-Einstein condensate. *Phys. Rev. A* **63**, 43612 (2001).

[104] Nicklas, E. et al. Rabi flopping induces spatial demixing dynamics. *Phys. Rev. Lett.* **107**, 193001 (2011).

[105] Nicklas, E., Muessel, W., Strobel, H., Kevrekidis, P. G. & Oberthaler, M. K. Nonlinear dressed states at the miscibility-immiscibility threshold. *Phys. Rev. A - At. Mol. Opt. Phys.* **92**, 053614 (2015).

[106] Sanz, J., Frölian, A., Chisholm, C. S., Cabrera, C. R. & Tarruell, L. Interaction control and bright solitons in coherently-coupled Bose-Einstein condensates. *Phys. Rev. Lett.* **128**, 013201 (2022).

[107] Williams, R. A. et al. Synthetic Partial Waves in Ultracold Atomic Collisions. *Science* **335**, 314–317 (2012).

[108] Cabrera, C. R. *Quantum liquid droplets in a mixture of Bose-Einstein condensates*. PhD thesis, Institut de Ciències Fotóniques, Universitat Politècnica de Catalunya (2018).

[109] Sanz, J. *Two-component Bose-Einstein condensates with competing interactions*. PhD thesis, Institut de Ciències Fotóniques, Universitat Politècnica de Catalunya (2020).

[110] Modugno, G. et al. Bose-Einstein condensation of potassium atoms by sympathetic cooling. *Science* **294**, 1320–1322 (2001).

[111] Roati, G., Riboli, F., Modugno, G. & Inguscio, M. Fermi-Bose Quantum Degenerate 40K-87K Mixture with Attractive Interaction. *Phys. Rev. Lett.* **89**, 150403 (2002).

[112] Roati, G. et al. K39 Bose-Einstein condensate with tunable interactions. *Phys. Rev. Lett.* **99**, 010403 (2007).

[113] Tiecke, T. *Feshbach resonances in ultracold mixtures of the fermionic quantum gases 6Li and 40K*. PhD thesis, University of Amsterdam (2009).

[114] Sabulsky, D. O., Parker, C. V., Gemelke, N. D. & Chin, C. Efficient continuous-duty Bitter-type electromagnets for cold atom experiments. *Rev. Sci. Instrum.* **84**, 104706 (2013).

[115] Ramsey, N. F. A molecular beam resonance method with separated oscillating fields. *Phys. Rev.* **78**, 695–699 (1950).

[116] Chin, C., Grimm, R., Julienne, P. & Tiesinga, E. Feshbach resonances in ultracold gases. *Rev. Mod. Phys.* **82**, 1225–1286 (2010).

[117] Roy, S. et al. Test of the universality of the three-body Efimov parameter at narrow Feshbach resonances. *Phys. Rev. Lett.* **111**, 053202 (2013).

[118] Tiemann, E. et al. Beyond Born-Oppenheimer approximation in ultracold atomic collisions. *Phys. Rev. Res.* **2** (2020).

[119] Tanzi, L. et al. Feshbach resonances in potassium Bose-Bose mixtures. *Phys. Rev. A* **98**, 062712 (2018).

[120] Shibata, K. et al. Interaction modulation in a long-lived Bose-Einstein condensate by rf coupling. *Phys. Rev. A* **99**, 013622 (2019).

[121] Cabrera, C. R. et al. Quantum liquid droplets in a mixture of Bose-Einstein condensates. *Science* **359**, 301–304 (2018).

[122] Castin, Y. & Dum, R. Bose-Einstein Condensates in Time Dependent Traps. *Phys. Rev. Lett.* **77**, 5315 (1996).

[123] Strecker, K. E., Partridge, G. B., Truscott, A. G. & Hulet, R. G. Formation and propagation of matter-wave soliton trains. *Nat. 2002 4176885* **417**, 150–153 (2002).

[124] Pérez-García, V. M., Michinel, H. & Herrero, H. Bose-Einstein solitons in highly asymmetric traps. *Phys. Rev. A* **57**, 3837 (1998).

[125] Salasnich, L., Parola, A. & Reatto, L. Condensate bright solitons under transverse confinement. *Phys. Rev. A* **66**, 043603 (2002).

[126] Nguyen, J. H., Luo, D. & Hulet, R. G. Formation of matter-wave soliton trains by modulational instability. *Science* **356**, 422–426 (2017).

[127] Everitt, P. J. et al. Observation of a modulational instability in Bose-Einstein condensates. *Phys. Rev. A* **96**, 041601 (2017).

[128] Al Khawaja, U., Stoof, H. T., Hulet, R. G., Strecker, K. E. & Partridge, G. B. Bright Soliton Trains of Trapped Bose-Einstein Condensates. *Phys. Rev. Lett.* **89**, 200404 (2002).

[129] Salasnich, L., Parola, A. & Reatto, L. Modulational Instability and Complex Dynamics of Confined Matter-Wave Solitons. *Phys. Rev. Lett.* **91**, 080405 (2003).

[130] Carr, L. D. & Brand, J. Spontaneous Soliton Formation and Modulational Instability in Bose-Einstein Condensates. *Phys. Rev. Lett.* **92**, 4 (2004).

[131] Carr, L. D. & Brand, J. Pulsed atomic soliton laser. *Phys. Rev. A - At. Mol. Opt. Phys.* **70**, 033607 (2004).

[132] Li, Y., Pitaevskii, L. P. & Stringari, S. Quantum tricriticality and phase transitions in spin-orbit coupled Bose-Einstein condensates. *Phys. Rev. Lett.* **108**, 225301 (2012).

[133] D'Errico, C. et al. Feshbach resonances in ultracold 39K. *New J. Phys.* **9**, 223 (2007).

[134] Gong, J., Morales-Molina, L. & Hänggi, P. Many-Body Coherent Destruction of Tunneling. *Phys. Rev. Lett.* **103**, 133002 (2009).

[135] Greschner, S., Santos, L. & Poletti, D. Exploring unconventional Hubbard models with doubly modulated lattice gases. *Phys. Rev. Lett.* **113**, 183002 (2014).

[136] Greschner, S., Sun, G., Poletti, D. & Santos, L. Density-dependent synthetic gauge fields using periodically modulated interactions. *Phys. Rev. Lett.* **113**, 215303 (2014).

[137] Inouye, S. et al. Observation of Feshbach resonances in a Bose-Einstein condensate. *Nature* **392**, 151–154 (1998).

[138] Theis, M. et al. Tuning the scattering length with an optically induced Feshbach resonance. *Phys. Rev. Lett.* **93**, 123001 (2004).

[139] Enomoto, K., Kasa, K., Kitagawa, M. & Takahashi, Y. Optical Feshbach res-

onance using the intercombination transition. *Phys. Rev. Lett.* **101**, 203201 (2008).

[140] Bauer, D. M., Lettner, M., Vo, C., Rempe, G. & Dürr, S. Control of a magnetic Feshbach resonance with laser light. *Nat. Phys.* **5**, 339–342 (2009).

[141] Fu, Z. et al. Optical control of a magnetic Feshbach resonance in an ultracold Fermi gas. *Phys. Rev. A - At. Mol. Opt. Phys.* **88**, 041601 (2013).

[142] Clark, L. W., Ha, L. C., Xu, C. Y. & Chin, C. Quantum Dynamics with Spatiotemporal Control of Interactions in a Stable Bose-Einstein Condensate. *Phys. Rev. Lett.* **115**, 155301 (2015).

[143] Jagannathan, A., Arunkumar, N., Joseph, J. A. & Thomas, J. E. Optical Control of Magnetic Feshbach Resonances by Closed-Channel Electromagnetically Induced Transparency. *Phys. Rev. Lett.* **116**, 075301 (2016).

[144] Arunkumar, N., Jagannathan, A. & Thomas, J. E. Designer Spatial Control of Interactions in Ultracold Gases. *Phys. Rev. Lett.* **122**, 040405 (2019).

[145] Spielman, I. B. et al. Collisional deexcitation in a quasi-two-dimensional degenerate bosonic gas. *Phys. Rev. A - At. Mol. Opt. Phys.* **73**, 020702 (2006).

[146] Perrin, A. et al. Observation of atom pairs in spontaneous four-wave mixing of two colliding Bose-Einstein condensates. *Phys. Rev. Lett.* **99**, 150405 (2007).

[147] Bücker, R. et al. Twin-atom beams. *Nat. Phys.* **7**, 608–611 (2011).

[148] Lücke, B. et al. Twin matter waves for interferometry beyond the classical limit. *Science* **334**, 773–776 (2011).

[149] Cappellaro, A., Macrì, T., Bertacco, G. F. & Salasnich, L. Equation of state and self-bound droplet in Rabi-coupled Bose mixtures. *Sci. Rep.* **7**, 1–9 (2017).

[150] Lavoine, L., Hammond, A., Recati, A., Petrov, D. S. & Bourdel, T. Beyond-Mean-Field Effects in Rabi-Coupled Two-Component Bose-Einstein Condensate. *Phys. Rev. Lett.* **127**, 203402 (2021).

[151] Hammond, A., Lavoine, L. & Bourdel, T. Tunable three-body interactions in driven two-component Bose-Einstein condensates. *arXiv Prepr. 2112.01782* (2021).

[152] Zhang, J. Y. et al. Collective dipole oscillations of a spin-orbit coupled Bose-Einstein condensate. *Phys. Rev. Lett.* **109**, 115301 (2012).

[153] Qu, C., Hamner, C., Gong, M., Zhang, C. & Engels, P. Observation of Zitterbewegung in a spin-orbit-coupled Bose-Einstein condensate. *Phys. Rev. A - At. Mol. Opt. Phys.* **88**, 021604 (2013).

[154] Zhang, L. et al. Stability of excited dressed states with spin-orbit coupling. *Phys. Rev. A - At. Mol. Opt. Phys.* **87**, 011601 (2013).

[155] Leblanc, L. J. et al. Direct observation of Zitterbewegung in a Bose-Einstein condensate. *New J. Phys.* **15**, 073011 (2013).

[156] Ji, S. C. et al. Experimental determination of the finite-temperature phase diagram of a spin-orbit coupled Bose gas. *Nat. Phys.* **10**, 314–320 (2014).

[157] Ji, S. C. et al. Softening of roton and phonon modes in a Bose-Einstein condensate with spin-orbit coupling. *Phys. Rev. Lett.* **114**, 105301 (2015).

[158] Wu, Z. et al. Realization of two-dimensional spin-orbit coupling for Bose-Einstein condensates. *Science* **354**, 83–88 (2016).

[159] Bersano, T. M. et al. Experimental realization of a long-lived striped Bose-Einstein condensate induced by momentum-space hopping. *Phys. Rev. A* **99**, 051602 (2019).

[160] Putra, A., Salces-Cárcoba, F., Yue, Y., Sugawa, S. & Spielman, I. B. Spatial Coherence of Spin-Orbit-Coupled Bose Gases. *Phys. Rev. Lett.* **124**, 053605 (2020).

[161] Li, J. R. et al. A stripe phase with supersolid properties in spin-orbit-coupled Bose-Einstein condensates. *Nature* **543**, 91–94 (2017).

[162] Wang, P. et al. Spin-orbit coupled degenerate Fermi gases. *Phys. Rev. Lett.* **109**, 095301 (2012).

[163] Fu, Z. et al. Production of Feshbach molecules induced by spin-orbit coupling in Fermi gases. *Nat. Phys.* **10**, 110–115 (2014).

[164] Cheuk, L. W. et al. Spin-injection spectroscopy of a spin-orbit coupled Fermi gas. *Phys. Rev. Lett.* **109**, 095302 (2012).

[165] Burdick, N. Q., Tang, Y. & Lev, B. L. Long-lived spin-orbit-coupled degenerate dipolar Fermi gas. *Phys. Rev. X* **6** (2016).

[166] Song, B. et al. Spin-orbit-coupled two-electron Fermi gases of ytterbium atoms. *Phys. Rev. A* **94**, 061604 (2016).

[167] Mancini, M. et al. Observation of chiral edge states with neutral fermions in synthetic Hall ribbons. *Science* **349**, 1510–1513 (2015).

[168] Stuhl, B. K., Lu, H. I., Aycock, L. M., Genkina, D. & Spielman, I. B. Visualizing edge states with an atomic Bose gas in the quantum Hall regime. *Science* **349**, 1514–1518 (2015).

[169] Kang, J. H., Han, J. H. & Shin, Y. Realization of a Cross-Linked Chiral Ladder with Neutral Fermions in a 1D Optical Lattice by Orbital-Momentum Coupling. *Phys. Rev. Lett.* **121** (2018).

[170] Livi, L. F. et al. Synthetic Dimensions and Spin-Orbit Coupling with an Optical Clock Transition. *Phys. Rev. Lett.* **117** (2016).

[171] Wei, R. & Mueller, E. J. Magnetic-field dependence of Raman coupling in alkali-metal atoms. *Phys. Rev. A - At. Mol. Opt. Phys.* **87**, 042514 (2013).

[172] Chisholm, C. S. *Density-Dependent Gauge Fields in Potassium Bose-Einstein*

Condensates. PhD thesis proposal, Institut de Ciències Fotóniques, Universitat Politècnica de Catalunya (2020).

[173] Martone, G. I., Li, Y., Pitaevskii, L. P. & Stringari, S. Anisotropic dynamics of a spin-orbit-coupled Bose-Einstein condensate. *Phys. Rev. A - At. Mol. Opt. Phys.* **86** (2012).

[174] Vuletic, V., Kerman, A. J., Chin, C. & Chu, S. Observation of low-field Feshbach resonances in collisions of cesium atoms. *Phys. Rev. Lett.* **82**, 1406–1409 (1999).

[175] Chin, C., Vuletić, V., Kerman, A. J. & Chu, S. High resolution Feshbach spectroscopy of cesium. *Phys. Rev. Lett.* **85**, 2717–2720 (2000).

[176] Chin, C., Kerman, A. J., Vuletić, V. & Chu, S. Sensitive Detection of Cold Cesium Molecules Formed on Feshbach Resonances. *Phys. Rev. Lett.* **90**, 4 (2003).

[177] Chin, C. et al. Precision Feshbach spectroscopy of ultracold Cs2. *Phys. Rev. A - At. Mol. Opt. Phys.* **70**, 032701 (2004).

[178] Berninger, M. et al. Feshbach resonances, weakly bound molecular states, and coupled-channel potentials for cesium at high magnetic fields. *Phys. Rev. A - At. Mol. Opt. Phys.* **87**, 032517 (2013).

[179] Gould, P. L., Ruff, G. A. & Pritchard, D. E. Diffraction of atoms by light: The near-resonant Kapitza-Dirac effect. *Phys. Rev. Lett.* **56**, 827–830 (1986).

[180] Ovchinnikov, Y. B. et al. Diffraction of a released Bose-Einstein condensate by a pulsed standing light wave. *Phys. Rev. Lett.* **83**, 284–287 (1999).

[181] Gadway, B., Pertot, D., Reimann, R., Cohen, M. G. & Schneble, D. Analysis of Kapitza-Dirac diffraction patterns beyond the Raman-Nath regime. *Opt. Express* **17**, 19173 (2009).

[182] Thomas, P. *Optical dipole potentials for multi-component Bose-Einstein condensates*. Master thesis, Institut de Ciències Fotóniques, Universitat Politècnica de Catalunya (2017).

[183] Marchant, A. L. et al. Controlled formation and reflection of a bright solitary matter-wave. *Nat. Commun. 2013 41* **4**, 1–6 (2013).

[184] Zhao, X. et al. Macroscopic quantum tunneling escape of Bose-Einstein condensates. *Phys. Rev. A* **96**, 063601 (2017).

[185] Ramos, R., Spierings, D., Potnis, S. & Steinberg, A. M. Atom-optics knife edge: Measuring narrow momentum distributions. *Phys. Rev. A* **98**, 023611 (2018).

[186] Di Carli, A. et al. Collisionally Inhomogeneous Bose-Einstein Condensates with a Linear Interaction Gradient. *Phys. Rev. Lett.* **125** (2020).

[187] Jin, D. S., Ensher, J. R., Matthews, M. R., Wieman, C. E. & Cornell, E. A. Collective Excitations of a Bose-Einstein Condensate in a Dilute Gas. *Phys. Rev. Lett.* **77**, 420 (1996).

[188] Steinhauer, J., Ozeri, R., Katz, N. & Davidson, N. Excitation Spectrum of a Bose-Einstein Condensate. *Phys. Rev. Lett.* **88**, 120407 (2002).

[189] Zhai, H. Degenerate quantum gases with spin-orbit coupling: A review. *Reports Prog. Phys.* **78**, 026001 (2015).

[190] Ramanathan, A. et al. Superflow in a toroidal Bose-Einstein condensate: An atom circuit with a tunable weak link. *Phys. Rev. Lett.* **106**, 130401 (2011).

[191] Moulder, S., Beattie, S., Smith, R. P., Tammuz, N. & Hadzibabic, Z. Quantized supercurrent decay in an annular Bose-Einstein condensate. *Phys. Rev. A - At. Mol. Opt. Phys.* **86** (2012).

[192] Corman, L. et al. Quench-induced supercurrents in an annular Bose gas. *Phys. Rev. Lett.* **113** (2014).

[193] Chen, H. R. et al. Spin-Orbital-Angular-Momentum Coupled Bose-Einstein Condensates. *Phys. Rev. Lett.* **121** (2018).

[194] Valentí-Rojas, G., Westerberg, N. & Öhberg, P. Synthetic flux attachment. *Phys. Rev. Res.* **2**, 33453 (2020).

[195] Böttcher, F. et al. Transient Supersolid Properties in an Array of Dipolar Quantum Droplets. *Phys. Rev. X* **9**, 011051 (2019).

[196] Tanzi, L. et al. Observation of a Dipolar Quantum Gas with Metastable Supersolid Properties. *Phys. Rev. Lett.* **122**, 130405 (2019).

[197] Chomaz, L. et al. Long-Lived and Transient Supersolid Behaviors in Dipolar Quantum Gases. *Phys. Rev. X* **9**, 021012 (2019).

[198] Petrov, D. S. Quantum Mechanical Stabilization of a Collapsing Bose-Bose Mixture. *Phys. Rev. Lett.* **115**, 155302 (2015).